THE UNIVERSITY OF QUEENSLAND

AUSTRALIA

All-optical ^{87}Rb Bose-Einstein condensate apparatus: Construction and operation

Dipl. phys. I. L. H. Humbert

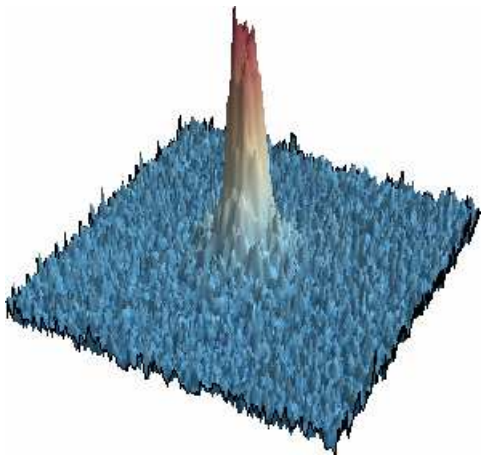

A thesis submitted for the degree of Doctor of Philosophy at

The University of Queensland in 2012

School of Mathematics and Physics

Abstract

Research on degenerate quantum gases of dilute atomic gases has become a well established field in modern physics and revealed many astonishing phenomena. The first experiments on Bose and Fermi gases at low temperatures aimed to prove the predictions of quantum mechanics on a macroscopic scale. Since then we make use of Bose and Fermi gases and mixtures of any combination to model other many body systems. A property of Bose Einstein condensates is superfluidity which we want to investigate further in toroidal potentials with a new apparatus which can produce an all-optical BEC. This means trapping thermal atoms in an optical dipole trap and cooling the sample by evaporation into the quantum degenerate regime. This new technique was first successfully demonstrated by M.D. Barrett et al. in 2001 and promises to be faster and simpler than the well established and common way of evaporation in magnetic traps.

A new apparatus was built by the author and we report on the experimental details of the trapping of ^{87}Rb atoms from a hot vapour and cooling them in a magneto-optical trap, and further evaporation to quantum degeneracy in a crossed optical dipole trap operating at a wavelength of $\lambda = 1064$nm, with accurate control of the power in both beams via a feedback loop. The evaporation of neutral atoms of ^{87}Rb in far red detuned optical dipole traps using linearly polarised laser light is spin independent, and mixed spinor condensates of the F=1 manifold can be formed. As an empirical technique we found by applying a magnetic gradient field during the final evaporation that we can selectively populate m_F spin states or prepare mixtures. This intriguing mechanism was found earlier as well by M. S. Chang, but is yet not fully understood and subject of our future research. We can now routinely prepare an almost pure condensate containing up to 7000 atoms in the condensed phase purely in the $m_F = 0$ spin state.

This thesis contains the theoretical framework of Bose-Einstein condensation with in mean-field theory, the concepts of cooling of atoms in magneto-optical traps, the

trapping and evaporation in optical dipole traps and the experimental realisation. In the future this experiment will be extended by a fast scanning dipole trap to apply arbitrary time averaged potentials of more complex geometries, such as toroidal traps to study the effects of superfluidity in a periodic potential. The production of toroidal traps and cold atoms in such a trap are outlined in this thesis.

Declaration by author

This thesis is composed of my original work, and contains no material previously published or written by another person except where due reference has been made in the text. I have clearly stated the contribution by others to jointly-authored works that I have included in my thesis.

I have clearly stated the contribution of others to my thesis as a whole, including statistical assistance, survey design, data analysis, significant technical procedures, professional editorial advice, and any other original research work used or reported in my thesis. The content of my thesis is the result of work I have carried out since the commencement of my research higher degree candidature and does not include a substantial part of work that has been submitted to qualify for the award of any other degree or diploma in any university or other tertiary institution. I have clearly stated which parts of my thesis, if any, have been submitted to qualify for another award.

I acknowledge that an electronic copy of my thesis must be lodged with the University Library and, subject to the General Award Rules of The University of Queensland, immediately made available for research and study in accordance with the Copyright Act 1968.

I acknowledge that copyright of all material contained in my thesis resides with the

Published Works by the Author Incorporated into the Thesis

No publications

Publications included in this thesis

No publications included

Contributions by others to the thesis

Ion Struesco, Fabien Casenave, Nicolas Manquest, Marco Perron, Daniel Sigle, Jessica Butcher and Kate Whittaker contributed in their time as PhD students, diploma students, research visitors or during their intern ship to the experimental setup and the collection of data.

Statement of parts of the thesis submitted to qualify for the award of anotherdegree

None.

Acknowledgements

Many people helped me on my way to finish this thesis and I would like to express my thanks to them

For advice and guidance during my time at UQ I would like to thank my advisory team Halina Rubinsztein-Dunlop, Norman Heckenberg, E.D. van Ooijen and Mark Baker.

I would like to thank also like to thank all other students who were involved on the project and I particularly like to thank Kate Whitettaker for some entertaining games of "BEC-roulette".

On theory side of the project I was supported by Matthew Davis and Simon Haine, who helped out with concepts and Gendankenexperiments.

I would like to thank the former and current staff of SMP Jo Hughes, Jenny Robinson, Julie Thai, Jackie Woods and Joan Ryan for helping out on organising bookings, fixing time sheets, tracing parcels and providing an invaluable administrative support.

The team from the workshop Alan Reid, Dave, Griffo and Evan for screws cutting bits and pieces, drilling wholes for me mostly on a Friday afternoon when they were about to leave.

Andrew White for interesting and entertaining conversations about physics and beyond.

Matthew Broome and Michael Garrett for many unforgettable mornings in the surf.

All my friends in the northern and southern hemisphere.

And finally I like to thank my parents Heiko and Ines who have supported me throughout my time in Brisbane over such a long distance. I have time now. I call you back later.

Keywords

Bose-Einstein condendsation, optical trapping,

Australian and New Zealand Standard Research Classifications (ANZSRC)

ANZSRC code: 020601, Degenerate Quantum Gases and Atom Optics

Fields of Research (FOR) Classification

FoR code: 0206, Quantum Physics

Contents

List of Figures

List of Tables

List of abbrevations

AOM ..... Acousto optical modulator

BEC ..... Bose-Einstein condensate

MOT ..... Magneto optical trap

ODT ..... Optical dipole trap

f ..... frequency

Γ_{sc} ..... scattering rate

λ ..... wavelength

ω ..... angular frequency

f ..... frequency

P ..... power

U_0 ..... trap depth

w_0 ..... waist

z_R ..... Rayleigh length

1 Introduction

1.1 Overview

Today 16 years after the first observation of Bose-Einstein condensates (BEC) in dilute atomic vapours [1, 2], the community of physicists working all over the world theoretically and experimentally on this intriguing phenomenon is still growing. The basic theory of BECs and the concepts of forming a BEC are well established [1, 2, 3, 4, 5]. Its prediction for an ideal gas was made in 1924/25 by A. Einstein based on ideas of S.Bose [6, 7]. What makes BEC interesting is that the ground state is macroscopically occupied and the condensed particles form a "giant" matter wave. Using the so called mean-field theory one can express the condensate wave function as $\Phi(\mathbf{r}, t) = \phi(\mathbf{r})\mathbf{exp}(-i\mu t/\hbar)$, where μ denotes the chemical potential and ϕ is normalised to the total number of particles. This wave function is a solution of the Gross-Pitaevski equation (GPE), a "nonlinear Schrödinger equation". The non linearity comes from the mean-field term that is proportional to the density $n(\mathbf{r}) = \phi^2(\mathbf{r})$.
Most confining traps for real gases are well approximated by harmonic potentials. With the trapping frequency ω_{ho} we find the characteristic length scale $a_{\mathrm{ho}} = \sqrt{\hbar/m\omega_{\mathrm{ho}}}$ of the order of a few microns. This is small in our daily life, but gigantic for quantum mechanical systems. The verification of the wave character of BEC was therefore an important experiment [8]. Moreover a BEC is a super fluid, which means it flows without friction, as observed first in liquid helium [9]. An impressive demonstration was given by Reppy [10], who investigated currents of liquid helium in toroidal vessels and did not observe any decay of the current over a period of 12 hours. It was London

[11], who discovered the link between the superfluidity of helium and Bose-Einstein condensation, which is the macroscopic occupation of a ground state in both systems. Helium is a strongly interacting system and therefore a theory of superfluid helium is hard to derive. BECs in dilute atomic gases are perfect systems for the theoretical model of Bogoliubov [12]. This model describes a weakly interacting Bose gas through its density and a small s-wave scattering length a_S. Improvements in experimental techniques, refining the theory of superfluidity in BECs and quantitative agreement led to a better understanding. In a couple of crucial experiments the superfluid properties of BECs like critical velocity, vortices and vortex lattices were demonstrated in [13, 14, 15, 16, 17, 18, 19]. However, there are still many questions to be answered.

1.2 Motivation for an all optical BEC and for toroidal traps

In this project the aim is to produce an all optical BEC and to construct smooth toroidal traps for neutral atoms in order to study superfluidity.
Toroidal traps represent an ideal system for quantitative studies of the emergence of superfluidity. These toroidal traps have to be smooth and small enough in order to enable studies of multiply connected BECs in a quantitative way. Many techniques have already been developed to achieve these aims. Experimental techniques such as polarisation gradient cooling, velocity selective coherent population trapping, Raman cooling and evaporative cooling in optical dipole force traps, were developed to reach the BEC phase transition. M.D. Barrett et al. [20] were the first to demonstrate the formation of a BEC in an optical dipole force trap. The advantages of this method are the much faster formation of a BEC than in a magnetic trap and spin independence. The faster evaporation relaxes considerably the requirement for long trap lifetimes; or in case of long trap life times it gives more time for experiments. Magnetic traps confine only one or two spin projections and therefore spinor condensates [21] are

formed with this technique. An early idea, even before the first BEC, of axially symmetric traps can be found in [22]. The proposal was to use toroidal traps as storage rings for cold atoms. The proposals for toroidal traps with axial symmetry for confining BECs range from magnetic traps [23, 24, 25], RF-dressed magnetic traps [26] to the use of spatial light modulators [27]. In order to study multiply connected BECs these traps have to be on the order of a few μm in diameter to be able to test which theoretical predictions like excitations, solitons or spinors to name some [28, 29, 30, 31]. These small trap geometries are realisable with far off resonant dipole traps of overlapped red and blue detuned laser beams [32]. Also Laguerre-Gaussian are proposed to be used to from such ring traps [33]. The first evidence of persistent currents of a superfluid Bose gas was demonstrated by K. Helmerson [34] in the group of W.D. Phillips where the toroidal trap was made of a magnetic potential overlapped with a blue detuned optical dipole trap at the center of symmetry. Another method for a ring shaped trap is proposed by S. Schnelle et al. [35] which suggests a fast scanning beam trap with a 2D-AOM.

1.3 Thesis outline

The authors work to build an experiment to create an all optical BEC is presented in the following chapters:

Chapter 2: Theoretical background on Bose-Einstein condensation

In the second chapter we will discuss the fundamental concept of Bose-Einstein condensation in a harmonic trap. By evaluating the statistics of a trapped bosonic gas we can derive an expression for the critical temperature T_c where Bose Einstein condensation occurs. Solving the "nonlinear Schrödinger equation" using a mean field approach allows us to find an expression for the density profile of a Bose-Einstein condensate in the Thomas-Fermi limit.

Chapter 3: Interaction of light with matter

We will focus on the interaction of light with matter in the third chapter and discuss the concepts of trapping and cooling neutral atoms in a near resonant and far detuned laser field. The former is based on a momentum transfer by the absorption of a photon by an atom whereas the latter is based on a decrease of the ground state energy and therefore creating an attractive potential if the laser field is red detuned.

Chapter 4: Experimental set up

Experimental details such as the design of the experiment including the vacuum system, the laser system for the MOT, the control of the power of the dipole traps and the imaging are described in detail in chapter 4.

Chapter 5: MOT

In chapter 5 we present the operation of the magneto optical trap in the current experiment. The first MOT was built with free space propagating beams and was replaced later with fibre coupled beams which was a major improvement of the experiment leading to better stability and reproducibility.

Chapter 6: Optical dipole traps

Chapter 6 will first focus on the general concept and ideas of the evaporation of neutral atoms in an optical dipole trap. After the description of the properties of our traps two schemes for the evaporation are presented and discussed. An all optical Bose-Einstein condensate was successful and was identified as a spinor condensate of the $F = 1$ manifold. A technique to prepare a particular m_F state is described as well.

Chapter 7: Towards a scanning dipole trap

A brief overview for a proposal of building a scanning beam trap is given in chapter 7. We also briefly discuss the physics of a bosonic gas at low temperatures in different regimes of interactions in a toroidal trap.

Chapter 8: Conclusions and outlook

A discussion of the achievements during the author's work and an outlook is given in the last chapter.

2 Theoretical background on Bose-Einstein condensation

2.1 Bose-Einstein condensation

In this chapter we discuss theoretical concepts behind the physics of Bose-Einstein condensation. First let us discuss the statistical physics of an ideal bosonic gas developed by Bose in 1924 [6] and supported by A. Einstein [7]. We derive an expression to calculate a critical temperature where Bose-Einstein condensation occurs and an expression for the number of particles in a Bose-Einstein condensate. The ground state is occupied macroscopically and we have to solve a Hamiltonian for N interacting particles. Numerical simulations for a number less than 10^4 can be calculated but for larger numbers these calculations become impractical if not impossible. However, a mean-field approximation provides an approach to calculate the ground state of a system and as well its thermodynamics. In the following sections we discuss the statistical and quantum mechanical properties of a BEC, following the theoretical description of F. Dalfovo et al [36] and [37].

2.1.1 Statistical considerations

For simplicity let us consider a harmonic potential, which approximates well confining potentials for atoms in real experiments, and let us draw some important conclusions from this model system. For a harmonic potential in three dimensions where the

energy U of a particle with mass m is given by

$$U(\vec{r}) = \frac{m}{2}(\omega_x^2 x^2 + \omega_y^2 y^2 + \omega_z^2 z^2) \tag{2.1}$$

with trapping frequencies ω_i, the energy eigenstates of a single particle are well known and given by

$$\epsilon_{n_x n_y n_z} = \left(n_x + \frac{1}{2}\right)\hbar\omega_x + \left(n_y + \frac{1}{2}\right)\hbar\omega_y + \left(n_z + \frac{1}{2}\right)\hbar\omega_z \tag{2.2}$$

where $\vec{n} = \{n_x, n_y, n_z\}$ are non-negative integers and $\hbar$ is Plancks constant divided by 2π. The number of particles of a bosonic ideal gas in an energy state E_i at any temperature T is given by the distribution

$$N_i(E_i) = \frac{1}{\exp\left(\frac{E_i - \mu}{k_B T} - 1\right)} \tag{2.3}$$

which is known as the Bose-Einstein distribution, where μ denotes the chemical potential, k_B the Boltzmann constant and T the temperature. The total number of particles and the total energy of the system are conserved and we write them as

$$N = \sum_i N(E_i) \tag{2.4}$$

$$E = \sum_i E_i N(E_i). \tag{2.5}$$

For convenience we separate from the total number of particles the lowest eigenstate ϵ_{000} of the sum in equation (2.4) and with N_0 we denote the number of particles in the ground state of the system. Thus we rewrite equation (2.4)

$$N = N_0 + N_{th} = N_0 + \lim_{\mu \to 0} \sum_{\vec{n} \neq 0} \frac{1}{\exp(\frac{E_i - \mu}{k_B T} - 1)} \tag{2.6}$$

where N_{th} are particles in excited states. It is difficult to evaluate the infinite sum but for $N \to \infty$ we can replace the sum by an integral,

$$N - N_0 = \int_0^\infty \frac{dn_x dn_y dn_z}{\exp[\beta\hbar(\omega_x n_x + \omega_y n_y + \omega_z n_z)] - 1} \tag{2.7}$$

This semiclassical approximation is accurate for large numbers of particles and excitation energies larger than the level spacing $k_B\mathrm{T} >> \hbar\omega$. With changing the variables in (2.7) to $\beta\hbar\omega_i n_i = \tilde{n_i}$ we can evaluate exactly the integral and find

$$N - N_0 = \zeta(3)\left(\frac{k_B T}{\hbar\overline{\omega}}\right)^3, \tag{2.8}$$

where ζ denotes the Riemann zeta function and $\overline{\omega}$ the geometrical frequency $\overline{\omega} = (\omega_x\omega_y\omega_z)^{1/3}$. The transition temperature occurs where $N_0 \to 0$ and we find for the critical temperature

$$k_\mathrm{B} T_c^0 = \hbar\overline{\omega}\left(\frac{N}{\zeta(3)}\right)^{\frac{1}{3}}. \tag{2.9}$$

This critical temperature is well defined in the thermodynamic limit letting $N \to \infty$ and $\hbar\overline{\omega} \to 0$ while keeping the product $N\overline{\omega}^3$ constant and within this limit we find for the fraction of the particles in the ground state for $T < T_c$

$$\frac{N_0}{N} = 1 - \zeta(3)\left(\frac{k_B}{\hbar\overline{\omega}}\right)^3 \frac{T^3}{N} = 1 - \frac{T^3}{T_c^3} \tag{2.10}$$

as depicted in figure 2.1 and verified in some experiments [38, 39]. From equation (2.10) we see that even below the critical temperature T_c, where Bose-Einstein condensation occurs, only a fraction of the particles condense into the ground state. We find the same result, if we calculate the density of thermal particles using the semiclassical approximation, where we integrate in the thermodynamical limit over momentum space $n_T(\mathbf{r}) = \int d\mathbf{p}(2\pi\hbar)^{-3}[\exp(\beta\epsilon(\mathbf{p},\mathbf{r})) - 1]^{-1}$, with the semiclassical energy in phase space $\epsilon(\mathbf{p},\mathbf{r}) = p^2/2m + V_{ext}$ and find for the density in phase space

$$n_T(\mathbf{r})\lambda_{dB}^3 = PSD \tag{2.11}$$

with the thermal wavelength $\lambda_{dB} = \sqrt{2\pi\hbar^2/mk_\mathrm{B}T}$. Bose Einstein condensation occurs at $T = T_c$ and the phase space density becomes $PSD \sim 2.6$. Therefore we see from equation (2.11) that Bose Einstein condensation occurs at high densities and low temperatures. The phase space diagram in figure 2.2 shows the density of particles versus the thermal wavelength (temperature) for ^{87}Rb. The dashed lines correspond

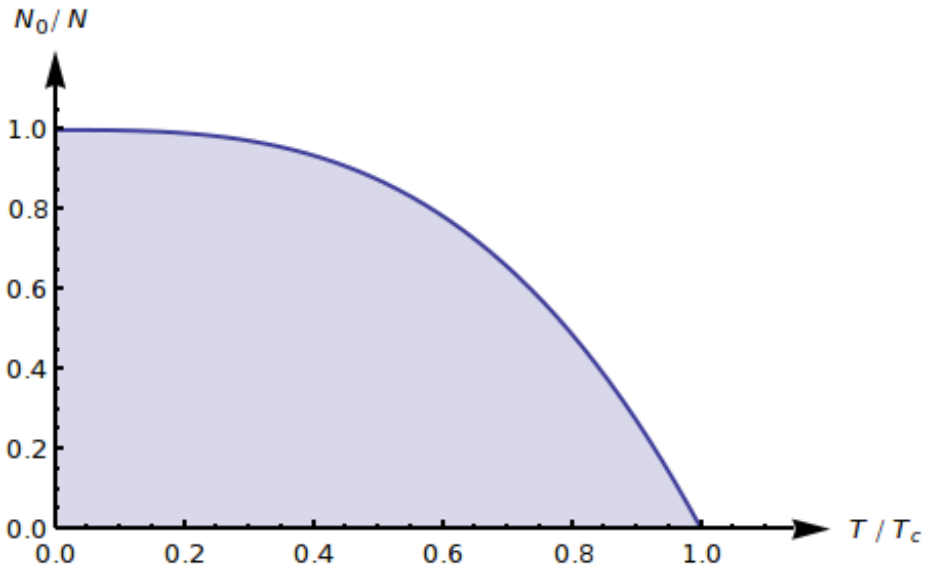

Figure 2.1: The relative number of condensed particles as a function of the temperature calculated from equation 2.10. It can clearly be seen that that condensation only begins at $T = T_c$. For $T = 0.37T_c$ the fraction of condensed particles is $N_0/N = 0.95$.

to a constant phase space density. At room temperature the phase space density is on the order of 10^{-18} and the cooling in a magneto-optical trap lowers the temperature by five orders of magnitude. Also a higher density of the atoms being trapped in a magneto optical trap means a higher phase-space density on the order of $10^{-7} - 10^{-6}$. Further cooling by evaporation raises the density of the atomic sample and lowers the temperature rasising the phase space density above the critical density of 2.6 where Bose-Einstein condensation occurs. Neutral atoms can be trapped in magnetic traps or optical dipole traps. The reader is referred to chapter 6 for a more detailed discussion of the differences of the two trapping techniques and a closer description of experimental techniques of our experiment.

The description of the noninteracting harmonic-oscillator as discussed above is only a guide and for a more comprehensive description one needs to take two other effects into account: the finite size of the system, and interactions among the constituents of the gas [37]. With these considerations in mind, in the next section we

derive a method to calculate the density of the gas in the ground state.

2.1.2 Quantum mechanical considerations

A Bose-Einstein condensate is a many-body system which can be very successfully described in a mean field approach. We briefly discuss this approach in this section following closely the more detailed description in [37]. We consider an interacting bosonic gas of N particles in an external potential V_{ext}. The Hamiltonian of this system is given by

$$\hat{H} = \int d\mathbf{r}\ \hat{\Psi}^\dagger(\mathbf{r}) \left[-\frac{\hbar^2}{2m}\nabla^2 + V_{\text{ext}}(\mathbf{r}) \right] \hat{\Psi}(\mathbf{r}) + \frac{1}{2} \int d\mathbf{r}\ d\mathbf{r}'\ \hat{\Psi}^\dagger(\mathbf{r}) \hat{\Psi}^\dagger(\mathbf{r}') V(\mathbf{r}-\mathbf{r}') \hat{\Psi}(\mathbf{r}') \hat{\Psi}(\mathbf{r}) \tag{2.12}$$

where $\hat{\Psi}(\mathbf{r})$ and $\hat{\Psi}^\dagger(\mathbf{r})$ are the bosonic creation and annihilation field operators, and $V(\mathbf{r}-\mathbf{r}')$ is the interaction potential of two bodies. Bogoliubov formulated an approximation based on the idea of separation of the condensate fraction of the field operator which can be written as $\hat{\Psi}(\mathbf{r}) = \sum_\alpha \Psi_\alpha(\mathbf{r})\ a_\alpha$ with single particle wave functions $\Psi_\alpha(\mathbf{r})$ and bosonic creation and annihilation operators $a_\alpha^\dagger$ and a_α. In order to describe the general case of a non-uniform gas and time-dependent configuration we write for the field operator

$$\hat{\Psi}(\mathbf{r},t) = \Phi(\mathbf{r},t) + \hat{\Psi}'(\mathbf{r},t) \tag{2.13}$$

in the Heisenberg representation. The complex function $\Phi(\mathbf{r},t)$ is defined as the expectation value of the field operator $\Phi(\mathbf{r},t) = \left\langle \hat{\Psi}(\mathbf{r},t) \right\rangle$, and fixes the density of the condensate through its modulus $n_0 = \left| \hat{\Phi}(\mathbf{r},t) \right|^2$. Therefore the function $\Phi(\mathbf{r},t)$ can be called the "wave function of the condensate" although it is a classical field having the meaning of an order parameter. We insert the field operator into equation 2.12 and treat the operator $\hat{\Psi}'$ as a small perturbation and neglect it. Thus using the Heisenberg equation the many-body Hamiltonian becomes

$$i\hbar \frac{\delta}{\delta t} \hat{\Psi}(\mathbf{r},t) = \left[\hat{\Psi}, \hat{H} \right] = \left[-\frac{\hbar^2 \nabla^2}{2m} + V_{\text{ext}}(\mathbf{r}) + \int d\mathbf{r}' \hat{\Psi}^\dagger(\mathbf{r}',t) V(\mathbf{r}'-\mathbf{r}) \hat{\Psi}(\mathbf{r}',t) \right] \hat{\Psi}(\mathbf{r},t) \tag{2.14}$$

We replace $V(\mathbf{r}' - \mathbf{r})$, the atom-atom interaction term with the two body potential $V(\mathbf{r}' - \mathbf{r}) = g\delta(\mathbf{r}' - \mathbf{r})$ which is characterised by the coupling parameter g and is related to the s-wave scattering length a by

$$g = \frac{4\pi\hbar^2 a}{m} \tag{2.15}$$

and finally arrive at the Gross-Pitaevskii equation (GPE)

$$i\hbar\frac{\partial}{\partial t}\Phi(\mathbf{r},t) = \left(-\frac{\hbar^2\nabla^2}{2m} + V_{\text{ext}}(\mathbf{r},t) + g\left|\Phi(\mathbf{r},t)\right|^2\right)\Phi(\mathbf{r},t). \tag{2.16}$$

The three terms on the right hand side of this equation are the kinetic energy, the potential energy and the interaction energy. Of particular interest is the ratio of the interaction energy and the kinetic energy. Typical densities of dilute gases are on the order of 10^{13} to 10^{15}cm^{-3} and we call a system dilute if $\overline{n}\left|a\right|^3 \ll 1$, where $\overline{n}$ is the average density of the system. The kinetic energy is on the order of $N\hbar\omega$ e.g. $E_{\text{kin}} \propto N/a_{\text{ho}}^{-2}$, whereas the energy of the interaction is of the order of $gN\overline{n}$ e.g $E_{\text{int}} \propto N^2\left|a\right|/a_{\text{ho}}^3$. So we find for the ratio of the two energies

$$\frac{E_{\text{int}}}{E_{\text{kin}}} \propto \frac{N\left|a\right|}{a_{\text{ho}}}. \tag{2.17}$$

Changing the sign and amplitude of the coupling parameter g can significantly change the density of the cloud. For positive values of g the coupling is repulsive and for negative values it is attractive. This has of course a significant effect on the dynamics and thermodynamics as well. The condensate wave function of the ground state is of the form $\Phi(\mathbf{r},t) = \phi(\mathbf{r})\exp(-i\mu t/\hbar)$, with the chemical potential μ and a real function ϕ normalised to the total number of condensed bosons $N_0 = N = \int d\mathbf{r}\phi^2$. Therefore the GPE 2.16 becomes

$$\left(-\frac{\hbar^2\nabla^2}{2m} + V_{\text{ext}}(\mathbf{r}) + g\phi^2(\mathbf{r})\right)\phi(\mathbf{r}) = \mu\phi(\mathbf{r}). \tag{2.18}$$

For $g \neq 0$ one has to solve the GP equation 2.18 numerically to find the density. For no inter-particle interactions, e.g. $g = 0$, the GP equation 2.18 turns into $-\hbar^2/(2m\nabla^2) + V_{\text{ext}}$ of similar form of the time independent Schrödinger equation for a single particle

but not to be mistaken with the SE. Solutions of the SE are quantum states of the (N body) system, whereas solutions of the GPE are classical fields which belong to degenerated states of the N body system. In a harmonic potential 2.1 the solution is a Gaussian function normalised to the numberof particles

$$\phi(\mathbf{r}) = \sqrt{N}\ \phi_0(\mathbf{r}) = \sqrt{N}\ \frac{m\overline{\omega}}{\pi\hbar}\ \exp\left[-\frac{m}{2\hbar}\sum\omega_i r_i^2\right]. \tag{2.19}$$

Another approximation, the so called Thomas-Fermi limit, is given in the case of repulsive interactions $g > 0$ and for $Na/a_{\mathrm{ho}} \gg 1$. In this particular case we can neglect the term of the kinetic energy

$$\left(V_{\mathrm{ext}}(\mathbf{r}) + g\phi^2(\mathbf{r})\right)\phi(\mathbf{r}) = \mu\phi(\mathbf{r}) \tag{2.20}$$

and we find for the density profile

$$n(\mathbf{r}) = \phi^2(\mathbf{r}) = \frac{\mu - V_{\mathrm{ext}}(\mathbf{r})}{g} \tag{2.21}$$

only valid for regions where $\mu > V_{\mathrm{ext}}$ and $n = 0$ elsewhere [36]. From this equation we directly calculate from the normalisation condition the chemical potential

$$\mu = \frac{\hbar\overline{\omega}}{2}\left(\frac{15Na}{a_{\mathrm{ho}}}\right)^{\frac{2}{5}}. \tag{2.22}$$

In a harmonic trap 2.1 the solution of equation 2.21 for the equilibrium density becomes

$$n(\mathbf{r}) = n(0)\left(1 - \sum_i \frac{x_i^2}{r_i^2}\right) \tag{2.23}$$

with the central density $n(0) = \mu/g$ and the radii $r_i = \sqrt{2\mu/m\omega_i^2}$. The GPE is valid at low temperatures, for large numbers of particles and dilute systems where $n\,|a|^3 \ll 1$. Because it is a mean field theory it can only describe the macroscopic behaviour of the system over distances larger than the mean separation of the particles but good agreement of the Thomas-Fermi approximation has been experimentally verified [40].

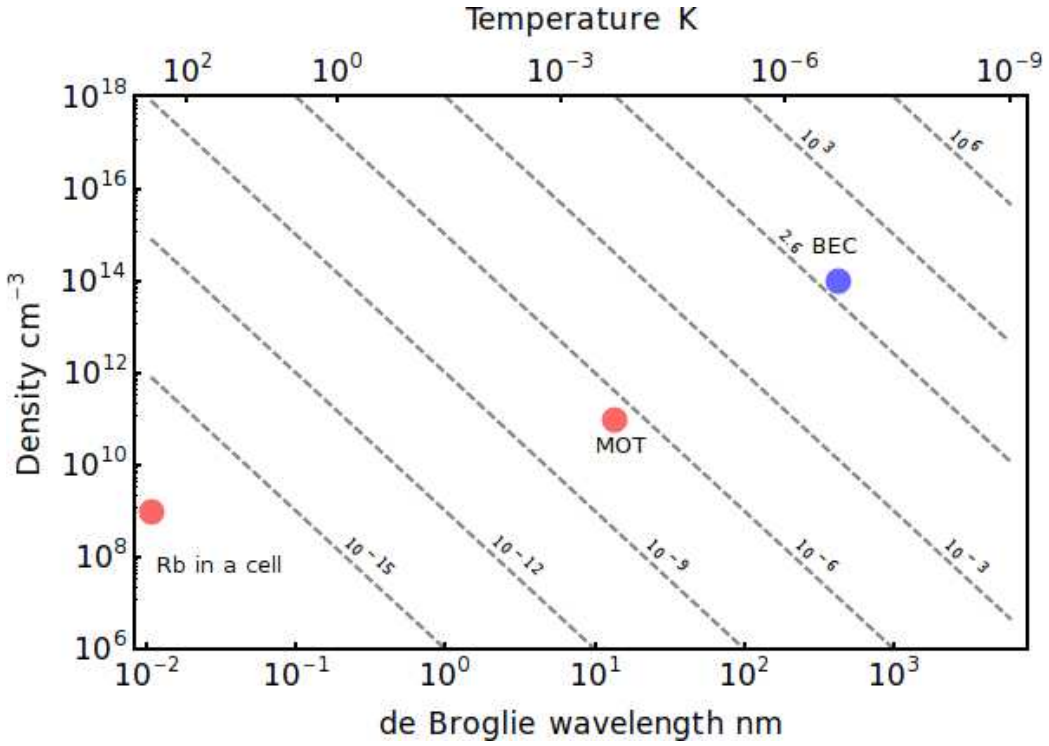

Figure 2.2: The phase space density of ^{87}Rb as a function of the density of particles and thermal wavelength. The dashed lines correspond to a constant phase space density. Bose Einstein condensation occurs above a phase space density of 2.6. The red dot on the left would be the phase space density of rubidium vapour at room temperature. The next red dot shows the phase space density in a MOT. The blue dot on the right symbolises the phase space density of a BEC.

3 Interaction of light with matter

The interaction of light with matter is the key to trap and cool neutral atoms [41, 42, 43]. Consider an atom with a transition between a ground state $|g\rangle$ and an excited state $|e\rangle$ with an angular transition frequency ω_0 and natural linewidth Γ. Further, consider this atom in a laser field of angular frequency ω_L. The two cases we will discuss are an atom in a near resonant laser field and in a laser field far detuned with respect to the atomic transition ω_0. In the former case the detuning is on the order of a few linewidhts $|\omega_L - \omega_0| \sim \Gamma$ and in the latter the detuning is on the order of $\omega_L/\omega_0 > 1$. In the former case we will see that the cooling is based on the radiation pressure [44, 45] of the light on the atom. In the second case the trapping is caused by the interaction of the laser field and an induced dipole moment of the atom creating a potential well for the atom.

3.1 Radiation pressure and Doppler cooling

With the excitation of an atom by the absorption of resonant light momentum is transferred to the atom as well. A simple model to explain the effect of radiation pressure is a two-level atom with a transition frequency ω_0 between a ground and excited state. Let us expose this system to a laser field of wavelength λ and angular frequency ω_L and let us consider the line width of the laser to be small compared to all other frequencies in this problem. Let us further consider we can detune the laser

from resonance by the amount $\Delta = \omega_L - \omega_0$, which will be negative in the following discussion. For an atom moving with velocity v in the direction of a laser beam the frequency of the laser is further shifted by the total amount $2\pi v/\lambda$, because of the Doppler effect, for a total detuning of $\Delta - 2\pi v/\lambda$. Excited atoms spontaneously decay radiatively into the ground state at a rate Γ that causes no net momentum transfer on the atom because that emission is isotropic. The photons of a laser beam of wavelength λ carry a momentum of $h/\lambda = \hbar k$. Thus, taking into account the frequency dependence and saturation of the absorption I_0[1],we can determine the average force on a moving atom in a laser beam

$$F_{\pm} = \pm\hbar k \frac{\Gamma}{2} \frac{I/I_0}{1 + I/I_0 + [2(\Delta \mp kv)/\Gamma]^2}. \tag{3.1}$$

The upper sign refers to a laser beam propagating in the positive direction, where I is the intensity and I_0 the saturation intensity, the lower sign in the negative direction. The force on an atom of two counter propagating beams is simply the sum of $F_{tot} = F_- + F_+$. Hence we find

$$F_{tot} = \hbar k \frac{\Gamma}{2} \left(\frac{I/I_0}{1 + I/I_0 + [2(\Delta - kv)/\Gamma]^2} - \frac{I/I_0}{1 + I/I_0 + [2(\Delta + kv)/\Gamma]^2} \right). \tag{3.2}$$

In figure 3.1 an example is shown for the forces F_+, F_- and the sum of both for a detuning of $\Delta = -\Gamma/2$ with Γ, m and k for ^{87}Rb. We simplify equation 3.1 by using the approximation $|kv| \ll \Gamma$ and $kv \ll |\Delta|$ to

$$F = 4\hbar k \frac{I}{I_0} \frac{k(2\Delta/\Gamma)}{[1 + (2\Delta/\Gamma)^2]^2} v \tag{3.3}$$

and see that the force is frictional and linearly proportional and opposite to the direction of the motion of the atom. This frictional force is compared to the viscous force of a particle moving in a fluid, hence this cooling is called optical molasses. The pre-factor of the velocity in equation 3.3 is the damping coefficient of this force and we simply write $F = -\alpha v$. At equilibrium the rate of cooling caused by the

[1] the saturation intensity is defined as $I_0 = \hbar\omega/\sigma\Gamma$, where ω and Γ are the frequency and lifetime of the transition and σ the resonant cross section.

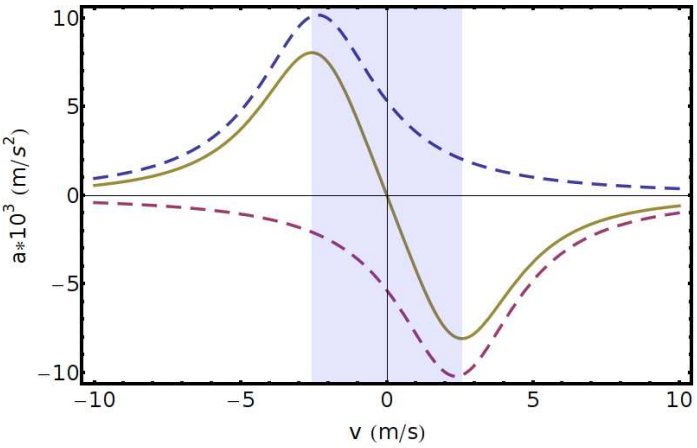

Figure 3.1: The total force F_{tot}, yellow, on an atom at velocity v of the two forces F_+, blue and F_-, red, for a detuning of $\Delta = -\Gamma/2$ and a power of $I/I_0 = 0.1$. The shadow area emphasizes the capture range.

damping of the atom's motion is the same as the heating caused by the random walk in phase space caused by the spontaneous emission of photons described by a diffusion constant D. Thus the temperature at equilibrium is given by the ratio of the diffusion constant and the damping coefficient

$$k_B T_D = \frac{D}{\alpha} = \frac{\hbar\Gamma}{4}\frac{1+(2\Delta/\Gamma)^2}{2\left|\Delta\right|/\Gamma}, \tag{3.4}$$

which has a minimum when $\Delta = -\Gamma/2$ which means

$$k_B T_{min} = \hbar\Gamma/2. \tag{3.5}$$

Thus the minimum temperature is equal to 145 μK for ^{87}Rb in the so called Doppler-cooling limit. This one dimensional scheme can be generalised in three dimensions. In a laboratory it is simply realised with three orthogonal pairs of counter propagating laser beams of equal power and detuning. The force on the atoms due to radiation pressure does not depend on the spatial position of the atoms which results in a random walk in phase space. Therefore the atoms can not be trapped and cooled in a small spatial volume. This cooling technique was proposed by Hänsch and Schalow [46] and independently by Wineland and Dehmelt [47] in 1975. Combining the force

of radiation pressure with an inhomogeneous magnetic field solves this problem as we will discuss in the next section.

3.2 Principle of the magneto optical trap

To hold our atoms in a small volume we need a restoring force towards the center of our trap. We will first discuss a simple 1D model of a magneto optical trap to demonstrate the principle of a MOT and then discuss the more complicated scheme of trapping and cooling of ^{87}Rb in a MOT.

Let us now consider a two-level atom that has a total spin of $F = 0$ in the ground state and $F' = 1$ in the excited state. The excited state is degenerate over the $m'_F = (0, \pm 1)$ manifold. The degeneracy of this manifold is lifted in a magnetic field because of the Zeeman effect. Let us consider a magnetic field with a linear gradient $B = \vec{\nabla}\mathbf{B}z$. At a position where $B \neq 0$ the sub-levels are shifted by the Zeeman effect by $\Delta E = \frac{\mu_B}{\hbar} g_{F'} m_{F'} \nabla \mathbf{B} z$. Let the polarisation of the light be circular such that with respect to the local magnetic field the beam propagating towards +z is σ^+ polarised and towards $-z$ becomes σ^- respectively (see figure 3.2). For a red detuned laser atoms at $z > 0$ will absorb more σ^- photons rather than σ^+ photons so that a net time-averaged force towards the origin of the trap is supplied to the atoms. On the other side of the origin the absorption is reversed and the atoms absorb more σ^+ photons rather than σ^- photons and therefore are directed again towards $z = 0$. This scheme can easily be generalised in three dimensions by using three pairs of counter propagating laser beams of counter-wise polarisation in a spherical quadrupole field $\mathbf{B} = B(-x/2, -y/2, z)$ as depicted in figure 3.3.

The D2 line of ^{87}Rb at $\lambda = 780$nm corresponds to transitions of the single valence electron from the $5S_{1/2}$ ground state into the excited state $5P_{3/2}$. This transition is very suitable for cooling and trapping ^{87}Rb in a magneto optical trap, because commercial diode lasers are readily available at this wavelength. The ground state

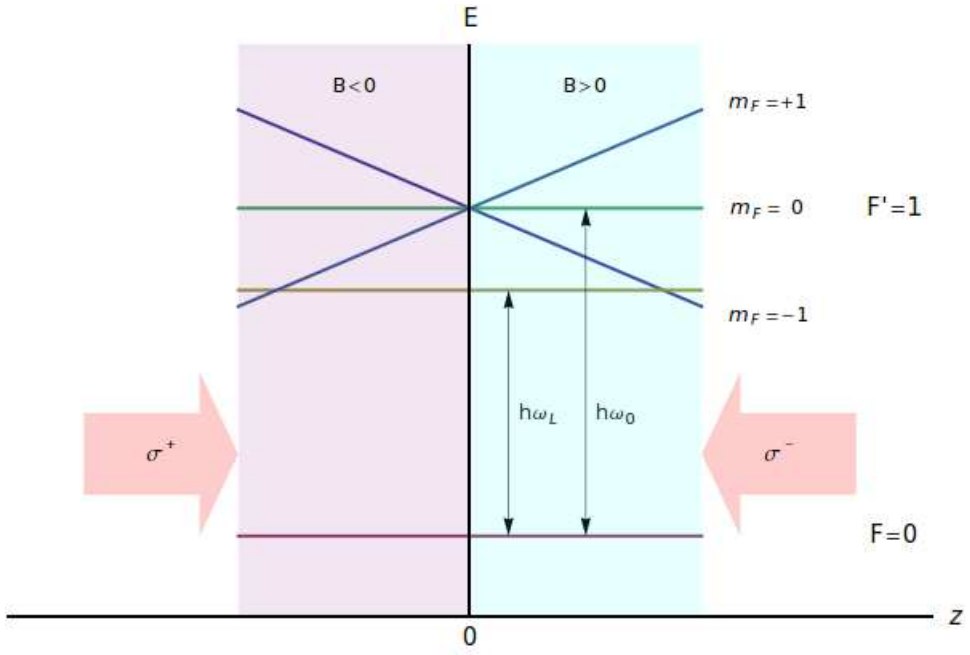

Figure 3.2: Atoms moving in the region where $B > 0$ are more likely to absorb photons from the σ^- beam and are excited into the state $F' = |1, -1\rangle$, because it is closer to the resonance of the frequency of laser ν_L. The net momentum transfer directs an atom towards the origin of the trap. The process reverses for an atom entering the region where $B < 0$.

splits into two hyperfine (compare figure 4.11) states $F = 1$ and $F = 2$. The excited state splits into four hyperfine states of $F' = 0$, $F' = 1$, $F' = 2$ and $F' = 3$. An atom in the $F' = 3$ state can only decay into the $F = 2$ level in the ground state. Therefore this closed transition is chosen for the cooling. Because of the finite line-width of a laser atoms might accidentally be exited into the $F' = 2$ state from where they may decay into the $F = 1$ hyperfine state of the ground state. In this state the atoms are not resonant to cooling light and are lost, unless they are transferred back into the cooling transition. Therefore another laser is used to excite atoms in the $F = 1$ ground state into the $F' = 2$ level of the excited state from where they decay back into the $F = 2$ level of the ground state. The force on atom in one dimension in a

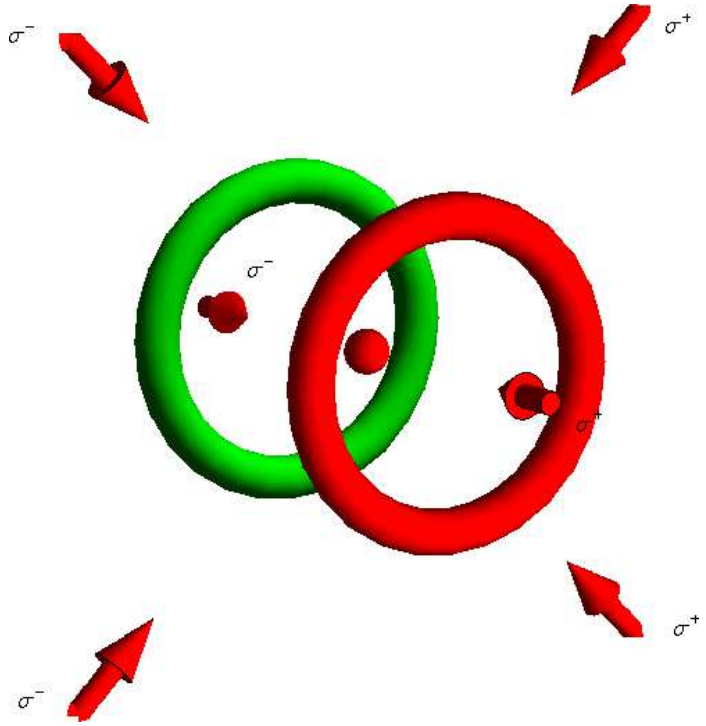

Figure 3.3: At the centre between the two coils (red and green) of opposite magnetic polarity a quadrupole field exists. The three pairs of counter propagating beams of counter wise polarisation σ^+ and σ^- intersect at the centre and form the region where the atoms are cooled and trapped.

MOT is similar to the expression in equation 3.1 plus an additional term taking the spatially dependent magnetic force $F = \mu_B dB/dz$ caused by the the gradient of the magnetic field into account. Adding the forces repelling the atom in either direction gives the total force on a moving atom in a MOT and it can be simplified to

$$F_{\mathrm{MOT}} = F_{+\mathrm{z}} + F_{-\mathrm{z}} = -\alpha \dot{z} - Kz \tag{3.6}$$

with a spring constant K and damping constant α which we know to be the equation of motion of a damped oscillator with mass m.

3.2.1 Beyond the Doppler limit

In the model of the Doppler-cooling limit that we discussed earlier (see section 3.1) we can not explain the lowest temperatures that were observed in optical molasses [48]. A more refined model of the cooling in an optical molasses was developed by J. Dalibard and C. Cohen-Tannoudji taking the polarisation of the light and multilevel structure of an real atom into account. The cooling mechanisms are described in detail in [49] and here we only want to discuss the general idea and the result. We focus on the scenario where the two counter propagating laser beams have opposite circular polarisation and we call it the $\sigma^+ - \sigma^-$ laser configuration (see figure 3.4). Our model system is a multi level system with two states $F = 1$ and $F = 2$ and in each state Zeeman sub-states ranging from $m_F = -F, ..., 0, ..., F$ (compare figure 3.5). The probability for an atom in the state $m_F = -1$ to absorb a σ^- photon propagating towards $z < 0$ is higher than to absorb a σ^+ photon propagating towards $z > 0$ and vice versus for an atom in the state $m_f = +1$. The derivation of the following argument is quite exhaustive and we refer the reader to the detailed discussion in [49]. Absorbing more photons from one of the beams than the other leads to an imbalance of the radiation pressure and also a difference of the populations in the ground states. To find the temperature at equilibrium we compare the diffusion constant and the damping coefficient and find that the limit of the temperature in this model comes to

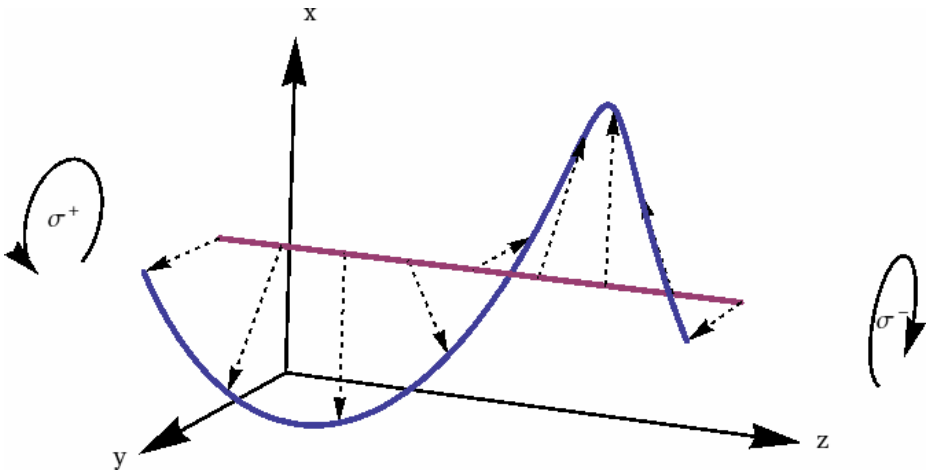

Figure 3.4: Two counter propagating lasers of opposite circular polarisation, $\sigma^+ - \sigma^-$ configuration, interfere to produce a field with a rotating linear polarisation (dashed arrows).

the recoil limit of one absorbed photon e.g. $k_B T = \hbar^2 k^2 / 2m$ with a theoretical limit of 180nK for ^{87}Rb.

3.2.2 Dynamics of the population in the MOT

Let us now consider a simple model to describe the growth and decay of the number of atoms being trapped in a MOT. Let us assume that atoms below a critical velocity are loaded into the MOT at a rate Φ. Further let us assume that atoms are lost from the trap because of two-body collisions of trapped atoms at a rate $\beta\ n^2(\vec{\mathbf{r}}, t)$ and collisions with a remaining background gas of other species at a rate γ. The rate equation for the number of atoms in the trap is given by [50, 51, 52, 53]

$$\frac{dN(t)}{dt} = \Phi - \gamma N - \beta \int n^2(\vec{\mathbf{r}}, t) d^3 r \tag{3.7}$$

where $n(\vec{\mathbf{r}}, t)$ is the density distribution of the trapped atoms. The number of atoms in the trap is determined by the balance between the loading rate and the loss rate of the trap. Therefore the number of atoms reaches a maximum, when the loading rate equals the total rate of losses. At this point the number of atoms in the MOT

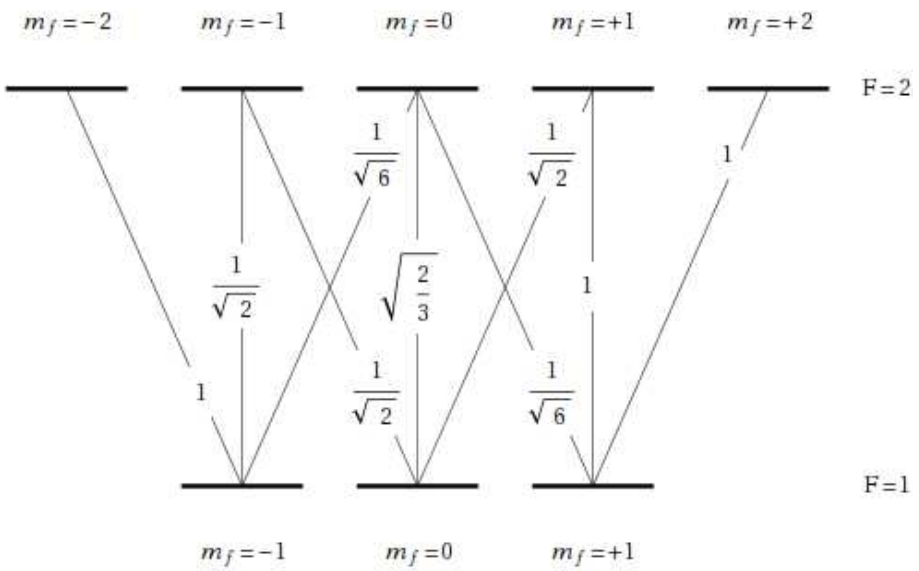

Figure 3.5: Atomic level scheme for a $F = 1 \leftrightarrow F = 2$ transition. Along the transitions indicated by the thin lines are the Clebsh-Gordon coefficients.

is constant in time and the density becomes time in dependent and is approximated by $n(\vec{\mathbf{r}}, t) = n_s(\vec{\mathbf{r}})$ in the radiation trapping limit [50, 54, 55] and equation 3.7 can be written as

$$\frac{dN}{dt} = \Phi - (\gamma + \beta\ n_s)N. \tag{3.8}$$

The integration of equation 3.8 is not difficult and we find a simple expression for the solution

$$N(t) = A(1 - e^{-Bt}) = N_{\max}(1 - e^{-t/\tau}) \tag{3.9}$$

with $A = \Phi/(\gamma + \beta\ n_s)$ and $B = \gamma + \beta\ n_s$. If one assumes that the losses of atoms from the MOT are dominated by collisions of the background of the same species, e.g. $\beta\ n_s \gg \gamma$, we can estimate the loss rate and therefore find an expression for the number of particles in the stationary limit. The loss rate can then be estimated by [56] $1/\tau = n\sigma(3kT/m)^{\frac{1}{2}}$, where σ is the collisional cross section between an atom of the background gas to eject trapped atoms from the MOT and m the mass of the atoms. For the maximum number of trapped particles, reached at $\gamma = 0$, we find $N_{\max} = \Phi/(\beta\ n_s) = \Phi\tau$. If no more atoms are loaded into the MOT, e.g. $\Phi = 0$, the

stationary MOT will decay exponentially as

$$n(t) = n_s \, e^{-t/\tau} \tag{3.10}$$

where τ is a time constant given by loss mechanisms as discussed.

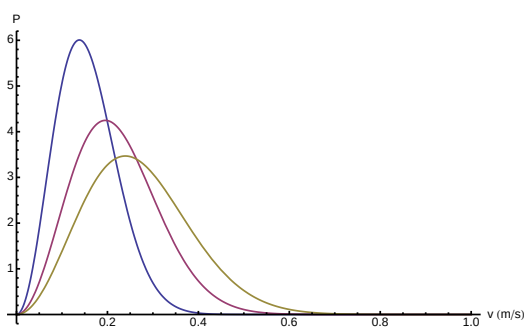

(a) Maxwell probability distribution for three different temperatures $T = \{100\mu\text{K}, 200\mu\text{K}, 300\mu\text{K}\}$, $\{\text{blue}, \text{red}, \text{yellow}\}$

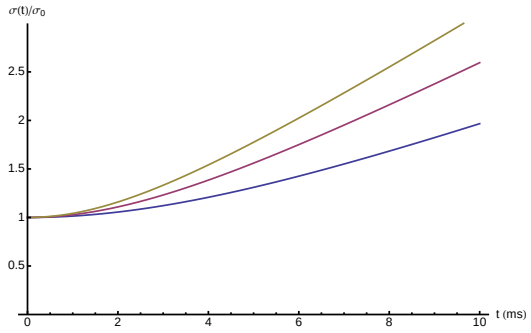

(b) Expansion of ensembles of same initial size for three different temperatures $T = \{100\mu\text{K}, 200\mu\text{K}, 300\mu\text{K}\}$, $\{\text{blue}, \text{red}, \text{yellow}\}$

Figure 3.6: The most probable velocity $\tilde{v}$ depends on the temperature T, see figure 3.6(a), and determines the expansion of the ensemble see 3.6(b).

3.2.3 Temperature of trapped atoms in a MOT

The velocity distribution of the thermal atoms trappen ina MOT obey the Maxwell-Boltzmann distribution with the most probable speed $\tilde{v} = \sqrt{2\text{k}_\text{B}T/m}$, with the Boltzmann constant k_B, the mass m of the atom and temperature T. About 60% of atoms are within the range of zero velocity and the most probable velocity $\tilde{v}$. The trapped ensemble will expand when released from the trap proportional to the square root of the temperature of the ensemble. To estimate the temperature one has to measure the initial size of the density distribution and the size at different times after being released from the trap. The density distribution is Gaussian $n(z) = n_s\text{exp}(-\text{z}^2/\sigma_\text{z})$, where σ_z is defined as the $1/e$ radius along the z direction. During the expansion the size will grow by $\tilde{v}\Delta t$ in a time interval Δt. The size of the cloud of cold atoms as a function of time is given by

$$\sigma(t) = \sqrt{\sigma_0^2 + (\tilde{v}\Delta t)^2}. \tag{3.11}$$

From fitting this equation to experimental data we can estimate the temperature of the MOT. In a simple model where we are not taking polarisation effects into account

we can derive a temperature limit in a MOT. The two counterparts in a MOT are the spontaneous emission and stimulated absorption. For equal contributions in a low saturation limit we find the so called Doppler limit which is given by $T = \hbar\Gamma/2/k_{\mathrm{B}}$ which is 145μK for ^{87}Rb. A typical density in a MOT is on the order of $10^{11}\mathrm{cm}^{-3}$ and assuming a temperature near the Doppler limit results in a phase space density on the order of 10^{-5} still five orders of magnitude away from the onset of Bose-Einsteincondensation.

3.3 The optical dipole force

In 1970 A. Ashkin successfully trapped micro-particles in a strongly focused laser beam [57]. With this achievement the idea of trapping neutral atoms was born and proposed by V.S. Letokhov [58] and A, Ashkin [59]. The trapping potential of an optical dipole trap is conservative, as we will see later, and therefore the atoms are not cooled in such a trap. By cooling atoms in a MOT or using molasses cooling one can load cold atoms into an optical dipole trap [60] and [61]. Since then the dynamics of the loading of optical dipole traps has been investigated in more detail[62, 63, 64]. Reaching high densities trapped atoms is the key to achieve quantum degeneracy which was demonstrated by M.D.Barrett in 2001 [20].

In the following sections we will discuss the theoretical concepts of trapping neutral atoms in an optical dipole trap. First we will look at a simple two-level systems which we will later extend taking multiple levels into account and refine the model for ^{87}Rb. Later we will discuss the dynamics of trapped atoms in an optical dipole trap and will focus on the trapping potential of a crossed optical dipole trap taking gravity into account.

3.3.1 Oscillator model of a two-level system

Let us describe the light of a laser by an electric field of amplitude $|\tilde{E}|$ by $\mathbf{E}(\mathbf{r},t) = \tilde{\mathbf{e}}\tilde{E}\exp(-i\omega t) + c.c.$, with the unit polarisation vector $\tilde{\mathbf{e}}$ and frequency ω. The time dependent electric field will induce an oscillating dipole moment $\mathbf{p}(\mathbf{r},t) = \tilde{\mathbf{e}}\ \tilde{p}\ \exp(-i\omega t) + c.c.$ in an atom put into this field. The amplitude of the dipole moment is given by the simple equation

$$\tilde{p} = \alpha\tilde{E}, \tag{3.12}$$

where α denotes the complex polarisability, which is a function of the frequency ω of the driving electric field. The induced dipole moment interacts with the driving field and the potential of this interaction is given by

$$U_{\mathrm{dip}} = -\frac{1}{2}\langle\mathbf{p}\cdot\mathbf{E}\rangle = -\frac{1}{2\epsilon_0 c}Re(\alpha)I, \tag{3.13}$$

where the angular brackets denote the time average over the rapid oscillating terms, $I = 2\epsilon_0 c\left|\tilde{E}\right|^2$ is the field intensity. The factor $\frac{1}{2}$ takes into account that the dipole moment is an induced rather than a permanent one. The resulting dipole force results from the gradient of the interaction potential

$$F_{\mathrm{dip}}(\mathbf{r}) = -\nabla U_{\mathrm{dip}}(\mathbf{r}) = \frac{1}{2\epsilon_0 c}\mathrm{Re}(\alpha)\nabla I(\mathbf{r}). \tag{3.14}$$

The power absorbed by an atom in the driving field is given by

$$P_{\mathrm{abs}} = \langle\dot{\mathbf{p}}\cdot\mathbf{E}\rangle = 2\omega\mathrm{Im}(\tilde{p}\tilde{E}) = \frac{\omega}{\epsilon_0 c}\mathrm{Im}(\alpha)I. \tag{3.15}$$

Describing the driving electric field as a stream of photons with energy $\hbar\omega$, that are absorbed and spontaneously remitted by the atoms the scattering rate is given by

$$\Gamma_{sc}(\mathbf{r}) = \frac{P_{\mathrm{abs}}}{\hbar\omega} = \frac{1}{\hbar\epsilon_0 c}\mathrm{Im}(\alpha)I(\mathbf{r}). \tag{3.16}$$

Solving these equations, considering the atom behaves like a classical oscillator (as in Lorentz's model) gives a simple and useful picture. In this picture the electron

is bound elastically to the nucleus and oscillates with its eigenfrequency ω_0. The dipole radiation of the oscillating electron causes damping according to Larmor's well-known formula. This approach is valid for low saturation and low scattering rates and provides a good approximation for the D lines of alkali metals [65]. With these assumption we find following expressions for the dipole potential and scattering rate

$$U_{\mathrm{dip}}(\mathbf{r}) = -\frac{3\pi c^2}{2\omega_0^3}\left(\frac{\Gamma}{\omega_0-\omega}+\frac{\Gamma}{\omega_0+\omega}\right) I(\mathbf{r}) \tag{3.17}$$

$$\Gamma_{sc}(\mathbf{r}) = \frac{3\pi c^2}{2\hbar\omega_0^3}\left(\frac{\omega}{\omega_0}\right)^3\left(\frac{\Gamma}{\omega_0-\omega}+\frac{\Gamma}{\omega_0+\omega}\right)^2 I(\mathbf{r}). \tag{3.18}$$

Let $\Delta = \omega - \omega_0$ be the detuning, then two essential points can be seen:

1. *Sign of detuning:* For a negative detuning or below an atomic resonance, the interaction becomes attractive and the potential minima are found at positions of maximum intensity.

2. *Scaling with intensity and detuning:* Usually optical dipole traps (ODT) operate at high intensities and large detuning to minimise the scattering rate. The potential scales as I/Δ, whereas the scattering rate scales as I/Δ^2.

The further the detuning the lower the scattering rate, but the more power one has to apply in order to provide sufficiently deep traps. A wide range of suitable lasers are commercially available. For the author's work a 20W fiber laser at a wavelength of 1064nm was chosen. In the next sections we will focus on general considerations and the design of an optical dipole trap.

3.3.2 Multi-level atoms

In the previous paragraph we introduced the concept of the optical dipole force using a simple two level model of one ground and one excited state. For a multi-level atom

the general conclusion remains unchanged i.e. the sign of the detuning determines the interaction and the scaling of the dipole force (scattering rate) as a function of the intensity over the detuning. In a real atom the electronic transitions exhibit a complex structure of many sub-levels. Instead of describing a multi-level system with state dependent polarisabilities, we will use the picture of dressed atoms, which was developed by Dalibard and Cohen-Tannoudji [66]. In a far-detuned laser field the atomic levels are perturbed which can be treated by second order perturbation theory of the laser field (linear terms of the field intensity). Thus we find from second-order time-independent perturbation theory with an interaction Hamiltonian $\mathcal{H}_1$, that the i-th state is shifted in its energy by

$$\Delta E_i = \sum_{j \neq i} \frac{|\langle j | \mathcal{H}_1 | i \rangle}{\mathcal{E}_i - \mathcal{E}_j} \tag{3.19}$$

if the states are non-degenerate. Similar to the two-level approach the interaction of the atom with the laser field is described by the interaction Hamiltonian $\mathcal{H}_1 = -\hat{\mu}\mathbf{E}$. The description of the energy states $\mathcal{E}_i$ is the combined system of the energy of the atom plus the total energy of the field. For an atom in its ground state the internal energy is zero and the field of n photons has an energy of $n\hbar\omega$. Therefore we find the total energy to be $\mathcal{E}_i = n\hbar\omega$. By absorbing a photon from the field the atom transfers energy to the excited state with an internal energy of $\hbar\omega_0$ leaving the field energy to be $(n-1)\hbar\omega$, thus the total energy is $\mathcal{E}_j = \hbar\omega_0 + (n-1)\hbar\omega = -\hbar\Delta_{ij} + n\hbar\omega$. Applying the previous results to a two level system yields the same result as we found before in the semiclassical approach

$$\Delta E = \pm \frac{|\langle e|\mu|g\rangle|}{\Delta} |E|^2 = \pm \frac{3\pi c^2}{2\omega_0^3} \frac{\Gamma}{\Delta} I. \tag{3.20}$$

This optically induced shift, also known as the AC Stark shift, shifts the energy states of the ground and excited states in opposite directions. The case of low saturation is interesting, because the atom will stay in the ground state most of the time. In a spatially inhomogeneous light field like given by a Gaussian laser beam the shift of the

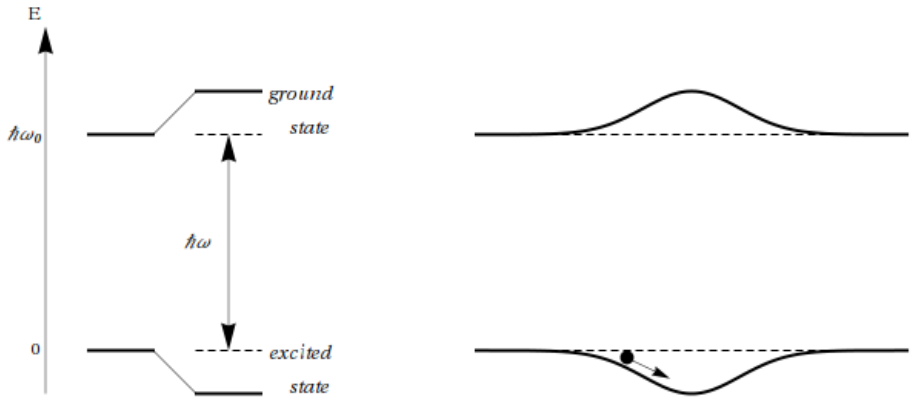

Figure 3.7: Shifts of the energy levels in a two-level system. On the left hand side, red detuned light $\Delta < 0$ lowers the energy of the ground state and raises the energy of the excited state. Right hand side, in a spatially inhomogeneous laser field the atom will seek the lowest point of the potential i.e. the region of highest intensity an can therefore be trapped.

energy depends on the position of the atom in the laser beam and therefore it 'sees' a potential well. The case of a two-level system in a red detuned laser field is plotted in figure 3.7 in which an atom in the ground state lowers its energy at the point of the highest intensity of a spatially inhomogeneous laser. Knowing all electronic states involved in a multi-level system one has to calculate all dipole matrix elements $\mu_{ij} = \langle e_j|\mu|g_i\rangle$. These elements can be written as the product of a reduced matrix element $||\mu||$ and a real coefficient c_{ij}. The real coefficients describe the coupling strength of the two states. The energy shift of the ground state $|g\rangle$ can be written as

$$\Delta E = \frac{3\pi c^2 \Gamma}{2\omega_0^3} I \sum_j \frac{c_{ij}^2}{\Delta_{ij}}, \tag{3.21}$$

where we carry out the summation over all the electronically excited states $|e_J\rangle$.

Dipole potential for Rubidium

Let us now have a closer look at ^{87}Rb which we use in our experiment. The nuclear spin of ^{87}Rb is $I = 3/2$. The well known D line doublet is caused by the spin-

orbit coupling and the two lines are related to the transitions from the ground state $^2S_{1/2}$ to the two excited states $^2P_{1/2}$ and $^2S_{3/2}$ with an energy splitting $\hbar\Delta'_{FS}$. The hyperfine structure is caused by the coupling to the nucleus which leads to a splitting of $\hbar\Delta_{HFS}$ and $\hbar\Delta'_{HFS}$ for the ground and excited state. The relevance of these levels is $\Delta'_{FS} \gg \Delta_{HFS} \gg \Delta'_{HFS}$. Starting from equation 3.21 we can derive a more general result for the ground state for large detunings compared to the hyperfine splitting of the excited states. The potential for an atom in the ground state of total angular momentum F and magnetic quantum number m_F in a laser field is given by

$$U_{dip}(\mathbf{r}) = \frac{\pi c^2 \Gamma}{2\omega_0^3} \left(\frac{2 + \mathcal{P} g_F m_F}{\Delta_{2,F}} + \frac{1 - \mathcal{P} g_F m_F}{\Delta_{1,F}} \right) I(\mathbf{r}), \tag{3.22}$$

where g_F is the Landé factor and $\mathcal{P}$ takes into account the polarisation of the light ($\mathcal{P} = 0, \pm 1$ for linear and circular $\sigma^{\pm}$ polarised light respectively). Therefore the terms in the brackets are the contributions of the D_2 and D_1 line with the detunings $\Delta_{2,F}$ and $\Delta_{1,F}$ with respect to the centre of each transition. Thus for ^{87}Rb and linear polarised light at a wavelength of $\lambda = 1064$nm we can write $U_{dip}(\mathbf{r}) = U_0 \cdot I(\mathbf{r})$, where $U_0 \sim -1.826 \cdot 10^{-36} \mathrm{m}^2\mathrm{s}$

3.3.3 Neutral atoms in a focused Gaussian beam

So far in our discussion we hace not considered any further constraints on the intensity. A focused laser beam with a Gaussian spatial intensity distribution (see figure 3.8(a) and 3.8(b)) with power P propagating along the z-axis is given by

$$I(r, z) = \frac{2P}{\pi w^2(z)} \exp\left(-2 \frac{r^2}{w^2(z)} \right) \tag{3.23}$$

with radial coordinate r. The radius of the beam w is defined along the radial direction, where the intensity has decreased to $1/e^2$ and varies along the axial direction z (see figure 3.8(b)) according to

$$w(z) = w_0 \sqrt{1 + \left(\frac{z}{z_R} \right)^2} \tag{3.24}$$

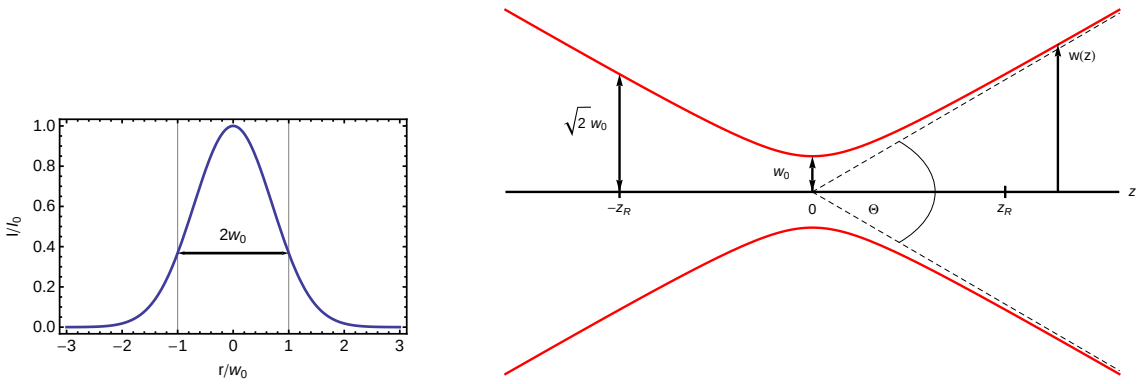

(a) Intensity profile of Gaussian laser beam at the waist.

(b) Beam profile ($1/e^2$) of a focused Gaussian laser along the axis of propagtion.

Figure 3.8: Beam profile of a focused Gaussian laser beam. The smallest radius w_0 is at the focus of the beam. At the distance of the Rayleigh length z_R the area of the beam is twice as big as in the focus.

where $z_R = \pi w_0^2 \lambda$ denotes the Rayleigh length and w_0 the smallest waist of the beam at the focus of the beam. It is also the place, where we define the depth of the trap $U_0 = U(r = 0, z = 0)$. The dipole potential of neutral atoms in a focused Gaussian laser beam is well approximated with a Taylor series if the kinetic energy $k_\mathrm{B}T$ of the atomic ensemble is much smaller than the depth of the trap. Truncating the series for higher orders than two, yields the harmonic approximation and we find for the optical dipole potential the simple expression

$$U(r,z) = -U_0 \left(1 - 2\left(\frac{r}{w_0}\right)^2 - \left(\frac{z}{z_R}\right)^2\right). \tag{3.25}$$

At the bottom of the trap the atoms oscillate with frequencies

$$\omega_r = \sqrt{\frac{4U_0}{m w_0^2}} \tag{3.26}$$

$$\omega_z = \sqrt{\frac{2U_0}{m z_R^2}} \tag{3.27}$$

along the radial and axial directions, where m is the mass of the atom. The geometry of the trap is determined by the aspect ratio which can easily be found by taking the ratio of the radial over the axial frequencies

$$\frac{\omega_r}{\omega_z} = \sqrt{2}\frac{z_\mathrm{R}}{w_0} = \sqrt{2}\frac{\pi w_0}{\lambda}. \tag{3.28}$$

Therefore the confinement in a single beam is stronger along the radial direction and weaker along the axial direction.

For convenience energies are often converted into a temperature equivalent by simply dividing the energy of the potential U_0 by the Boltzmann constant k_B. The useful picture we can derive from this is that atoms which are hotter than the depth of the trap can not be trapped. The dipole potential for ^{87}Rb in a focused Gaussian laser beam is shown in figure 3.9. The solid red line shows the $1/e^2$ beam profile along the axis of propagation (z-direction). The dashed lines show equipotential lines of the trap in units of $T = U_0/k_\mathrm{B}$. Note the difference of the dimensions of a factor 100 on the radial and axial directions (r and z -directions). This is a consequence of the ratio of the two trapping frequencies which we found in equation 3.28 to be $\sqrt{2}\frac{z_\mathrm{R}}{w_0} = \sqrt{2}\frac{\pi w_0}{\lambda} = 112.7$ for a waist of 27μm we used for the calculation in figure 3.9. The depth of the trap, and therefore the scattering rate, scales linearly in power but with the inverse square root of the waist (compare equation 3.25). As we can see in figure 3.10 a deeper trap is found for a smaller waist but also a higher scattering rate. On the other hand a larger waist at the same power means a lower scattering rate but also a shallower potential. Regardless, the scattering rate is on the order of a few Hz at high powers and is not of concern and can be neglected for far red detuned traps. Other loss mechanisms (as we will see in chapter 6) happen at a faster rate and the power is reduced from tens of W to a few mW in a few seconds. The radial and axial trapping frequencies are shown in figure 3.11 at the centre of the trap. Again we emphasize the difference of a factor of 112.7 between the frequencies in the two directions.

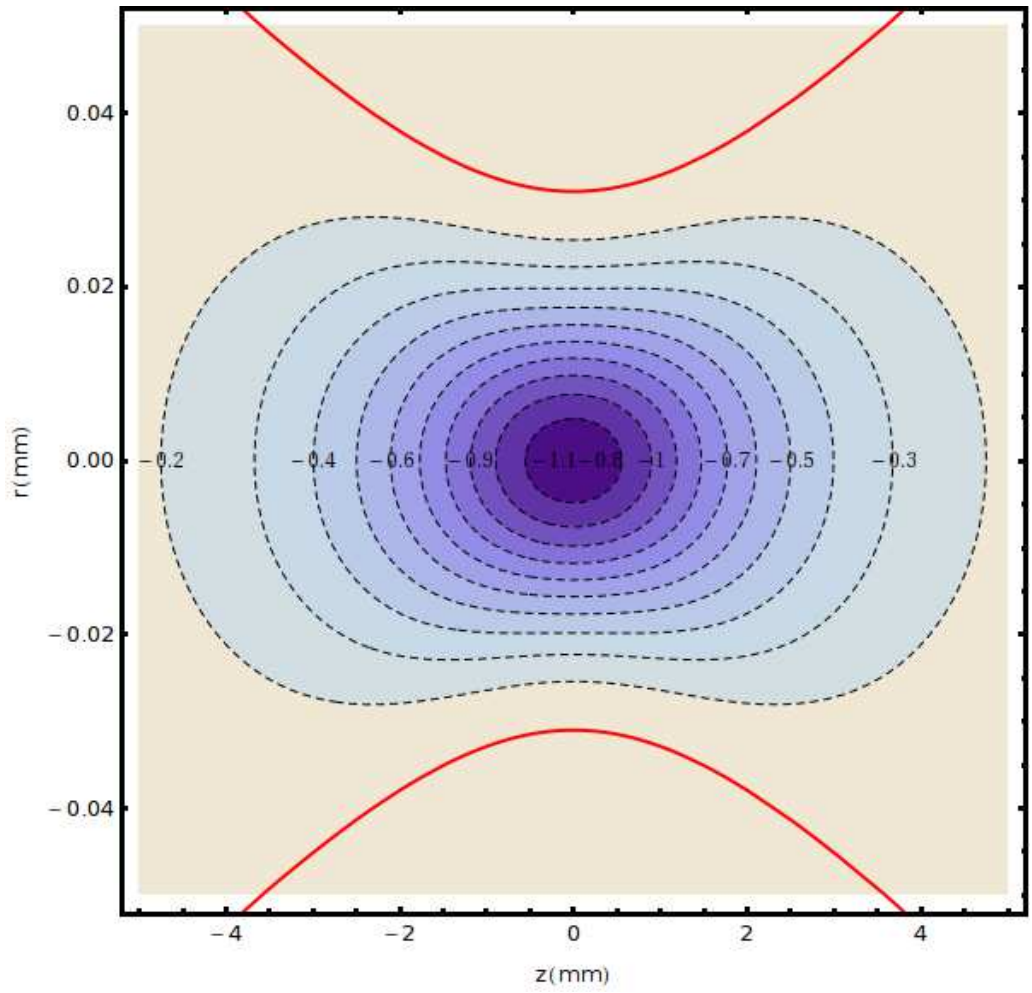

Figure 3.9: Beam profile of a focused Gaussian laser beam wavelength 1064nm and $w_0 = 27\mu$m (red lines). The dashed lines are equipotential lines of the potential energy of the optical dipole trap for ^{87}Rb at a power of $P = 10$W in units of a temperature equivalent to $E/k_B = T(\mu K)$.

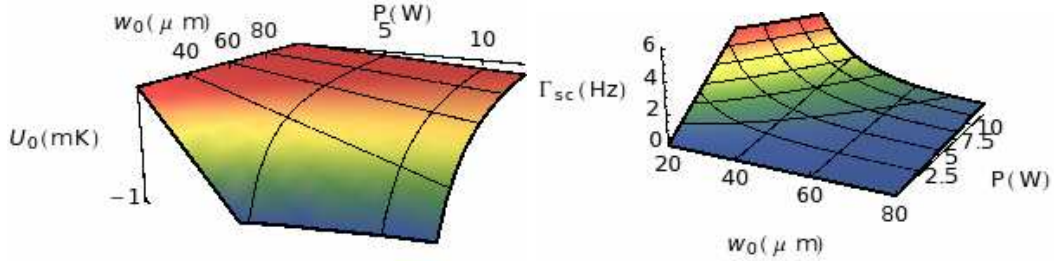

(a) Trap depth $U_0(P, w)$ as a function of the waist w_0 and power P.

(b) Scattering rate $\Gamma_{\mathrm{sc}}(P, w)$ as a function of the waist w_0 and power P.

Figure 3.10: On the left hand side the depth of the trap as a function of the power and waist of the laser beam. On the right hand side the scattering rate as a function of power and waist of the laser beam.

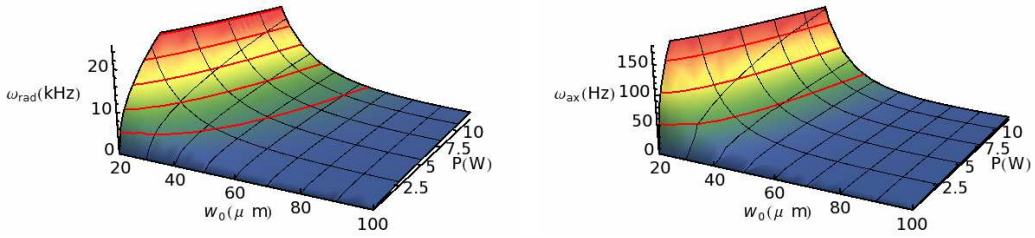

(a) The radial trap frequency as a function of the waist w_0 and power P.

(b) The axial frequency as a function of the waist w_0 and power P.

Figure 3.11: The radial and axial trapping frequencies as a function of the power and the waist in a single beam trap.

3.3.4 Crossed dipole trap

Thermalisation of the trapped atoms is governed by the two body-collision rate which depends on the geometry of the trap. The weak confinement in a single beam trap along the axial direction dilutes the density of the atoms at the centre of the trap and reduces therefore the two-body collision rate. By overlapping two optical dipole traps the weak direction is combined with the strong direction of the other. The confinement is therefore stronger in each direction. In order to avoid interference between two beams of the same wavelength one has to make sure that their polarisations are orthogonal. The intensities of two beams of the same wavelength propagating along the x-direction and y-direction with different powers and waists are:

$$I(x,y,z) = \frac{2P_x}{\pi w(x)^2}\exp\left(-2\frac{y^2+z^2}{w(x)^2}\right) + \frac{2P_y}{\pi w(y)^2}\exp\left(-2\frac{x^2+z^2}{w(y)^2}\right). \tag{3.29}$$

The trapping frequencies in each direction in such a trap are then given by

$$\omega_x = \sqrt{-\frac{8U_0}{\pi m}\left(\frac{P_y}{w_{0,y}^4} + \frac{P_x}{2w_{0,x}^2 x_\mathrm{R}^2}\right)} \tag{3.30}$$

$$\omega_y = \sqrt{-\frac{8U_0}{\pi m}\left(\frac{P_x}{w_{0,x}^4} + \frac{P_y}{2w_{0,y}^2 y_\mathrm{R}^2}\right)} \tag{3.31}$$

$$\omega_z = \sqrt{-\frac{8U_0}{\pi m}\left(\frac{P_y}{w_{0,y}^4} + \frac{P_x}{w_{0,x}^4}\right)}. \tag{3.32}$$

These equations give the same result as the equations 3.27 and 3.26 of a single beam trap if we consider the power of one beam to be zero. The second terms in ω_x and ω_y depend on the Rayleigh length and are only important at lower powers.

3.3.5 Gravity

The acceleration of $g = 9.81 m/s^2$ caused by gravity causes an additonal linear potential along the direction of gravity, which can be neglected for deep traps such $U_0(z) \gg mgz$. For shallower traps the geometry becomes more anharmonic and for too little power we can not trap atoms against gravity in our trap. In figure 3.12 the

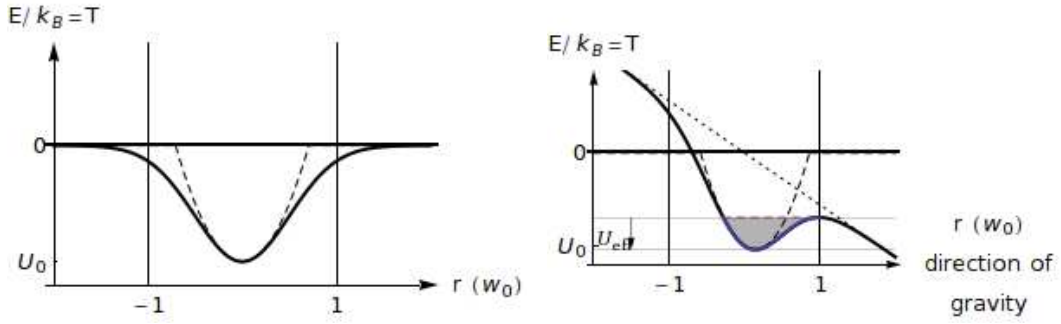

(a) Optical dipole potential without gravity, see equation 3.25.

(b) Optical dipole potential with gravity, see equation 3.33.

Figure 3.12: The optical dipole potential at low power not taking into account the influence of gravity (figure:3.12(a)) and for same beam parameters taking gravity into account (figure:3.12(b)). The dashed line in both plots shows the harmonic approximation.

potential produced by the optical dipole force is shown for one and the same beam parameters (power, waist and wavelength). The left hand figure 3.12(a) shows the potential neglecting gravity, whereas the right hand figure 3.12(b) shows the combined potential. Quite remarkable is the anharmocity of the potential as well as the fact that the effective trap depth is not anymore given by the difference from $U = 0$ to $U(0) = U_0$ or the constant term in the series approximation. The effective depth of the trap is given by the potential minimum which is slightly shifted from the origin and the local maximum (shaded area in figure 3.12(b))

$$U_z = mgz + U_0 I(0, 0, z) \tag{3.33}$$

3.3.6 Parametric heating

As we will see in Chapter 4 (see section 4.7) the power and the waist diameter are quite important parameters as they are used to determine the temperature and phase

space density. The equations 3.26 and 3.27 allow us to determine the frequencies for a given power and waist. With the technique of parametric heating [67, 68] one modulates periodically the power of the trapping beam varying the frequency of the modulation. Due to the energy transfer the atoms are heated and the loss of atoms from the trap is resonantly enhanced at harmonics $\omega_n = 2\omega_r/n$ (n integer) of the unperturbed trapping frequency ω_r. By identifying these resonances and rearranging (3.27) and (3.26) one can determine the waist and Rayleigh length of the trapping beam. The equation of motion for a parametrically driven oscillator with damping is given by

$$\ddot{x} + \beta(t)\dot{x} + \omega(t)^2 x = 0 \tag{3.34}$$

with the damping coefficient $\beta(t)$ and frequency $\omega(t)$. Periodic modulation of the eigenfrequency $\omega^2(t) = \omega_0^2\ [1 + a_0\ \sin(\omega_m t)]$, with amplitude a_0 and frequency ω_m of the modulation, causes an exponential increase of the energy of the oscillator for driving frequencies near $2\omega_0$ and other subharmonics at $2\omega_0/n$. Near the resonance the profile is well described by a Lorentz profile:

$$f(\nu) = \frac{1}{\pi}\ \frac{\Gamma}{\Gamma^2 + (\omega - \omega_0)^2} \tag{3.35}$$

with the position of the resonance at ν_0 and a line width of the resonance Γ. We can use this technique in a single beam as well in a crossed optical dipole trap to determine the waists (e.g. the geometry) at the centre of the trap.

3.3.7 Growth and decay of the number of atoms in a ODT

Collisions among the atoms determine the lifetime of the trap which we define as the time taken to reach the 1/e level of our initial number of atoms in the trap. One loss mechanism is collisions of a trapped atom with highly energetic atoms from the background gas where we lose one trapped atom. Collisions among two atoms -two body collisions- redistributes the energy and converts the internal energy into kinetic energy and loss of an atom may occur after the collision. At higher densities

the collision of the atoms -three body loss- has to be taken into account. Three colliding atoms may form a molecule and transfer the binding energy onto the third atom and both molecule and atom are lost from the trap. The photon scattering is not mentioned here, as it is much smaller than all other loss mechanisms. All three mechanisms are described by the following differential equation [62]:

$$\frac{dN}{dt} = -\Gamma N - \beta N^2 - \gamma N^3 \tag{3.36}$$

where Γ, β and γ are the coefficients for

Γ collisions with highly energetic atoms from the background gas

β collisions among two trapped atoms

γ three trapped colliding atoms.

In the limit of low densities ($n < 10^{12}\mathrm{cm}^{-3}$) we take only the one body and two body mechanisms into account and a solution of equation (3.36) is given by

$$N(t) = N_0 \, \frac{\mathrm{e}^{-\Gamma t}}{1 + \left(\frac{\beta N_0}{\Gamma}\right)\left(1 - \mathrm{e}^{-\Gamma t}\right)}. \tag{3.37}$$

Typical decays of the population in an optical dipole trap is shown in figure 6.8 at different stages of the evaporation.

3.3.8 Potential of a crossed ODT taking gravity into account

In this section we want to discuss the potential of a crossed dipole trap crossing at a slight angle, their foci not intersecting at the same point and taking gravity into account. We assume one beam propagating along the x-direction and a second beam along the y-direction under a slight angle β and gravity along the z-direction. The first beam is given by

$$U(x,y,z) = U_0 \frac{2P_1 \exp\left(-\frac{2((x-x_0)^2+z^2)}{w_1^2\left(1+\frac{(x-x_0)^2}{x_R}\right)}\right)}{w_1^2\left(1+\frac{(x-x_0)^2}{x_R}\right)} \tag{3.38}$$

where y and z are the transverse directions of the beam and x_0 an offset to the spatial position of the waist. The second beam is rotated under a slight angle Θ and with the new coordinates

$$x' = x\ \cos(\beta) \tag{3.39}$$

$$y' = y\ \sin(\beta) \tag{3.40}$$

the second beam is given by

$$U(x,y,z) = U_0 \frac{2P_2 \exp\left(-\frac{2\left(((x-x_0)\cos(\beta)-(y-y_0)\sin(\beta))^2+z^2\right)}{w_2^2\left(\frac{((y-y0)\cos(\beta)-(x-x_0)\sin(\beta))^2}{y_{\mathrm{R}}^2}+1\right)}\right)}{\pi w_2^2\left(\frac{((y-y_0)\cos(\beta)-(x-x_0)\sin(\beta))^2}{y_{\mathrm{R}}^2}+1\right)} \tag{3.41}$$

where x and z are the transverse directions of the beam and $(x_0, y0)$ an offset to the spatial position of the waist. The spatial geometry of the beams is show in figure 3.13 which is the given geometry in our experiment (see figure 3.14). The beams intersect under a slight angle due room constraints in our set up. The combined potential is given by:

$$U(x,y,z) = \tag{3.42}$$

$$U_0\left(\frac{2P_1\exp\left(-\frac{2((x-x_0)^2+z^2)}{w_1^2\left(1+\frac{(x-x_0)^2}{x_R}\right)}\right)}{w_1^2\left(1+\frac{(x-x_0)^2}{x_R}\right)} + \frac{2P_2\exp\left(-\frac{2\left(((x-x_0)\cos(\Theta)-(y-y_0)\sin(\Theta))^2+z^2\right)}{w_2^2\left(\frac{((y-y_0)\cos(\Theta)-(x-x_0)\sin(\Theta))^2}{y_{\mathrm{R}}^2}+1\right)}\right)}{\pi w_2^2\left(\frac{((y-y_0)\cos(\Theta)-(x-x_0)\sin(\Theta))^2}{y_{\mathrm{R}}^2}+1\right)}\right)$$

$$+ mgz.$$

For this spatial geometry we can calculate the optical dipole potential taking gravity into account. In figure 3.15 we show the potential with following parameters for O1:($P_1 = 0.03W, w_0 = 27\mu m, \lambda = 1064nm$) and O2($P_1 = 0.03W, w_0 = 30\mu m, \lambda = 1064nm$) an angle of 76° and a displacement of the focus of O1 of $x_{\mathrm{off}} - 0.2z_{\mathrm{R1}}$. Again we estimate the trapping frequencies according to the harmonic approximation which

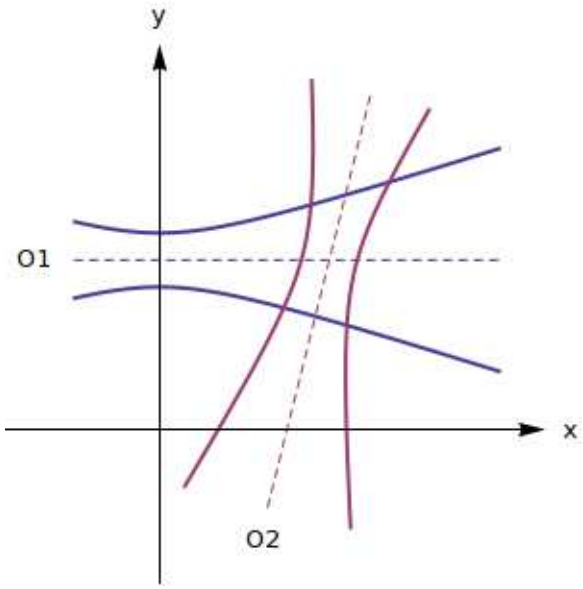

Figure 3.13: Two traps are propagating along the blue and pink lines which show the $1/e^2$ radii of two focused laser beams in the x-y plane perpendicular to gravity. The angle between the propagation axes is 76° and the focus of O1 is offset by $2z_{\mathrm{R}}$ with respect to the intersection point of the two traps.

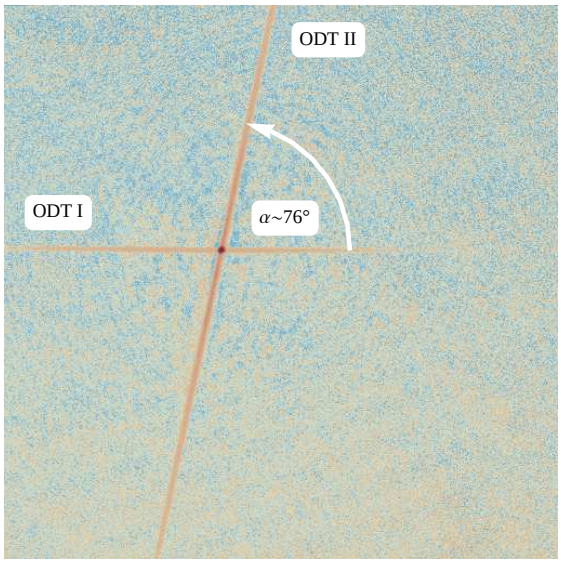

Figure 3.14: Absorption image of the crossed traps in our experiment. The two traps intersect at an angle of $\alpha \sim 76°$. The focus of the trap propagating from the left to the right in the image is displaced by $\sim 2z_R = 5\mathrm{mm}$.

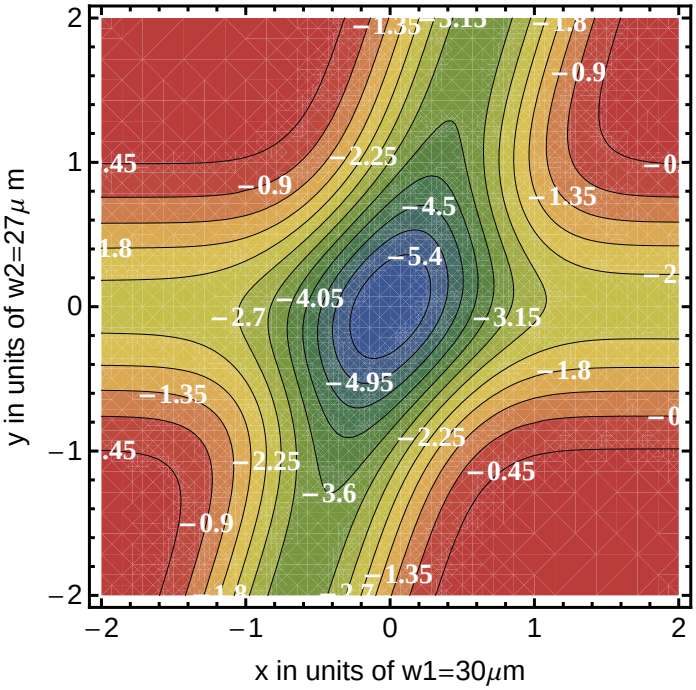

Figure 3.15: Equipotential lines in the $x-y|_{z=0}$ plane at z=0 of a crossed trap under an angle of 76°. The equipotential lines are in units of $E/k_{\mathrm{B}} = T(\mu K)$. The trapping region in x and y direction is just a few ten μm across and the focus of the trap propagating in x direction is $0.2 z_{\mathrm{R}} \sim$ 0.5mm away.

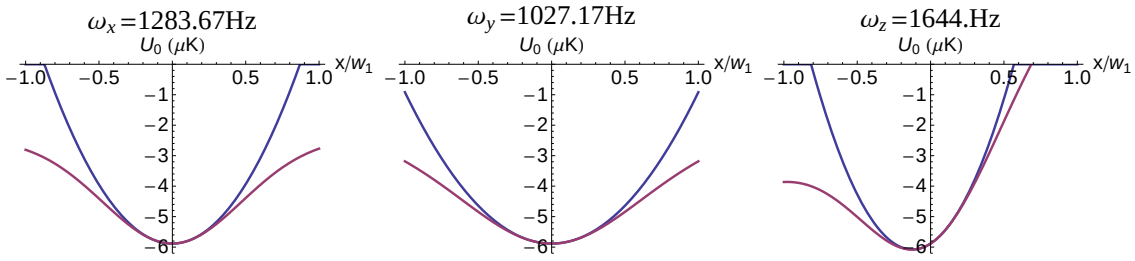

(a) x-direction (b) y-direction (c) z-direction

Figure 3.16: The trapping frequencies along the directions of the Cartesian system. In each plot the blue line shows the actual potential whereas the purple one the potential found by the harmonic approximation. Labels are the trap frequencies in each direction.

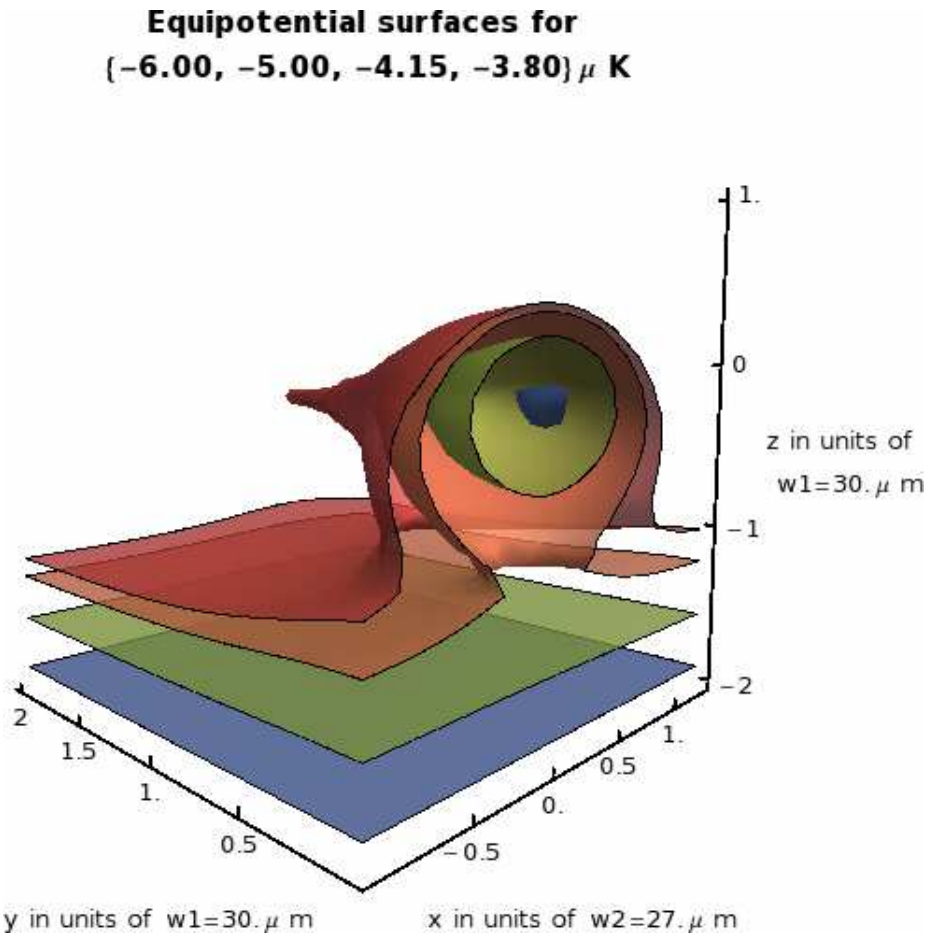

Figure 3.17: Equipotential surfaces for $-6, -5, -4.15, 3.8\mu$K

is visualised in figure 3.16. The geometry of the potential can be shown for a surface of constant energy (see figure 3.17) and we see that above a certain energy the trap "opens up" and atoms can leak out of the trap. In figure 3.18 slices through the centre of the trap are shown for a line of constant energy. The challenge therefore is to have a trap that is deep enough to still trap atoms versus gravity but not to have to evaporate further e.g. lowering the intensity further to achieve quantum degeneracy.

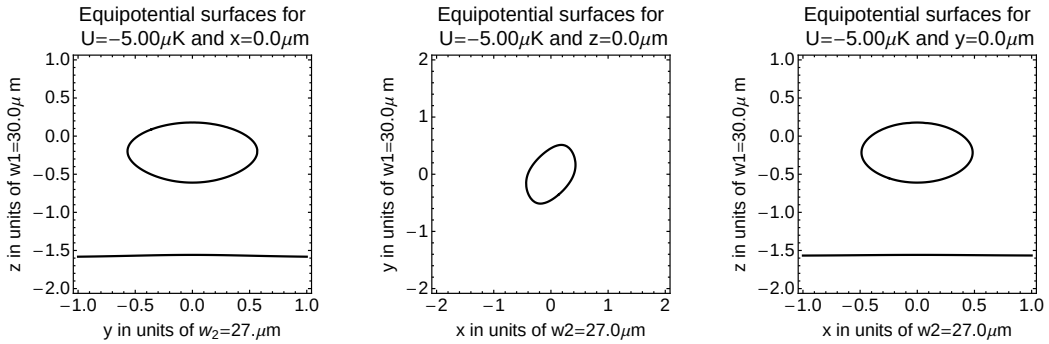

Figure 3.18: Similar to figure 3.17 the cross sections through the trap in the planes y-z,x-y and x-z from left to right.

4 Experimental set up

In this chapter we have a look at all the different components that are used in this experiment to achieve Bose-Einstein condensation in an all-optical trap. The general idea to reach quantum degeneracy is to load a magneto-optical trap (MOT) using near resonant light, transfer the atoms into a optical dipole trap (ODT) of a far resonant laser and evaporatively cool the atoms by lowering the power. BECs formed in a ODT are called 'all-optical' BECs as the trapping potential is provided by the laser field only. The onset of Bose-Einstein condensation is typically observed at temperatures on the order of a few hundred nano-Kelvin. In our experiment we use the absorption imaging technique for detection and further analysis.

4.1 Ultra high vacuum system

Three counter propagating pairs of laser beams are needed for a MOT. Preferably the optical access for the dipole trap, ring trap and imaging is not used along one of the MOT beams as well. To keep the current as low as possible and to reduce the inductance the coils should be as small and as close to the atomic sample as possible. Furthermore, the inner surface of the set up should be as small as possible to reach and maintain an ultra high vacuum. These constraints are satisfied using a commercial vacuum chamber from Kimball Physics. It has eight equidistant $2\frac{3}{4}''$ ports on a ring and two $6''$ ports on the faces of the ring as can be seen in figure 4.1. The design of the set up was developed in SolidWorks,(see figure 4.1). A pressure gauge is mounted on the far left mainly to monitor the pressure for detection of coarse leaks, during

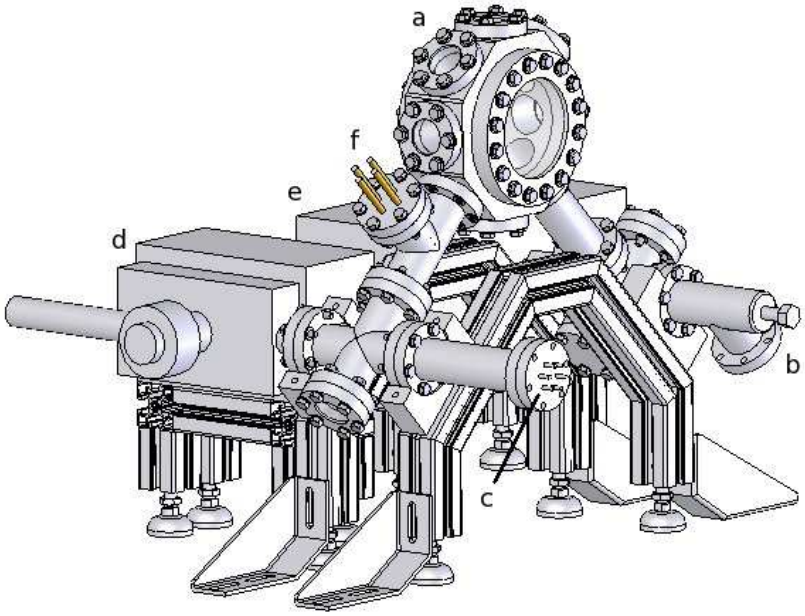

Figure 4.1: The vacuum part of the experiment (a) chamber, (b) valve, (c) pressure gauge, (d) and (e) Varian ion pumps, (f) feedthrough connecting the dispenser.

.

Figure 4.2: During the bake out the pressure in the chamber was continuously monitored on a pressure gauge. Turning on and off the ion getter pumps during that time caused some pollution as is clear from the spikes in the pressure.

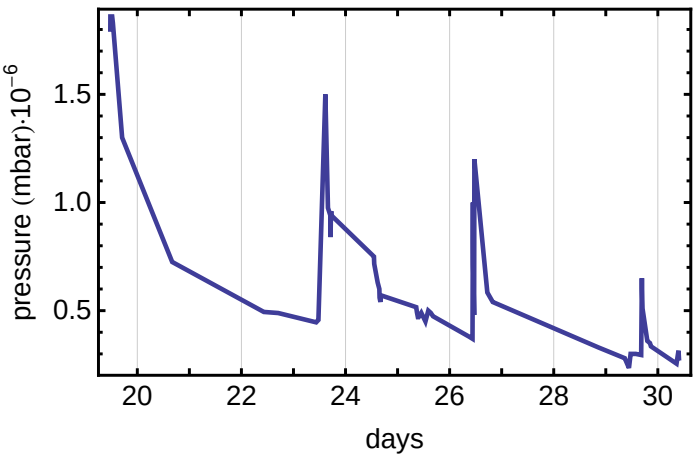

the baking. Two ion pumps (Varian) are mounted on the right to keep the pressure in the low range of 10^{-10}mbar. This pressure is required to keep the scattering rate with the remaining background gas low for trapped atoms. In order to achieve a clean ultra high vacuum the set up was baked out over 4 weeks at a temperature of 150°C. The set up was wrapped with Aluminium foil and heated up with flexible band heaters. The temperature was measured at various points of the set up and slowly increased in order to avoid thermal stress on components. The valve was left open and connected to a turbo pump to pump away atmospheric gases and to reach low pressures. During that time the remaining background gas was analysed with a mass spectrometer. The valve was closed when the fraction of hydrogen of the remaining background gas was dominant. After slowly decreasing the temperature the pressure gauge was reading pressures as low as 10^{-10} mbar, at the limit of its sensitivity. The pressure during the bake out is shown in figure 4.2. In order to remove contaminants from the ion pumps we turned the ion pumps on for brief times. These short bursts of contaminants being emitted into the chamber can be clearly seen in figure 4.2 by the sharp rises of the pressure. With each repeat the amount of contaminants being emitted became smaller as we see from the decaying height of the pressure burst in figure 4.2 each time the ion pumps where turned on for a short time.

4.2 Experiment control

One of the technical challenges for experiments in atom-optics is the accurate timing and control of the experiment on long and short time scales. At the beginning of each run of an experiment it takes typically several seconds to load a MOT and to form a BEC. On the other hand actual experiments and the final imaging only take ms or even μs. We use digital channels to switch shutters, to turn on and off AOMs and to trigger a camera. Analog channels are used to adjust frequencies of VCOs and to control power levels.Typically experiments in atom optics follow a step by

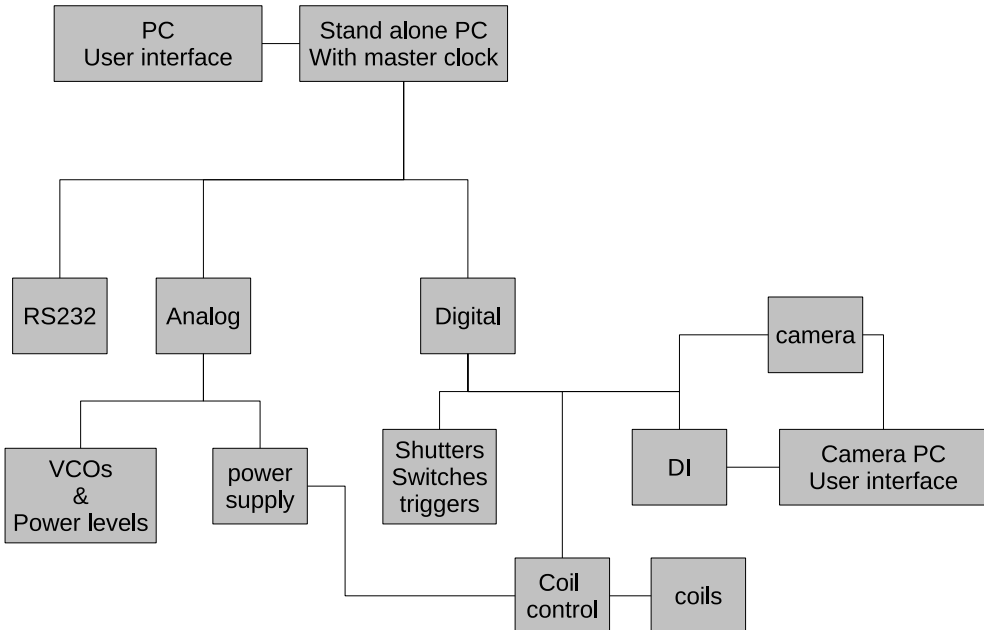

Figure 4.3: Schematic flow chart of the experiment control. Details are described in the text.

step routine of different time scales in each step and various parameters changing from step to step. A user friendly interface to control an experiment was developed by Aviv Keshet at the MIT in W. Ketterle's group. The software contains Cicero Word Generator (see figure 4.4) and Atticus Hardware Server. It gives the user the ability to control sequences of 60s duration with a time resolution of 1-2μs. This software runs on a PC and is connected to a stand-alone PC with a master clock in order to synchronise the analogue and digital channels. The stand alone unit delivers digital inputs and analogue levels to National Instruments (NI) instrument cards and RS232 commands via two serial channels. A schematic overview of the experiment control system is given in figure 4.2. The analogue channels are used to adjust the frequencies for the AOMs for the laser frequency control, MOT detuning and imaging (see section 4.3 for further details) and to control the power levels of the repumper and the power level of the laser beam for the optical dipole trap (see section 4.5 for further details). The digital channels are used to trigger shutters to extinguish light in several beam paths, to trigger switches in order to turn on or off AOMs (see section 4.3) and to select different configurations of magnetic fields. The options of different configurations of magnetic fields are discussed in more detail in section 4.4.1. The details for the control of the imaging are described in section 4.6

4.3 Laser system-MOT

The continuous absorption and spontaneous emission of photons driving the $|2, X\rangle \rightarrow |3, X\rangle$ transition cools the ^{87}Rb atoms (see figure 4.5). However, some atoms decay into the F=1 state and would be lost if they are not transferred back into the cooling transition. Therefore the repumper excites the atoms into the $F' = 2$ state from where they either decay back into the $F = 1$ state or into the $F = 2$, where they get back into the cooling transition. Figure 4.6 is a simple schematic of the laser system for the MOT and detection systems. It consists of two commercial diode lasers (Toptica, TA

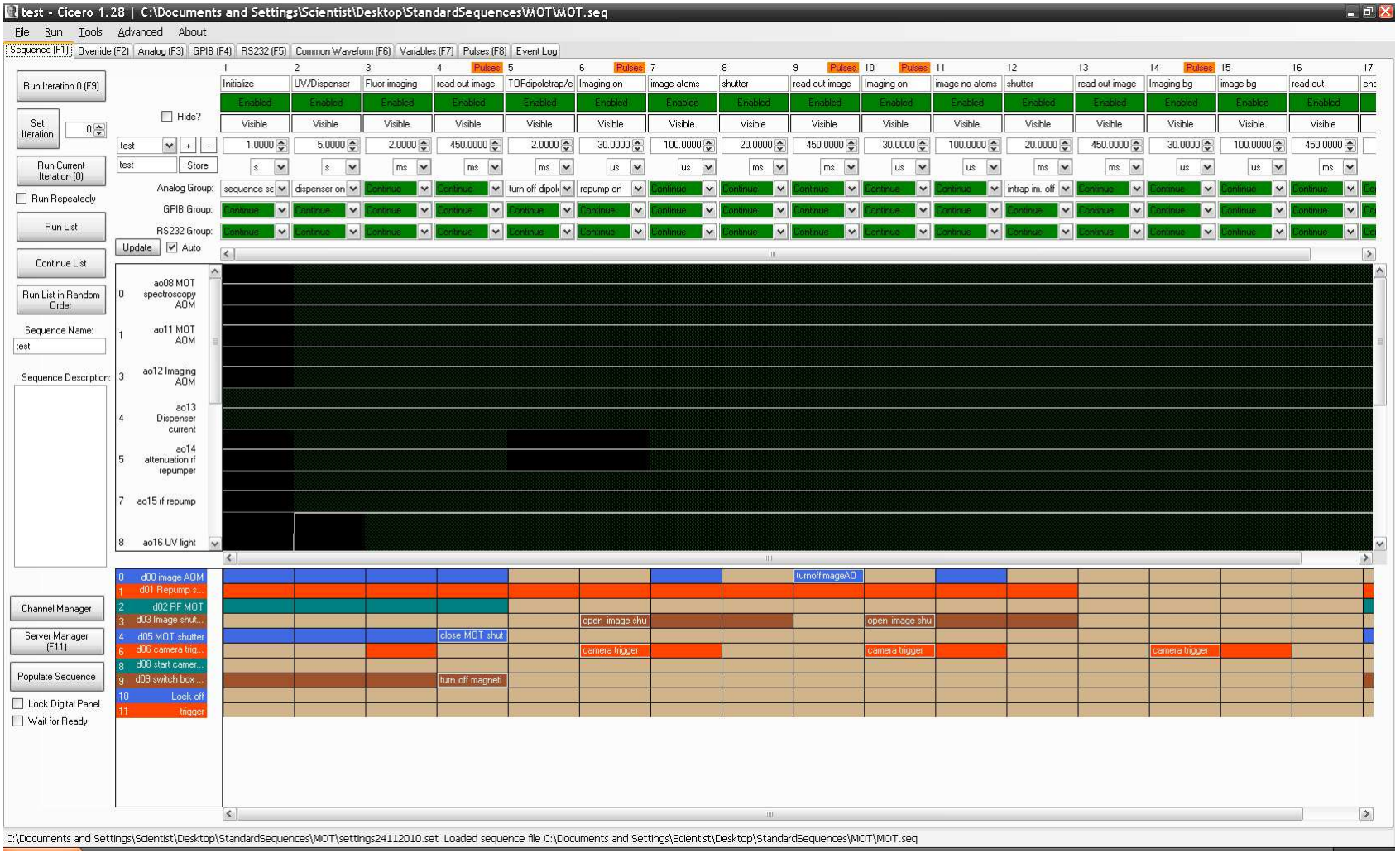

Figure 4.4: Screenshot of the Cicero word manager being used for the sequence control. The Cicero word manager shows an overview of the values of the analog and digital channels during a timeslot

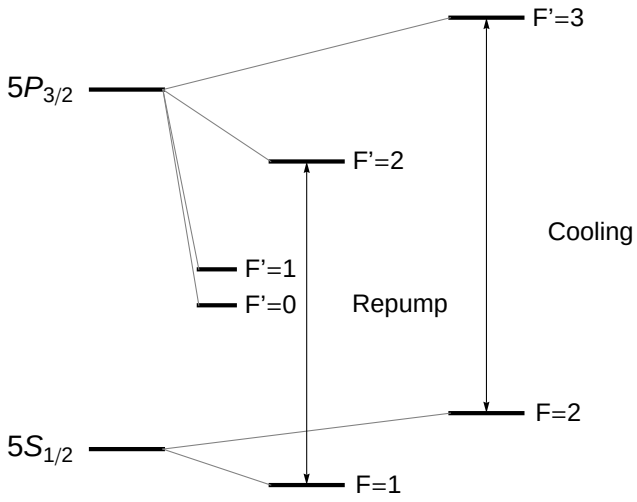

Figure 4.5: The relevant transitions for the cooling of ^{87}Rb in a MOT.

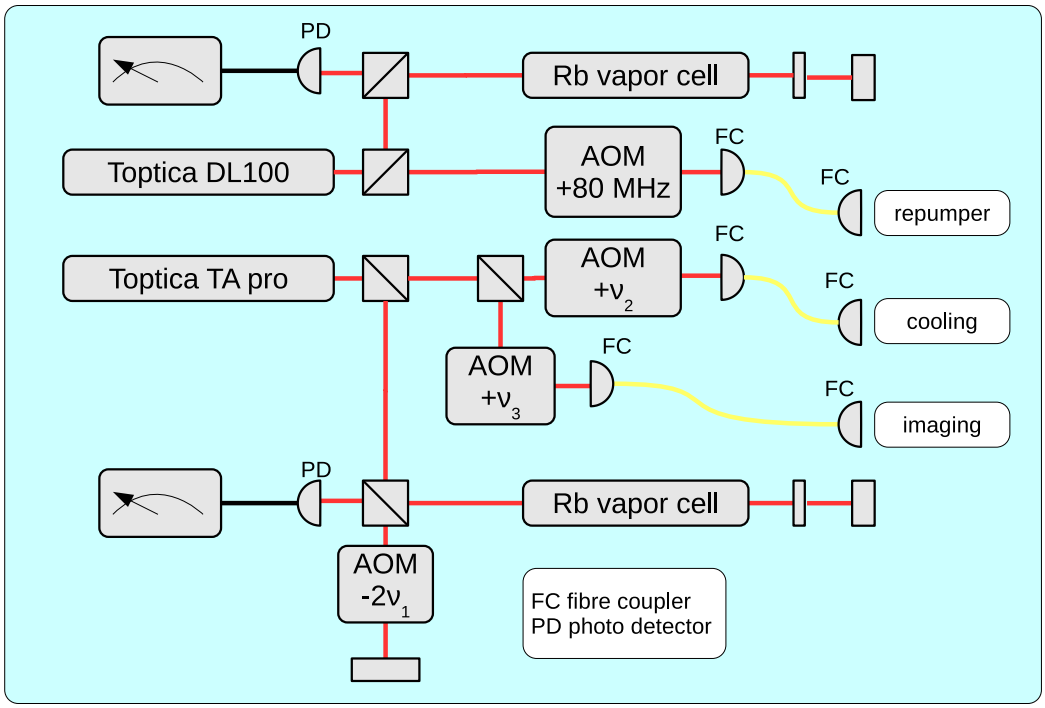

Figure 4.6: A simple schematic of the MOT and detection laser system.

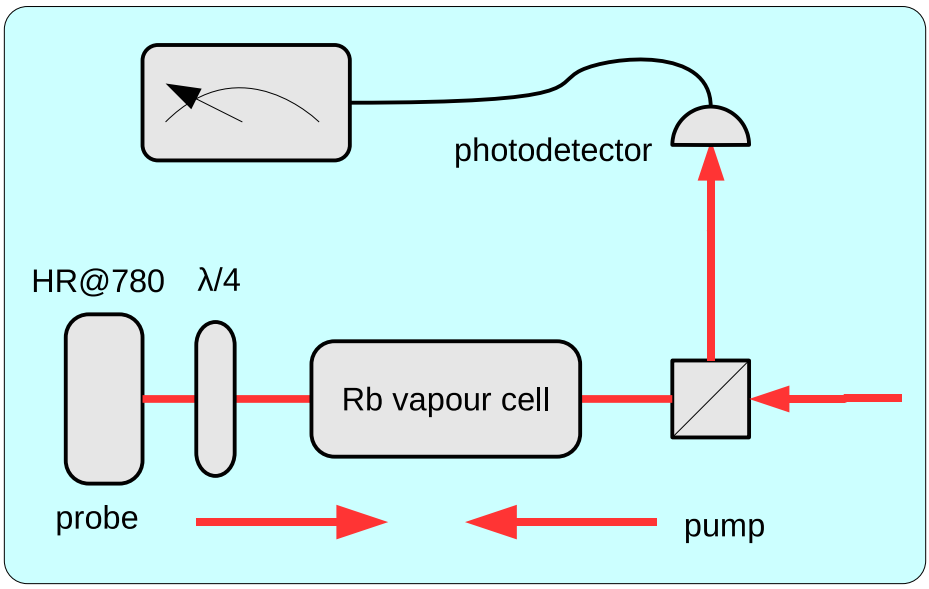

Figure 4.7: In the simplified sketch of a pump and probe set up, a linearly polarised beam passes through a polarising beam splitter and through a glass cell that contains a dilute gas of Rubidium. The $\lambda/4$ wave plate rotates the polarisation of the reflected probe beam such that the polarisation of the pump and probe are orthogonal. The absorption is monitored on a photo detector.

Pro and DL100) to drive the cycling transition for cooling and repumping ^{87}Rb shown in figure 4.5. The $F = 1$ and $F = 2$ states are separated by 6.8 GHz (see figure 4.11) so it is from a technical point of view easier to set up another Doppler-free saturated absorption spectroscopy unit instead of using a frequency offset lock which requires an accurate frequency source. A probe beam of each laser, (seefigure 4.6) is used to stabilise the frequency using standard Doppler-free saturation spectroscopy. Doppler-free saturation spectroscopy is a technique to selectively detect atomic transitions of those atoms which belong to the class of velocity $v = 0$ parallel to the propagating beam. To detect the atomic transitions we excite the atomic sample with a pump beam and monitor the transmittance with a probe beam on a photodetector (see figure 4.7). Let us assume our pump beam has a frequency ω_L which is slightly lower than an atomic transition ω_0. The condition to absorb resonant photons is $\omega_L = \omega_0 - kv$

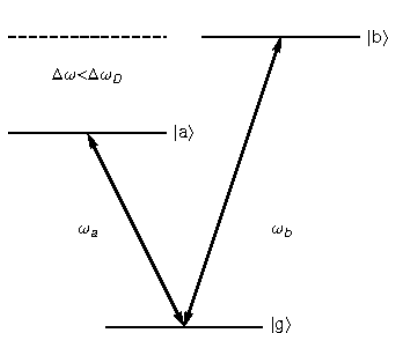

Figure 4.8: The upper states $|a\rangle$ and $|b\rangle$ with common ground state $|g\rangle$. The splitting $\Delta\omega$ of the two upper states is smaller than the Doppler-width ω_{D}

and depends on the direction of the propagation of the beam and the motion of the atom. Therefore only atoms with a velocity $-v$ absorb photons from this beam and a reflected beam will only be absorbed by atoms of velocity $+v$. For $\omega_L = \omega_0$ only atoms of velocity $v = 0$ absorb photons and the absorption of the probe beam is lower. Yet, in a multi-level system we see the effect of cross over resonances, if two (or more) levels are separated by a frequency smaller than the Doppler-width (see figure 4.8). Consider the frequency $\omega = \frac{\omega_a+\omega_b}{2}$ where the pump beam excites atoms of velocity $-v$ into the state $|a\rangle$ and the probe beam excites atoms at velocity $+v$ into the state $|b\rangle$. We then have $\omega_a - kv = \omega_b + kv$ or $kv = -\frac{\omega_b+\omega_a}{2}$. The probe beam depletes the population of the common ground state and the sample becomes more transparent for the probe beam. Of course the signals from cross-over resonances increase the number of observed lines in a spectrum but they are actually very useful for controlling and adjusting frequencies for various applications in our experiment. The states $F' = 2$ and $F' = 3$ of ^{87}Rb are separated by 266.7 MHz with the common ground state $F = 2$ and therefore we see a cross-over resonance 110 MHz below the transition from $F = 2 \rightarrow F' = 3$.

In order to tune the frequency of the light for the MOT independently of other applications and alignment we use an AOM in a double-pass configuration (see figure 4.10). The advantage of a double-pass configuration is that the retro reflected beam, which is shifted twice in its frequency, is collinear with the incident beam. If one wishes to tune the frequency of that laser during an experiment, no further alignment

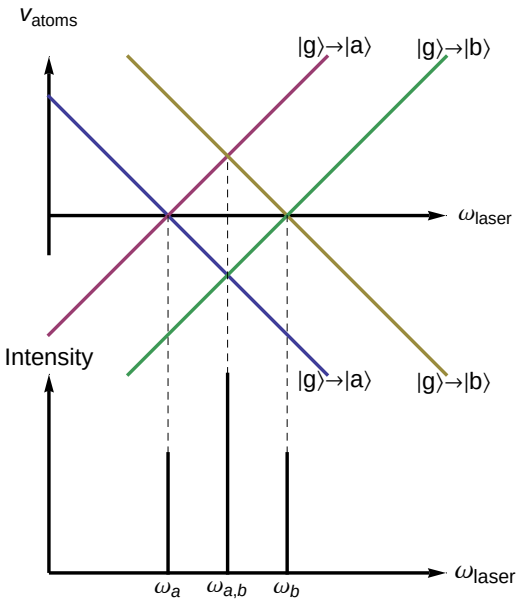

Figure 4.9: Occurrence of crossover resonances in a system of one ground state $|g\rangle$ and two excited states $|a\rangle$ and $|b\rangle$. Lines of positive slope belong to the pump beam and lines of a negative slope belong to the probe beam. A signal occurs where pump and probe beam intersect. The crossover resonance occurs if pump and probe excite different states.

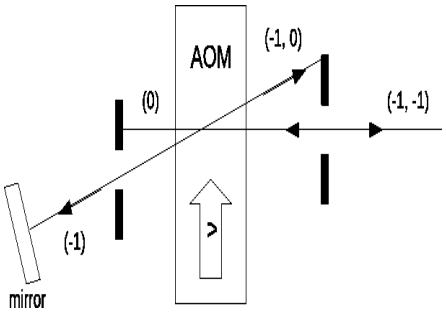

Figure 4.10: Tuning of the frequency using using a double pass configuration. An incident beam is deflected by an AOM and shifted in its frequency by an amount of ν. The deflected part of the back reflected beam is shifted twice in its frequency. In brackets are the orders of deflection (1st, 2nd).

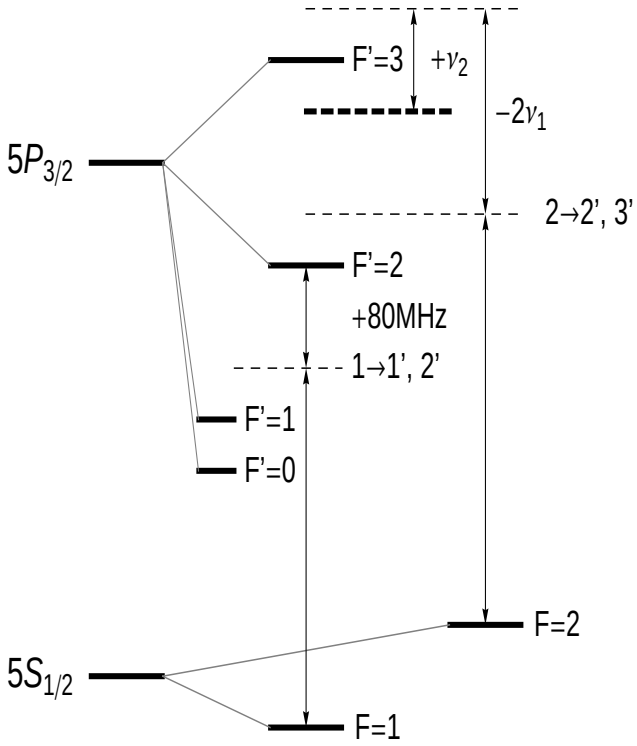

Figure 4.11: The cooling laser is locked to the $F = 2 \rightarrow F' = 2, 3$ cross over resonance and is blue detuned with respect to the $F = 2 \rightarrow F' = 3$ with a double pass AOM configuration. With another AOM the frequency of the light is red detuned by a few MHz below the $F = 2 \rightarrow F' = 3$ transition.

is required. In our experiment we shift the frequency twice with the negative first order such that the total frequency shift is $2\nu_{\mathrm{AOM1}}$. The frequency to run the MOT is adjusted with another AOM at frequency ν_{AOM2} such the total detuning of the MOT laser beam becomes $\Delta\nu = \nu_{\mathrm{AOM2}} - 2\ \nu_{\mathrm{AOM1}}$. The frequency of one laser (TA pro) is blue detuned with respect to the $|2, X\rangle \rightarrow |3, X\rangle$ transition of ^{87}Rb (see figure 4.12(a)) and is adjusted with AOMs to the desired frequency for cooling and detection of ^{87}Rb. Another laser (DL 1100 is locked to the $F = 1 \rightarrow F' = 1, 2$ crossover resonance (see figure 4.12(b)) and shifted on to resonance of the $|1, X\rangle \rightarrow |2, X\rangle$ repumping transition with an AOM. Figure 4.11 shows the locking as described above.

4.4 Coil design

Magnetic fields are an important tool to manipulate atoms and require accurate control. A magnetic quadrupole field is required for loading the MOT, weak homogeneous

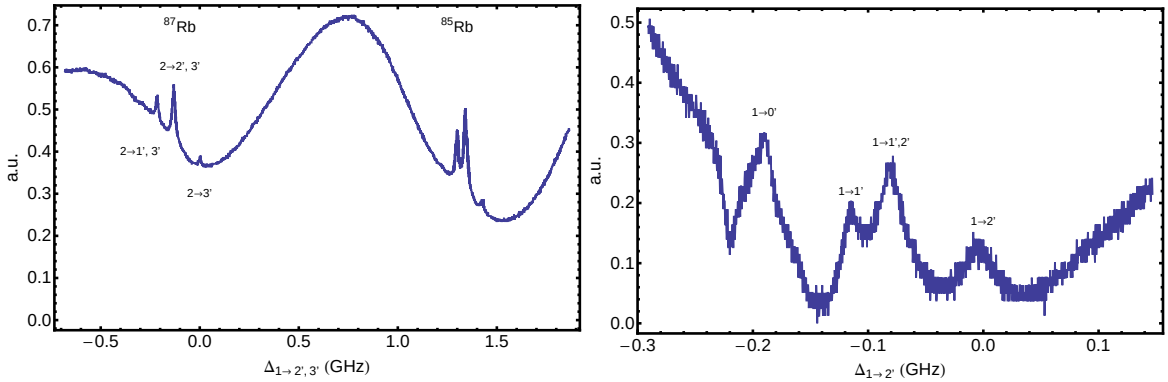

(a) The left feature shows cross over resonances of transitions of ^{87}Rb from $F = 2 \rightarrow F' = 2, 3$. The weakest peak is the $F = 2 \rightarrow F' = 3$ transition. The strongest peak is given by the crossover resonance from $F = 2 \rightarrow F' = 2, 3$.

(b) Crossover resonances of transitions from $F = 1 \rightarrow F' = 0, 1, 2$ To lock a laser the cross over resonance $F = 1 \rightarrow F' = 1, 2$ is used and with an AOM the frequency is adjusted to the $F = 1 \rightarrow F' = 2$ transition. transition.

Figure 4.12: For cooling and trapping ^{87}Rb in a MOT the transition from $F = 2 \rightarrow F' = 3$ is used for cooling, whereas the transition $F = 1 \rightarrow F' = 2$ is used to pump the atoms back into the cooling cycle. The transitions and locking points are shown in figure 4.11. Absorption spectra of the cooling and repump transition are shown in figure 4.12(a) and 4.12(b)

fields are needed to supply a quantisation axis and high homogeneous fields are required to tune atom interactions with Feshbach resonances. The former is simply realised with any pair of coils with currents flowing in opposite directions, whereas for the latter the best realisation is given for two coils separated by a distance equal to their radius, also known as the Helmholtz condition. Both kinds of fields can be supplied by the same pair of coils. The constraints are: 1. size of the windows of the chamber (R=8 cm), 2. diameter of the wire (ø=3.25 mm), 3. desired maximum field strength (B=1200 G at (160 A,40 V)), 4. homogeneity of the field in the center ($\frac{\Delta B}{\Delta z} = \min$). In cylindrical coordinates the axial and transverse field components for a single current loop of radius R perpendicular to the z axis and placed at z=A are given by:

$$\begin{aligned} \mathrm{B_z} &= \frac{I\mu_0}{2\pi\sqrt{(r+\mathrm{R})^2+(z-\mathrm{A})^2}} \\ &\times \left(\frac{(-r^2+\mathrm{R}^2-(z-\mathrm{A})^2)\,E(k)}{(\mathrm{R}-r)^2+(z-\mathrm{A})^2}+K(k)\right) \end{aligned} \tag{4.1a}$$

$$\begin{aligned} \mathrm{B_r} &= \frac{\mu_0 I(z-\mathrm{A})}{2\pi r\sqrt{(r+\mathrm{R})^2+(z-\mathrm{A})^2}} \\ &\times \left(\frac{(r^2+\mathrm{R}^2+(z-\mathrm{A})^2)\,E(k)}{(\mathrm{R}-r)^2+(z-\mathrm{A})^2}-K(k)\right) \end{aligned} \tag{4.1b}$$

with

$$\mathrm{k} = \frac{4r\mathrm{R}}{(r+\mathrm{R})^2+(z-\mathrm{A})^2}, \tag{4.1c}$$

where E(k) and K(k) denote the complete elliptical integrals [69]. With these parameters it was found from calculations (using Mathematica) that coils with 12 layers of 7 turns at a distance of 8.8 cm, in contrast to 8 cm given by the Helmholtz condition, comply best with the requirements mentioned above. Strictly the Helmholtz condition applies to a set of two coils of zero wire radius. Here we took the finite size of the wire into account and the winding of the coils which explains the discrepancy of distance of the two coils comparing the ideal and the real arrangement of the coils. The linearity of the quadrupole field as a function of the current and spatial position, and

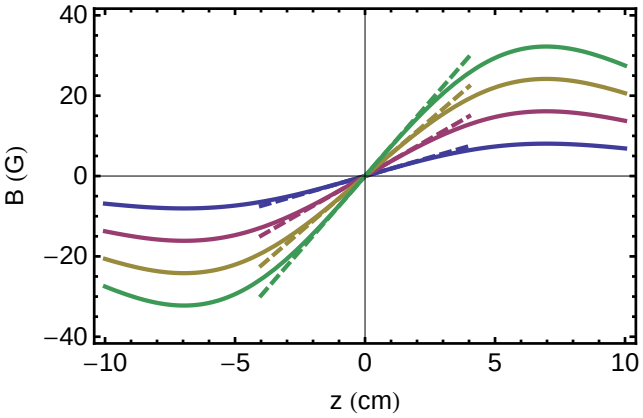

Figure 4.13: The lines show calculations (see equations 4.1) of the strength of total magnetic field in the anti-Helmholtz configuration between the coils for $I = 2, 4, 6, 8$A. Between the coils the field changes linearly as shown with the dashed lines.

	calculated	measured
resistance [Ω]	0.24	0.26
inductance [mH]	1.748	1.72±0.03
gradient [G/cm] (for I=8A)	7.44	7.64±0.02
magnetic flux at centre [G](for I=8A)	55.95	55.75±0.1

Table 4.1: Summary of calculated and measured characteristics of the Helmholtz pair. All magnetic fields were measured with a GM04 Gaussmeter.

also the homogeneity of the field are depicted in figure 4.14, taken with a Hall-probe (Hirst Magnetic Instruments (GM04)). The accuracy of the probe is better than 1% at 20°C, and the results show a good agreement with the calculations tabulated in table 4.1. The Helmholtz field varies less than one percent over a range of 2.5cm along the field direction. The size of the BEC can be expected to be about 100 μm. Over this region the spatial variation of the magentic field vaires by a few parts per million for a constant current. This is sufficient to manipulate the interaction close to Feshbach resonances which typically are a few mG wide.

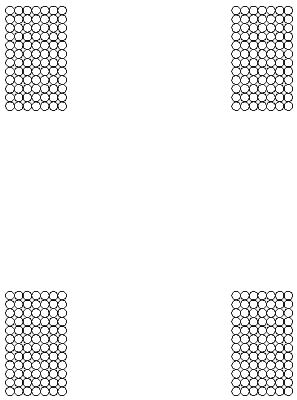

(a) Each coils is made of 7*12 windings of a copper wire of a diameter of 3.25mm.

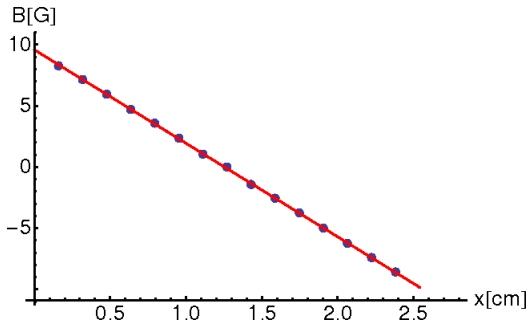

(b) Magnetic flux B as a function of position (dots) at a constant current of I=8A. The slope of the linear fit is 7.64 ± 0.02G/cm.

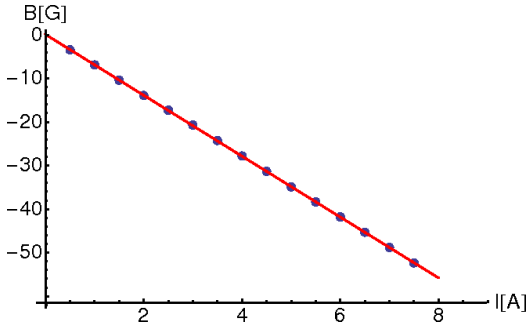

(c) Currents flowing through both coils in the same direction results in a homogeneous magnetic field. The strength of the field changes linearly with the strength of the current. Magnetic flux B (dots) as a function of current I at the center of the field, $B = B(I)|_{x=0}$. The line shows a linear fit.

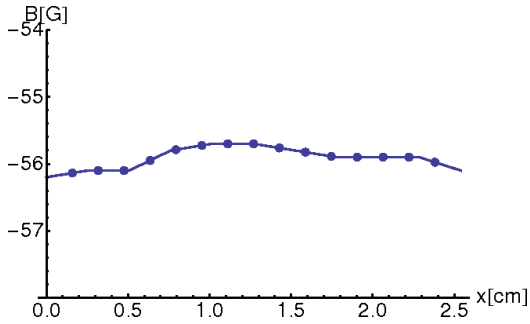

(d) Homogeneity of the Helmholtz field at the center, $B = B(x)|_{I=\text{const}}$.

Figure 4.14: Production of the magnetic field and its calibration. The current flows through the coils 4.14(a) in anti-Helmholtz 4.14(c) or in Helmholtz 4.14(b) and 4.14(d) configuration and forms an inhomogeneous or a homogeneous magnetic field.

	TTL 1	TTL 2	TTL 3	configuration
I.	0	0	0	OFF
II.	1	0	0	Helmholtz
III.	0	1	0	Anti-Helmholtz
IV.	0	0	1	+Coil 2
V.	1	1	0	+ Coil 1
VI.	1	0	1	- Coil 2
VII.	0	1	1	n/a
VIII.	1	1	1	n/a

Table 4.2: The eight combinations of the three TTL inputs set the desired configuration. Configuration I. is needed to load the MOT and configuration II. to apply a weak homogeneous magnetic field to provide a quantisation axis. The configurations IV., V. and VI. are useful to supply an inhomogeneous magnetic field in order to spatially separate spin mixtures.

4.4.1 Coil control

For experiments with BECs, magnetic fields of different strengths and directions are required, and to apply homogeneous and inhomogeneous fields one has to be able to control the direction of the current in the coils. The technical challenge of such a device is to be able to switch high currents as quickly as possible. Different configurations are chosen by turning on and off MOSFETS (see figure 4.15) to conduct the current along different paths. These configurations are turned on and off via TTL signals from the computer. Three inputs set different settings and the truth table 4.2 shows the available configurations. The response of switching on and off the coils in anti-Helmholtz configuration is shown in figure 4.16 for different currents. While switching the anti-Helmholtz configuration on, the second input of the current switcher is set high. The decay of the current is determined by the inductance of the

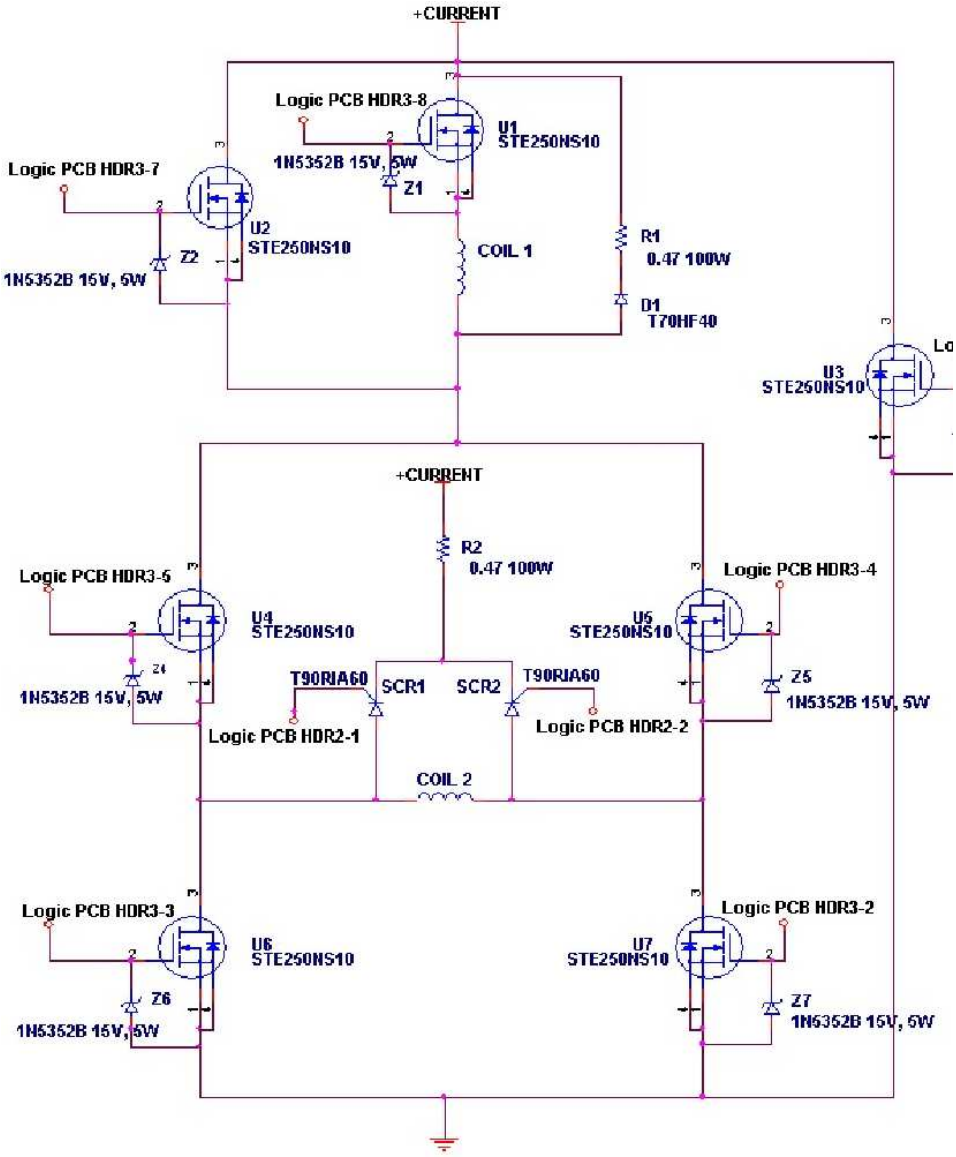

Figure 4.15: Circuit diagram of the current switcher.

Helmholtz mode: the gates of U1, U6, U7 are on to allow the current to flow in the same direction through the coils 1 and coil 2.

Anti-Helmholtz mode: the gates of U1, U5, U6 are switched on to allow the current to flow through coil 1 and in opposite direction through coil 2.

Single coil modes: the current is flowing only through coil 1 if U1 is switched on and the current is bypassed through U5 and U7 or U4 and U6. A change of direction through coil 1 is not possible. A combination of U2, U5, and U6 will allow the current to flow in one direction or in another if U2,U4, and U7 are switched on through coil 2.

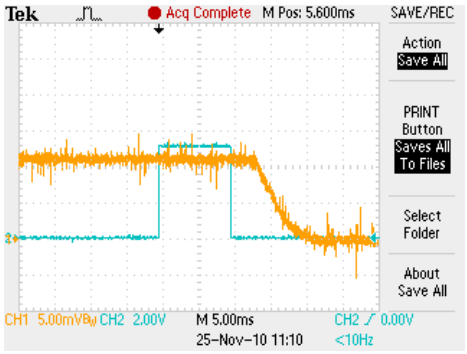

(a) Switching off the coils at current of 11A

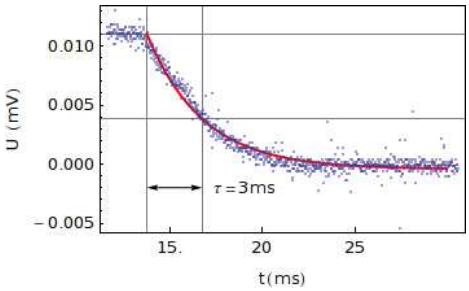

(b) Exponential fit to deacy of the current from 11A

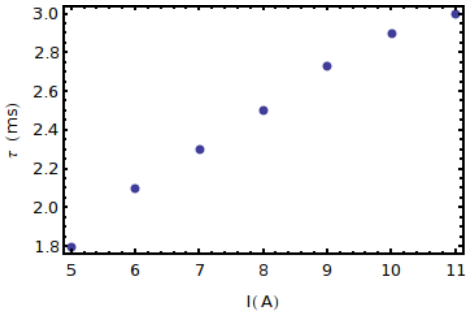

(c) Time constants of the decay for different initial currents

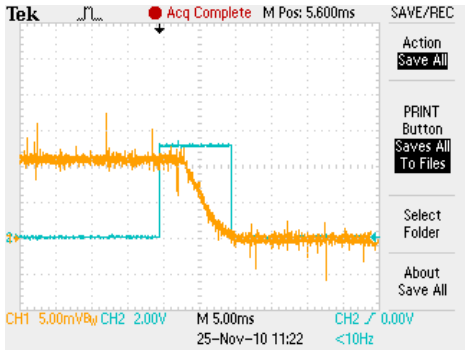

(d) Switching off the coils at current of 11A with a 10ms pretrigger

Figure 4.16: The decay time (1/e) of the current is 3ms for a current of 11A and decreases for lower currents. Setting a pretrigger in the sequence turns the current of earlier to ensure that the current is off at the end of the desired time slot.

coils and the voltage drop across the MOSFETs. The time constant of the decay of a initial current is 3ms, which is too long. In order to cool the atoms below the Doppler limit during an optical molasses no residual fields should be present. This also limits the feasibility of a compressed MOT where in order to increase the density of the atoms the magnetic gradient is increased in a short time on the order of 10ms before the current is turned off for the molasses cooling. It turned out that the current supply we used first was not able to ramp currents up or down in a sufficiently short time. We overcame this problem with another power supply from Delta Elektra the

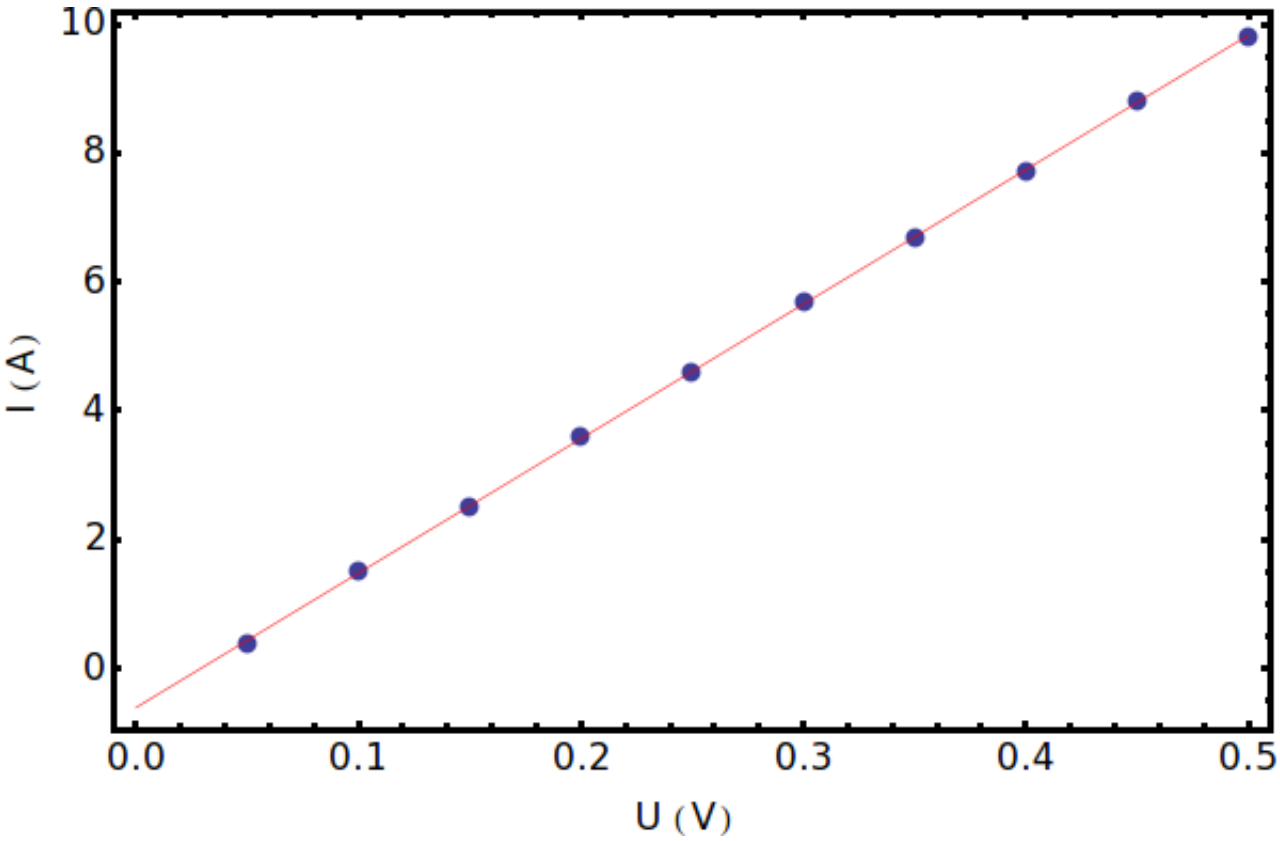

Figure 4.17: Calibration of the output current as a function of the supplied voltage of the analogue channel. The dots show the data points and the line a linear fit. The function of the fit is I(U)=20.86A/V·U-0.6A

output, of which can be remotely controlled via analogue channels (see figure 4.17). Leaving the switch constantly in the Anti-Helmholtz mode shortens the switching time. Still the problems remained that the time for the current to decay was too long.

4.4.2 A faster switch for the current

In order to achieve a faster decay of the current we replaced the previous circuit with a circuit of four parallel insulated gate bipolar transistors (IGBTs) which are clamped by Zener diodes to a voltage of 390V. The decay of the current from 10A to 0A was

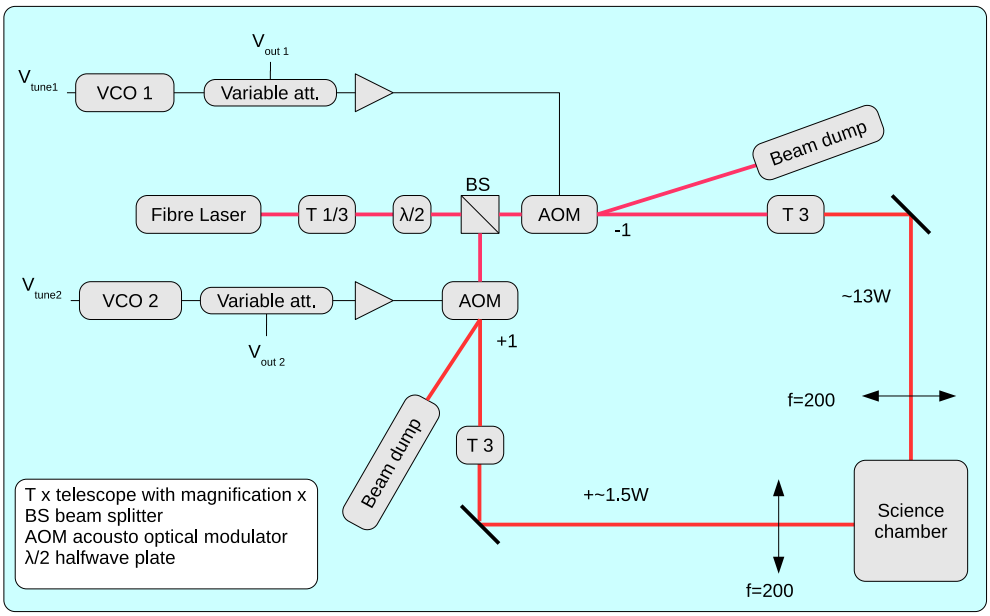

Figure 4.18: Schematic of the power control of the laser for the optical dipole trap.

faster than 50μs, measured by induced current within a current clamp () which is not permanently in the set up and therefore has no effect on the experiment.

4.5 Laser system-optical dipole trap

For the optical dipole trap an infra red fiber laser from IPG (YLM-29) is used, operating at a wavelength of $\lambda_L = 1064$nm. The output of the laser is linearly polarised and has a maximum power of 20W. The loading dynamics of our ODT will be discussed in chapter 6 and here we only want to describe how we control the power in the laser beams of a crossed trap. Figure 4.18 shows a schematic diagram of the setup for the optical dipole trap. The beam exiting from the head of the fibre laser passes first through a combination of a telescope (magnification=1/3) a half-wave plate (HWP) and a polarising beam splitter to adjust the power in two paths and to match the aperture of the AOMs for optimal operation. After deflection by the AOMs both beams pass through another telescope (magnification=3) to size each beam to its original

diameter (D=5mm) before they are focused via a lens of focal length f=200mm into to the science chamber. We can estimate the waist of a focused Gaussian laser beam at the focus using the equation $w_0 = (2\lambda/\pi)(f/D)$. Therefore we expect a waist of $w_0 \sim 27.1\mu$m. In order to avoid perturbing interferences between the two that cause heating of the atoms the polarisations are adjusted to be orthogonal and the frequency shift between both beams is about 160MHz. The amount of light being deflected by the AOMs is determined by the power of the RF-frequency driving the AOM. In order to have an accurate control over the power we use a feed back loop (see figure 4.19) which monitors the power level of each path on a photodetector. The challenging task is to gain a reliable control over three orders of magnitude in power. Typical powers to load our ODT are $9-13$W but will be as low as few tens mW by the end of the evaporation. After the beams passed through the chamber we only pick a few percent of the intensity with a thin glass plate and reflect it onto a photodetector which allows us to control the power over three orders of magnitude. This is achieved with noise eater for feedback control. Essentially it is a differential amplifier that adjusts the output signal such that the difference between the two input lines is zero.

4.5.1 Calibration of the ODT

The need of a noise eater also comes from the fact that although the intensity of the laser is sufficiently stable after its warm up time (see figure 4.20) of roughly 30min it has a long term fluctuation on the order of $\pm$100mW which is too much to run the evaporation reliably.

The power in a deflected order is a convoluted function of the response of the attenuation of the voltage variable attenuator and the AOM itself (see figure 4.18) which both are strongly non-linear. Figure 4.21(b) shows the voltage V_{PD} on the photodetector versus the control voltage V_{c} from the computer. If we turn on the feedback the noise eater will stabilise the voltage of the photodetector given to a reference.

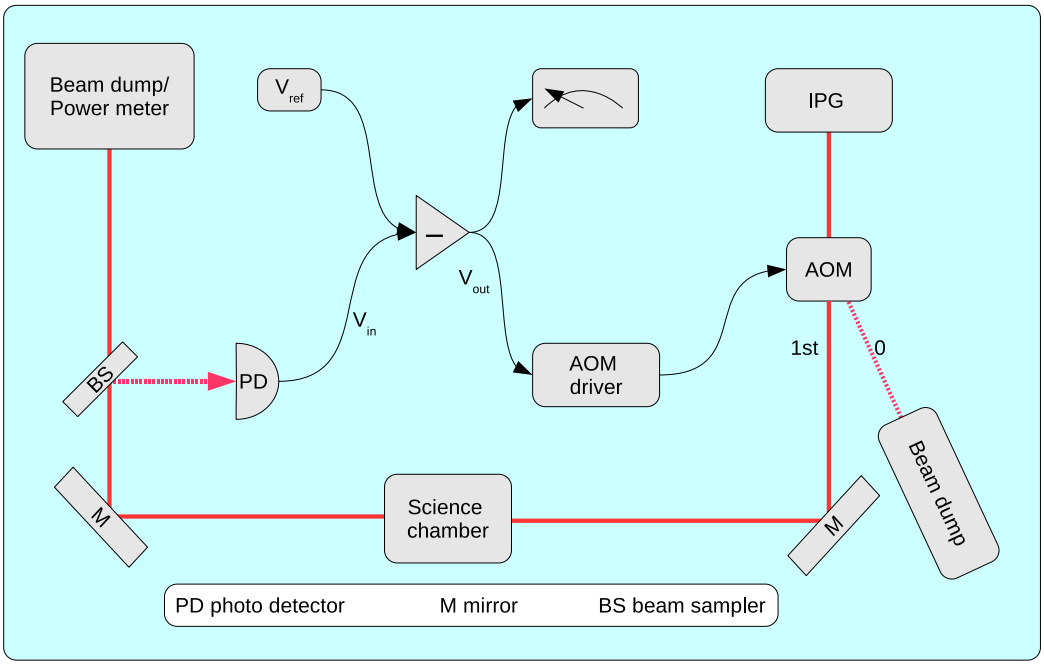

Figure 4.19: Simplified schematic of the feedback loop to control the power in the deflected order.

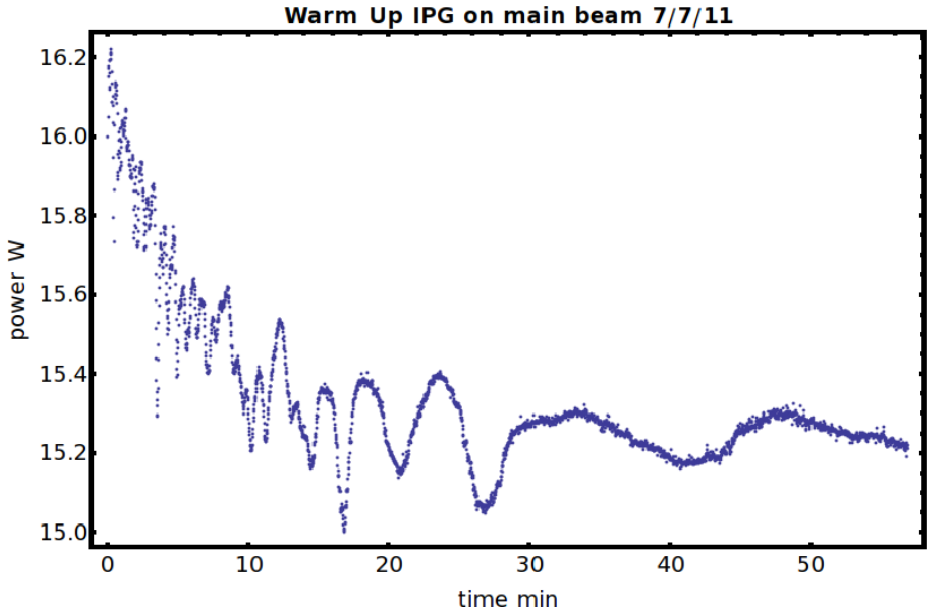

Figure 4.20: After turning on the emission of the fiber laser it takes about 30min to emit light on a stable level. After warming up the fluctuation of the power is less than 1%.

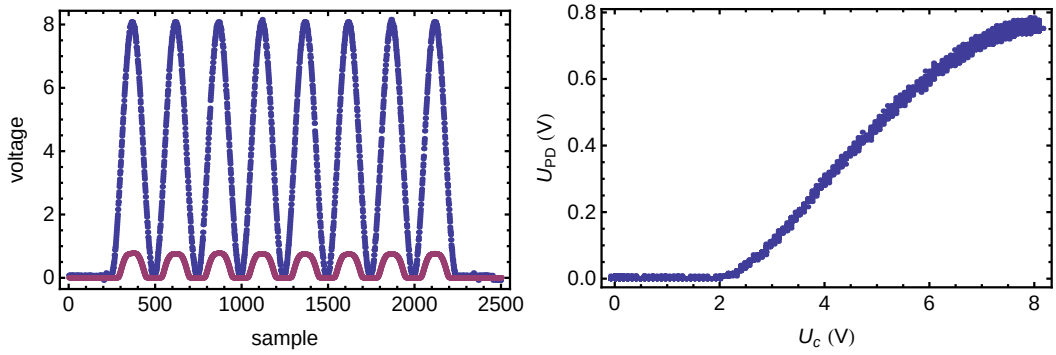

(a) The blue line shows the measured output voltage with a slow modulation. The purple line shows the measured voltage on the photodetector which was attenuated by a factor 10.

(b) The response of the AOM as a function of the control voltage V_c is visualised by plotting the voltage of the photodetector against the control voltage

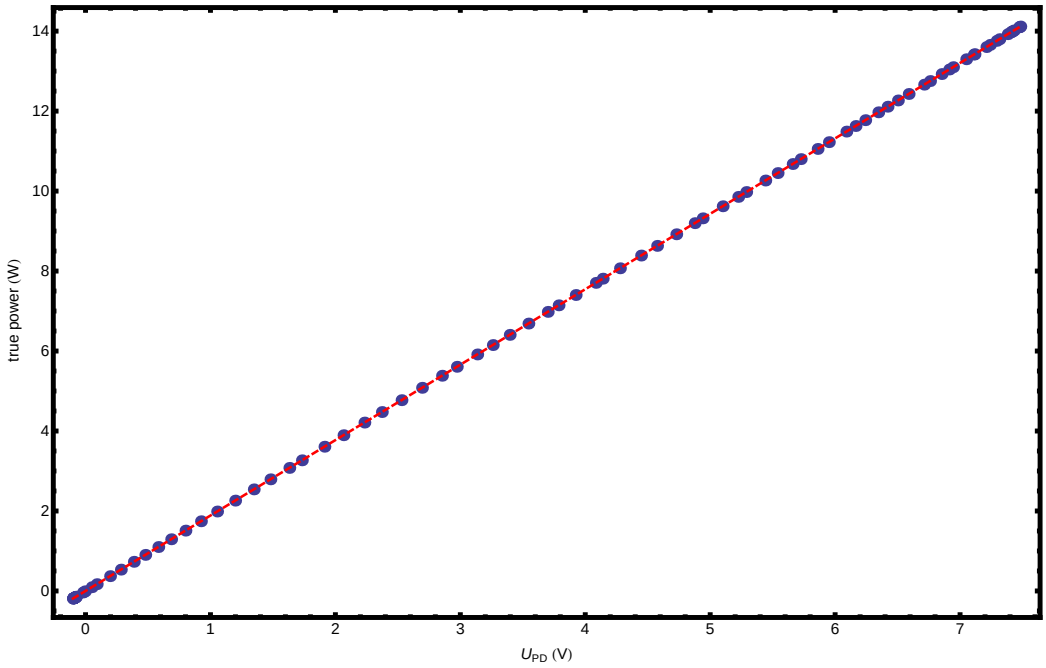

(c) The true power at the focus as a function of the control voltage. The blue dots are data points and the red dashed line shows a fit to the data.

Figure 4.21: Calibration of the optical dipole trap: In order to calibrate the optical dipole trap we slowly ramp the control voltage over the desired range and find therefore the response of the AOM as a function of the control voltage. The feedback on the actual power at the focus results in a linear function of the voltage of the photodetector.

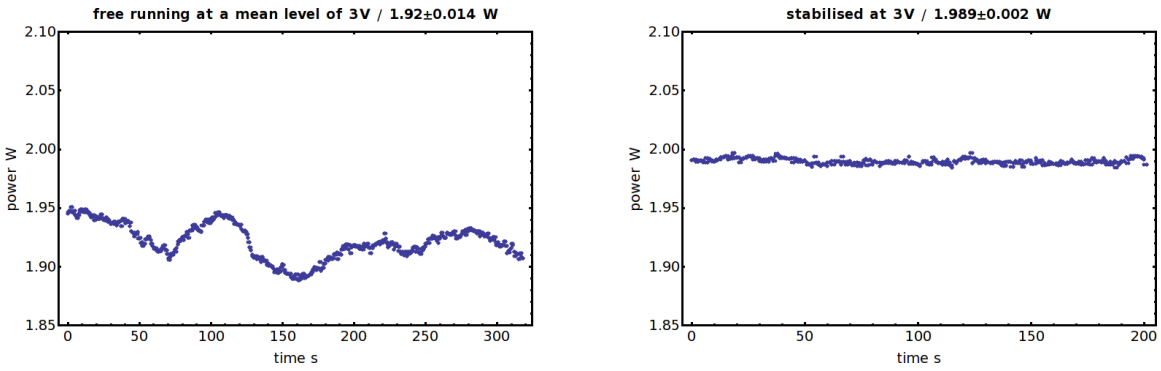

Figure 4.22: Power control without and with the feedback: The left figure shows the power fluctuation on an average power level of ∼2W. In the right hand figure with the feedback on the noise is significantly reduced and the average power is ∼2W as well.

Therefore one needs to know only the power of the laser beam at any point along the $V_{\mathrm{PD}} - V_{\mathrm{c}}$-line (see figure 4.21). By taking the offsets of the voltage and power measurement as well as losses along the beam-line lets us deduce the actual power of the laser beam at the point of the focus which we need to know to calculate the potential of the ODT. This system has been implemented on both beams and only differs in the constant attenuation on the output of the RF-amplifiers and the attenuation of light on the photodetector. In the left hand figure of figure 4.22 is shown the typical fluctuation of the laser measured on a power head at a power level of 1.9W. The mean and one standard deviation of the power is 1.92 ± 0.014W. The difference between the maximum and minimum measured power is 62 mW which is on the order of the power levels at the final evaporation and therefore too large. With the feedback on (see right hand in figure 4.22) power level remains constant and the noise on the data is determined by uncertainty of the used power head of 5mW. An example of a calibration of one of our dipole traps is shown in figure 4.21(c) which shows the linear relationship between the power at the focus and the voltage on the photodetector which is programmed as the reference in the sequence control.

4.5.2 Bandwidth of the noise eater

Loading the ODT and reducing the laser power to evaporate atoms from the dipole trap happens on very different time scales and powers. For loading of the ODT the power has to be high over seconds whereas the initial evaporation happens on the time scale of ms. In order to make sure that on the order of the trap frequency the bandwidth of the noise eater is high enough we modulate the reference voltage periodically. From those measurements we find that the noise eater follows a modulation up to 20kHz which is far beyond the highest expected trap frequencies. In figure 4.23 we see the modulation of the reference and the signal on the photodetecor. Please note that although the sampling of the sinusoidal signal is at the limit of the resolution of the computer cards the signal on the photo detector doesn't show any sudden steps.

4.6 Imaging atoms

Several detection techniques exist to image cold atoms each with different advantages and disadvantages. The three common techniques are phase-contrast imaging, fluorescence imaging and absorption imaging. Phase contrast imaging is a non destructive method where an atomic sample is imaged with a non resonant laser beam that is interfered with a reference laser beam. From the interference pattern one can determine the spatial structure of the atomic sample. The advantage is that for a large sample one can monitor the sample continuously in situ but the sample has to be dense to gain a high contrast. Spontaneous emission of light of an atomic sample can be monitored with a fluorescence technique, but the fluorescence of small samples produces only weak signals and requires large numerical apertures. The standard technique to detect cold atoms is absorption imaging which we will discuss in the following sections.

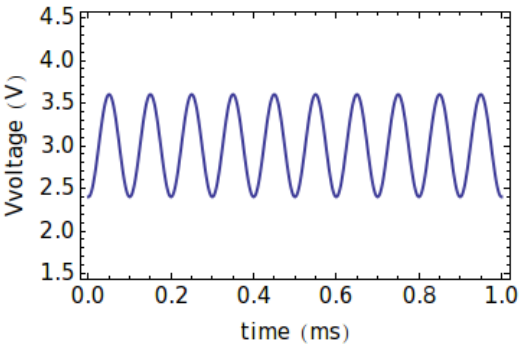

(a) Sinusoidal input signal.

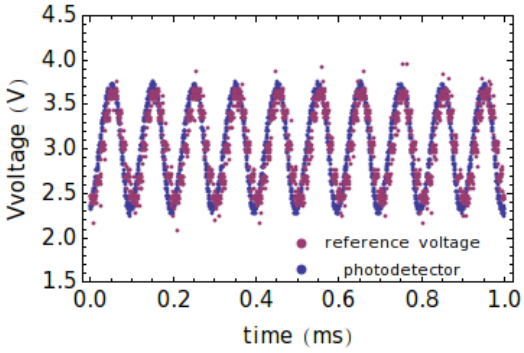

(b) Measured output signals.

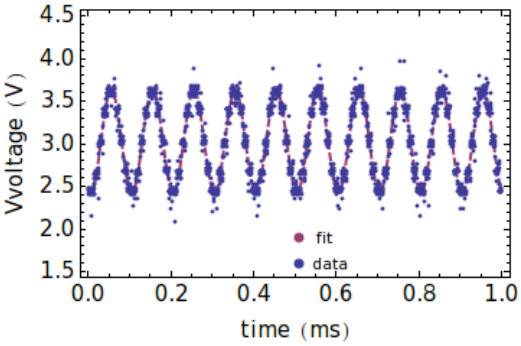

(c) Fit to the measured reference signal.

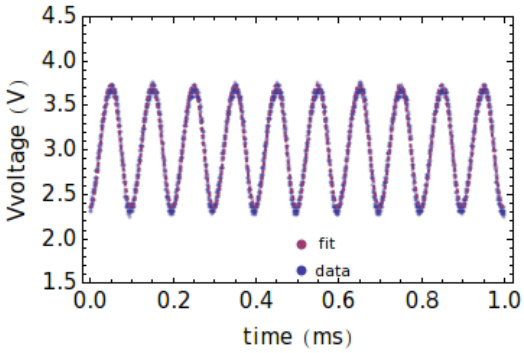

(d) Fit to the measured signal on the photodetector.

Figure 4.23: The upper left graph shows the programmed sinusoidal modulation4.23(a). The upper right shows the measured signal of the reference output voltage and the signal on the photodetecor4.23(b). Fits to the measured signals are shown for the reference voltage 4.23(c) and the voltage on the photodetecor 4.23(d). From the fits we determine a phase difference between the reference voltage and the voltage on the photodetector of 25.2° at a frequency of $f = 10$ kHz.

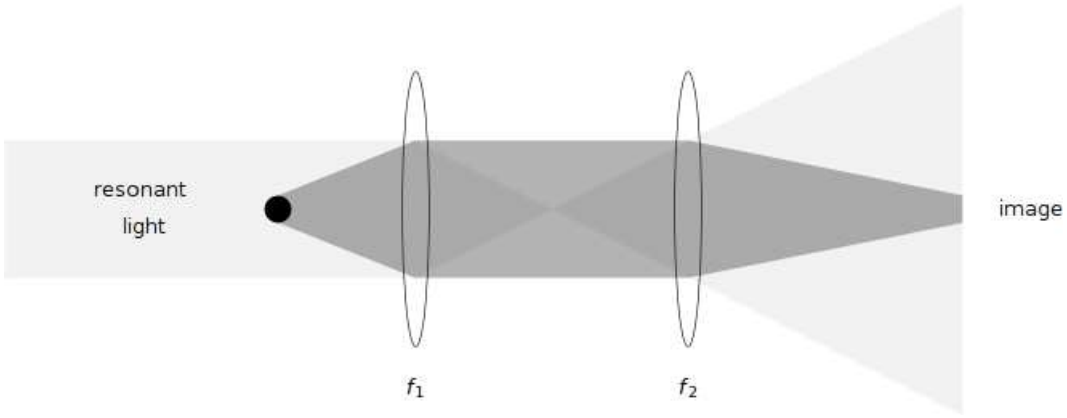

Figure 4.24: Principle of absorption imaging: A resonant laser beam is absorbed by the atomic sample. The 'shadow' is imaged by two lenses of focal lengths f_1 and f_2 onto a CCD camera.

4.6.1 Absorption imaging

A resonant probe beam passing through the cloud (see figure 4.24) will be absorbed and the intensity decreased according to the Lambert-Beer law

$$\frac{dI}{dz} = -n\ \sigma_0\ I \tag{4.2}$$

after transmission in z-direction through an atomic sample of density $n(x, y)$ with a resonant crossection σ_0. We can neglect saturation for intensities that are much smaller than the saturation intensity and find for the intensity of the transmitted light

$$I(x, y) = I_0(x, y)\exp(-\tilde{n}\sigma_0) \tag{4.3}$$

where $\tilde{n}$ is the integrated intensity along the axis of propagation or the column density. The image of this intensity would give a profile given by

$$S(x, y) = S_0(x, y)\exp(-\tilde{n}\sigma_0) + S_b(x, y) \tag{4.4}$$

where the additional term S_b arises from scattered background light. In order to determine the transmission we take three pictures on a CCD camera. One picture

is taken where the laser is attenuated by the cloud (absorption image) $\mathcal{A}$ (see figure 4.25(a)), one where the CCD is exposed only to the laser (reference image) $\mathcal{R}$ (see figure 4.25(b)) and a last one without any light illuminating the CCD (dark image) $\mathcal{D}$, (see figure 4.25(c)). The reference image should be taken immediately after the absorption image to minimise interference effects because of the coherence of the probe beam. This time frame is limited by the read out time of the camera. With these three images we calculate the transmission $\tilde{T}$ of the cloud via

$$\tilde{T} = \frac{\mathcal{A} - \mathcal{D}}{\mathcal{R} - \mathcal{D}}. \tag{4.5}$$

In figure 4.25(d) and 4.25(e) are shown two and three dimensional plots of a thermal cloud. Integrating the column density, which is given by $\tilde{n} = -ln(\tilde{T})/\sigma_0$ we find for the number of atoms

$$N = -\frac{A}{\sigma_0} \sum \ln \tilde{T} \tag{4.6}$$

where A is the area per pixel of the CCD camera. The three images are taken after a signal triggers the software to read out a camera which itself is triggered three times. One has to be careful that the time between the three images is long enough to read out the previous image before another is taken. The user can choose a folder in the software to save the pictures (16 bit/ *.tiff) which are taken and automatically given a filename that includes the date, which picture of the three it is and a number. In order to detect the atoms we illuminate the sample with a laser beam with a frequency of the $|F = 2\rangle \rightarrow |F = 3\rangle$ transition. Because of the resonant probe light for the imaging the atoms are accelerated due to absorption and spontaneous emission of photons. Let us assume that the sample of atoms is at rest before it illuminated with the probe beam. The displacement for an atom at rest is given given by the recoil velocity of the probe light v_{rec}, the number of scattered photons N_p and the exposure time t_{exp} by

$$\Delta x = \frac{1}{2} N_p \; v_{rec} \; t_{exp}. \tag{4.7}$$

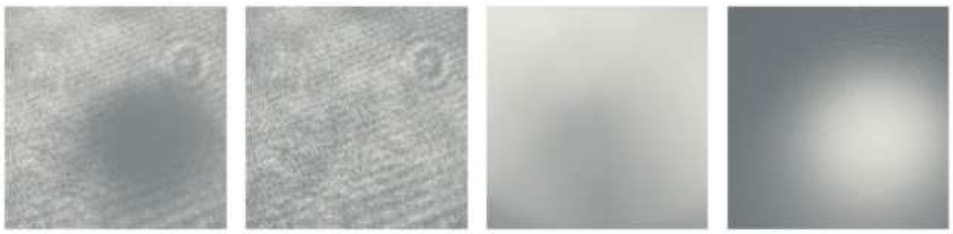

(a) Absortion image$\mathcal{A}$

(b) Reference image $\mathcal{R}$

(c) Dark image $\mathcal{D}$

(d) Calculated optical density $OD = (\mathcal{A} - \mathcal{D})/(\mathcal{R} - \mathcal{D})$

(e) Three dimensional representaion of the optical density

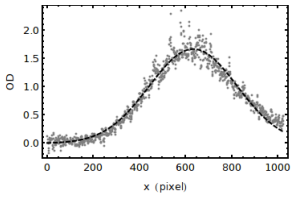

(f) Cross section along the x-direction of the cloud through the maximum (dots) and Gaussian fit (dashed line).

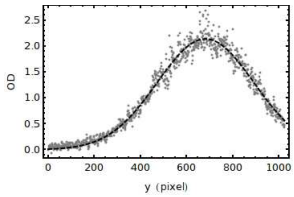

(g) Cross section along the y-direction of the cloud through the maximum (dots) and Gaussian fit (dashed line).

Figure 4.25: Imaging of cold atoms: The three images $\mathcal{A}, \mathcal{R}$ and $\mathcal{D}$ are taken in a sequence to determine the optical density. After evaluation of equation (4.5) one can plot two or three dimensional plots (figure 4.25(d) and 4.25(e)) of the optical density. In order to determine the width of the cloud Gaussian profiles are fitted to cross sections through the maximum of the cloud figure 4.25(f) and 4.25(g).

The velocity an atom at rest gains by absorption or emission of a photon is given by $v_{rec} = \hbar k/m$, where m is the mass of the atom, $\hbar$ Plancks constant and $k = 2\pi/\lambda$ the wavenumber of the probe light. The number of scattered photons is large near the resonance hence we can neglect the uncertainty and the number of photons is determined by the scattering rate (see (3.4)) and the exposure time $N_p = \Gamma t_{exp}$, therefore we find

$$\Delta x = \frac{\Gamma}{4} \frac{I/I_{sat}}{1 + \frac{I}{I_{sat}} + \left(\frac{\Delta}{\Gamma}\right)^2} \; v_{rec} \; t_{exp}^2. \tag{4.8}$$

For a short pulse of 50μs on resonance at an intensity of $I \approx 0.1 I_{sat}$ the displacement becomes 12.5μm. The diffuse image of a displaced point source appears to be a disk of radius $R_d = d/2f \; \Delta x$, with distance d and focal length f of the imaging system. For our example and an numerical aperture of 0.17 the radius of the disk is $1.5/mu$m and as we will see in the next section below the diffraction of the imaging system in our experiment.

4.6.2 Optics

Detection along gravity

We will discuss here the optical system being used. Optimal resolution is given if the imaging system is diffraction limited rather than aberration limited. The angle Θ where the first minimum of a diffraction pattern of a point source is observed through a circular aperture is given by

$$\sin\Theta = \frac{1.22\lambda}{a}, \tag{4.9}$$

where λ denotes the wavelength of the light and a the diameter of the aperture. The spot size D_{spot} of a point on a screen at distance d is given by

$$D_{\text{spot}} = 2 \; d \; \tan\left(\frac{\Theta}{2}\right). \tag{4.10}$$

The windows of the chamber have an aperture of $1.4''$ and the distance from the center of the chamber to the outer side of a window is 12cm. Substituting (4.9) in

(4.10) yields for the smallest distance where two points can be resolved

$$\mathrm{D_{spot}} = 2\ d\ \tan\left(\frac{1}{2}\ \arcsin\left(\frac{1.22\lambda}{a}\right)\right) \tag{4.11}$$

$$= 2.5\mu m. \tag{4.12}$$

The goal of the optimisation of the imaging system (see figure 4.24) was to find a suitable configuration of commercially available lenses. It is desirable that each single pixel of the CCD camera is exposed to just one single resolved spot. For the imaging a EC1380 Prosilica camera is used that has a pixel-size of $6.45\mu m$. Further details of the camera are described in appendix A. Those practical constraints require a magnification by a telescope of at least a factor of 2.5. Design and optimisation of the telescope was done with the ray-tracing program Optics Software for Layout and Optimization (OSLO). As a result both lenses $f1$ and $f2$ (compare figure 4.24) have to be a set made of two lenses in order to reduce aberrations and have to be spaced very precisely. The focal length of the first set is $f_1 = 348.2$mm (see figure 4.26(b)) and the second has a focal length of $f_2 = 116.1$mm (see figure 4.26(a)) with a magnification of $M = 3$. To test the resolving power of the telescope we used a test target of the US Air Force (test target 1951, see figure 4.27(a)) on which each element contains three bars in horizontal and vertical directions. These elements are part of groups and with increasing group and element number the number of line pairs per millimetre increases. Figure 4.27(b) shows an image taken with the Prosilica camera. The smallest structure that cannot be resolved is the 6th element of the 7th group (see figure 4.27(c)) which means that there are 228 line pairs per millimetre. Therefore the resolving power of the optical system is 2.2 μm e.g. the imaging is diffraction limited. The imaging system was optimised for the Prosillica camera with a pixel size of $6.45 \cdot 6.45\mu\mathrm{m}^2$ and taking the magnification into account a square of $\sim 2\mu$m is imaged onto one pixel. The camera from Prosillica was later replaced with a camera from Princeton Instruments. This camera has a lower noise and a higher sensitivity and a pixel size of $13.0 \cdot 13.0\mu\mathrm{m}^2$. Therefore the effective resolution decreases to $\sim 4\mu$m.

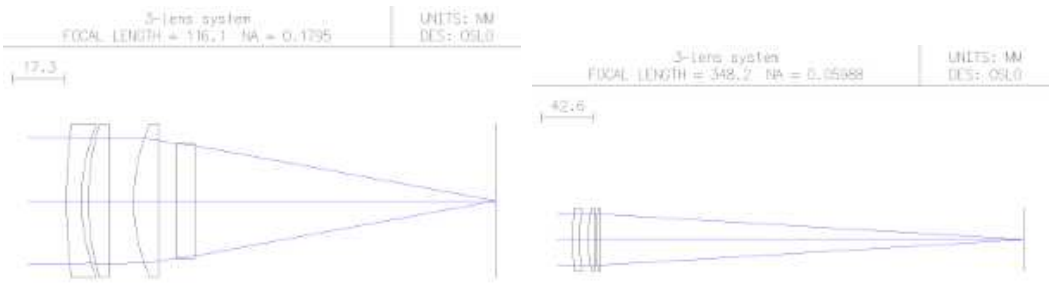

(a) The first with a focal length of f=116.1mm focuses on the atomic sample.

(b) The second doublet with a focal length of f=348.2mm focuses the image of the atomic sample onto a camera.

Figure 4.26: The diffraction limited system designed in OSLO. Two doublet lens systems of commercially available lenses are designed in OSLO to resolve near the diffraction limit of $\sim 2.2\mu$m.

The major disadvantage of imaging along the vertical axis is that for increasing time of flight the cold cloud of atoms drops out of the focal plane. The distance increases as $s = 1/2gt^2$ and after a typical time of flight of 15-25 ms the distance from the initial position of the cloud until it is detected has increased to $1 - 3mm$ which is larger than the depth of the focus.

Detection in the horizontal plane

To overcome the problem that during the time of flight the atom cloud drops out of the focal plane we set up another imaging direction in the horizontal plane. The optical system is much simpler and just consists one $f = 125$mm lens in a 2f-2f configuration with a magnification of ~ 1 (schematic in figure 4.28).

4.6.3 Cameras

For taking the absorption images two cameras were available. We can use the same camera we use for the continuous imaging of the fluorescent light of the MOT the Proscillica, or a Pixis camera with very low noise. Both configurations come with ad-

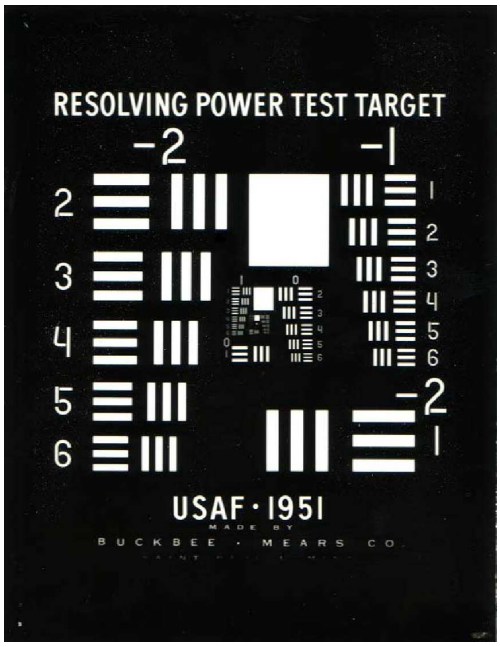

(a) Photocopy of the target 1951.

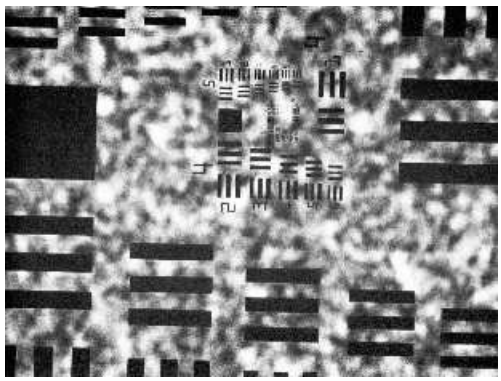

(b) An image taken of the inner structure of the target.

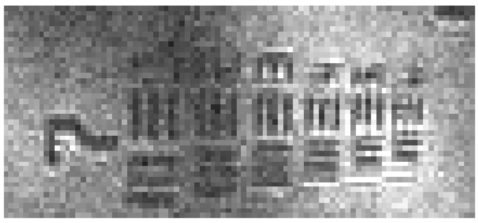

(c) The 7th group and its elements can be seen. Resolving the 5th group and just not the 6 means a spatial resolution of 2μm.

Figure 4.27: The resolving power of an optical system can be determined with the resolving power test target 1951. The largest bar that cannot be resolved determines the resolving power. The number of the group and element determines how many line pairs per millimetre are resolved.

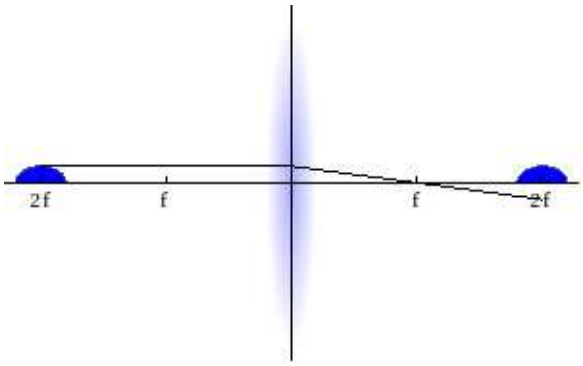

Figure 4.28: 2f-2f imaging in the horizontal plane.

vantages and disadvantages. The advantages of the Proscillica camera are automatic file saving and online preview of the absorption images with a self written program in Labview, but a higher noise on the camera. The advantage of the Pixis camera is the low noise at high sensitivity, but it comes with the disadvantages of having to start the camera manually. The software provided with the camera lets the user choose from various options and settings to set up the camera. For absorption imaging it is recommended to take one picture before the actual three pictures are taken in order to remove any residual charges on the camera. The readout time for large areas goes up to about 500ms which the operator of the experiment has to keep in mind when designing a sequence. The saved pictures are stored in a desired folder and are analysed using other software like Mathmatetica or MatLab.

4.7 Analysis of absorption images

In chapter 2 we derived an expression for the critical temperature T_c where Bose-Einstein condensation occurs and an expression for the fraction of condensed atoms for a temperature below T_c. That means that for a temperature of the atomic sample below the critical temperature both a thermal and a condensed phase are present with a characteristic bimodal distribution

$$n(\mathbf{r}) = \underbrace{n_{\mathrm{th}} \prod_{i=1}^{3} \mathrm{Exp}\left(-\frac{x_i^2}{\sigma_i^2}\right)}_{\text{thermal phase}} + \underbrace{n_{\mathrm{c}}\ \mathrm{Max}\left(0, 1 - \sum_{i=1}^{3} \frac{x_i^2}{r_i^2}\right)}_{\text{condensed phase}} \tag{4.13}$$

where n_{th} is the density of the thermal fraction at the centre of the cloud and σ_i is its width along the i-th direction; similarly n_{c} is the density of the Bose-Einstein condensate and its radii r_i. Along the imaging axis we measure the column density of the cloud. Thus we integrate (4.13) along one axis and rename the remaining coordinates ρ and z and find an expression for the column density the following

expression

$$\tilde{n}(\rho,z) = \tilde{n}_0 \exp\left[\left(\frac{\rho}{\sigma_\rho}\right)^2 + \left(\frac{z}{\sigma_z}\right)^2\right] + n_\mathrm{c}\ \mathrm{Max}\left[0, 1 - \left(\frac{\rho}{r_\rho}\right)^2 - \left(\frac{z}{r_z}\right)^2\right]^{3/2}. \quad (4.14)$$

Fitting (the fitting is performed in Mathematica, see appendix B) this function to the measured optical density works very well and we can determine the number of atoms in the two fractions by the separate integration of both profiles. In the following section we will discuss how important quantities are extracted from these profiles.

4.7.1 Temperature

In order to determine the temperature of an atomic ensemble the atoms are released from the trap and allowed to expand ballistically in free fall. Therefore the width σ of the atomic cloud grows as a function of time as

$$\sigma_i(t) = \sqrt{\sigma_{0,i}^2 + \tilde{v}^2 t^2} \quad (4.15)$$

where σ_0 is the initial size. The velocity distribution of the trapped atoms obeys the Maxwell-Boltzmann distribution with the most probable velocity $\tilde{v} = \sqrt{2\mathrm{k_B}T/m}$, with the Boltzmann constant $\mathrm{k_B}$, the mass m of the atom and temperature T. About 60% of atoms are within the range of zero velocity and the most probable velocity $\tilde{v}$. The trapped ensemble will expand when released from the trap to a size proportional to the square root of the temperature of the ensemble. Taking images for different time of free expansion we can determine the temperature from fitting $\sigma(t)$ to our data and extracting the most probable velocity and rearranging for $T = \tilde{v}^2 m/k_\mathrm{B}/2$. We can also determine the temperature from two measurements if the time of flight is short and the temporal difference of the two measurements is small or the time of flight is long e.g. $\tilde{v}^2 t^2 \gg \sigma_{0,i}$, where the initial size of the cloud becomes negligible, we can approximate the temperature by

$$T = \frac{m}{k_\mathrm{B}} \frac{\sigma_2^2 - \sigma_1^2}{t_2^2 - t_1^2}. \quad (4.16)$$

The temperature of the ensemble can also be determined from only one image if one knows well the initial geometry of the trap e.g. the trap frequencies (ω_i) and if the time of the expansion is larger than mean trapping frequency $t_{\mathrm{TOF}} \gg \bar{\omega}^{-1}$, where $\bar{\omega} = (\omega_1\omega_2\omega_3)^{1/3}$. Then we find the following expression for the temperature [5]

$$T = \frac{m}{k_{\mathrm{B}}} \frac{\omega^2 \sigma(t)^2}{1 + \omega^2 t^2}. \tag{4.17}$$

4.7.2 Phase space density

An important parameter to know is the phase space density which is given by

$$PSD = n\lambda_{\mathrm{dB}}^3, \tag{4.18}$$

where n is the density of the atoms and λ_{dB}^3 the thermal de'Broglie wavelength. Knowing the temperature and the peak density we can calculate this by

$$PSD = n_0 \frac{h}{\sqrt{2\pi m k_{\mathrm{B}} T}}. \tag{4.19}$$

We can also write the phase space density as a function of the number of atoms N, the temperature T and mean trapping frequency $\bar{\omega}$

$$PSD = N \left(\frac{\hbar\bar{\omega}}{k_{\mathrm{B}} T} \right)^3. \tag{4.20}$$

4.7.3 Fringe removal

The coherence of the imaging beam causes interference patterns caused by mechanical noise. The phase of the fringes of the interference patterns are randomly distributed over the interval $\{0..2\pi\}$. For small numbers of atoms at a long time of flight the height of the fringes can be as high as 10% of the maximum optical density. These fringes lead at times to a negative number of atoms when calculating the number of atoms by equation (4.6). The noise caused by the fringes can be reduced significantly by using the following technique which is described in more detail in [70, 71, 72]. The basic idea of this technique is to compute for an absorption $\mathcal{A}$ a reference image $\mathcal{R}$

from a linear superposition of a set of reference images $\mathcal{R}_1 ... \mathcal{R}_N$, e.g. $\mathcal{R} = \sum_i^N c_i \mathcal{R}_i$. The coefficients c_i are determined by a scalar product of the absorption image $\mathcal{A}$ and the reference image $\mathcal{R}_i$. Each individual reference image shows a different noise pattern caused by various reasons. Therefore by determining the coefficients c_i will encounter for noise caused in a given absorption image. Similar to the Gram-Schmidt algorithm where we find for a set of given vectors a orthonormal basis, we want to find an orthonormal basis $\mathcal{B}_1 .. \mathcal{B}_n$ of images for a set of reference images $\mathcal{R}_1 ... \mathcal{R}_n$. Projecting the absorption image $\mathcal{A}$ onto this basis gives the reference image $\mathcal{R}$ to the absorption image $\mathcal{A}$. First define the following scalar product of two images $\mathcal{I}$ and $\mathcal{J}$ by

$$(\mathcal{I}, \mathcal{J}) = \sum_{y_{min}}^{y_{max}} \sum_{x_{min}}^{x_{max}} \mathcal{I}[y, x] \; \mathcal{J}[y, x] \tag{4.21}$$

where $\mathcal{I}[y, x]$ is the value of the image $\mathcal{I}$ of the pixel at $[y, x]$. From a set of reference images $\mathcal{R}_1 .. \mathcal{R}_N$ we calculate the basis set $\mathcal{B}_1 .. \mathcal{B}_N$ via

$$\begin{aligned}
\mathcal{B}_1 &= \frac{1}{\sqrt{(\mathcal{R}_1, \mathcal{R}_1)}} \cdot \mathcal{R}_1 \\
\mathcal{B}_2 &= \frac{1}{\sqrt{(\mathcal{C}_2, \mathcal{C}_2)}} \cdot \mathcal{C}_2 \quad \text{with} \quad \mathcal{C}_2 = \mathcal{R}_2 - (\mathcal{R}_1, \mathcal{B}_1) \cdot \mathcal{B}_1 \\
&\vdots \\
\mathcal{B}_j &= \frac{1}{\sqrt{(\mathcal{C}_j, \mathcal{C}_j)}} \cdot \mathcal{C}_j \quad \text{with} \quad \mathcal{C}_j = \mathcal{R}_j - \sum_{1 \le i < j} (\mathcal{R}_j, \mathcal{B}_i) \cdot \mathcal{B}_i
\end{aligned}$$

With this basis set of images we project the absorption image $\mathcal{A}$ onto this basis to find the reference image $\mathcal{R}$ by

$$\mathcal{R}' = \sum_{i=1}^{N} (\mathcal{A}, \mathcal{B}_i) \cdot \mathcal{B}_i \tag{4.22}$$

and after normalisation

$$\mathcal{R} = \frac{||\mathcal{A}||}{||\mathcal{R}'||} \cdot \mathcal{R}'. \tag{4.23}$$

The norm we used here is given by

$$||\mathcal{I}|| = \sum_{y_{min}}^{y_{max}} \sum_{x_{min}}^{x_{max}} \mathcal{I}[y, x] - \sum_{f_{y_{min}}}^{f_{y_{max}}} \sum_{f_{x_{min}}}^{f_{x_{max}}} \mathcal{I}[y, x] \tag{4.24}$$

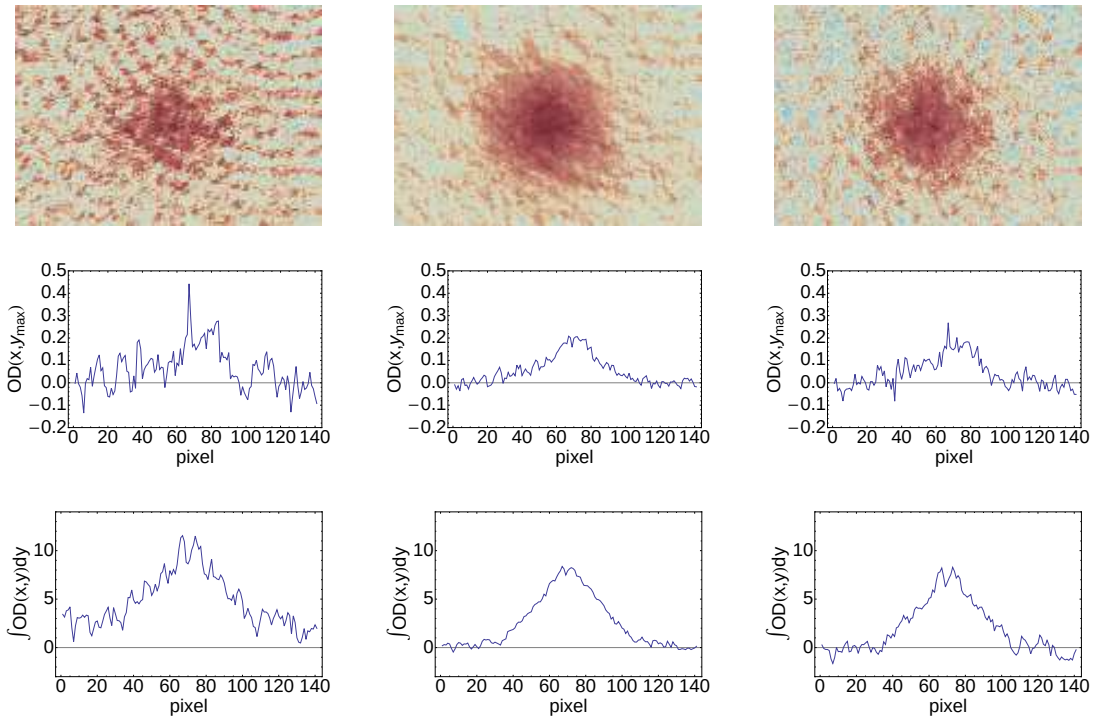

(a) A noisy image (b) Mean of nine images (c) Removed fringes with an optimal reference image

Figure 4.29: Removing fringes by the mean and an optimal reference image: The noise from fringes of an image 4.29(a) can be reduced by taking the mean of consecutive images 4.29(b) or using an optimised reference image 4.29(c) as descried in the text. The outer frame and inner frame 4.30 to calculate the norm of (4.24)

where the summation over $[f_{y_{min}}, f_{y_{max}}]$ and $[f_{x_{min}}, f_{y_{max}}]$ is a frame in the image $\mathcal{I}$ that contains the atoms see figure 4.30. With this technique we can improve the quality of an image strongly distorted by fringes 4.29(a) as we can see in figure 4.29. To remove the fringes in the image shown in figure 4.29(a) we took a series of nine images where the image 4.29(a) was the worst distorted in the series. We use the same series to calculate a basis containing nine orthogonal reference images to remove the fringes. In figure 4.29(c) the fringes are removed with the method describes above. In figure 4.29(b) the mean of these nine images is shown and it still shows a distinctive

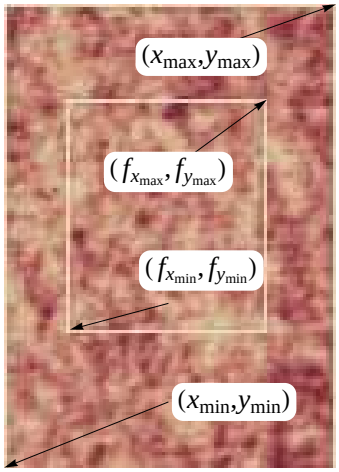

Figure 4.30: Frames of the norm given in (4.24)

fringe pattern. Removing those fringes comes at a cost. It is not economic to use all pictures in a data set to calculate the basis set. A less extensive way is described in [71] which we just want to outline here. From a series of images one chooses a subset of images which are normal according to the scalar product given in (4.21). This subset of images is then used to determine the optimal reference image of the series.

5 MOT

To obtain an ensemble of cold atoms one has to slow down atoms released from a source at a much higher temperature. In our experiment we can release ^{87}Rb atoms from a source at a temperature of a few hundred Kelvin and cool them in a magneto-optical trap [73] (see section 3.1) to a few hundred micro Kelvin. Using a temporal dark MOT and molasses cooling (see section 3.2) we can increase the density and decrease the temperature to improve the trapping in a optical dipole trap.

5.1 Optimisation of the MOT

In chapter 3 we discussed a simplified model of a MOT and extended the model for ^{87}Rb. The optimum operation of a MOT depends on several parameters which have to be determined experimentally. In the following sections we will investigate the influence of these parameters on the capture efficiency, density, temperature and number of atoms in order to find the optimum operation of the MOT in the experiment. The MOT can be loaded in two different ways. We either increase the background pressure of ^{87}Rb by releasing ^{87}Rb atoms from a hot source or by turning on a source of UV-light which ejects ^{87}Rb from the interior surfaces [74].

5.1.1 Magnetic field gradient

In order to investigate the loading as a function of the applied current in the anti-Helmholtz configuration we loaded the MOT only by ejecting ^{87}Rb atoms from interior

surfaces by turning on a source of UV-light. Figure 5.1 shows the number of atoms as a function of time and the loading rates[1] (see section 3.2.2) for the applied current. A lower current results in a weaker gradient and therefore a weaker trap but with a larger trapping volume. While a higher current produces a stiffer trap but with a smaller volume. We are able to take advantage of this in the following way: we load the MOT at a lower current but then increase the current to compress the cloud to optimise the loading into the optical dipole trap. We find the fastest rate at a current

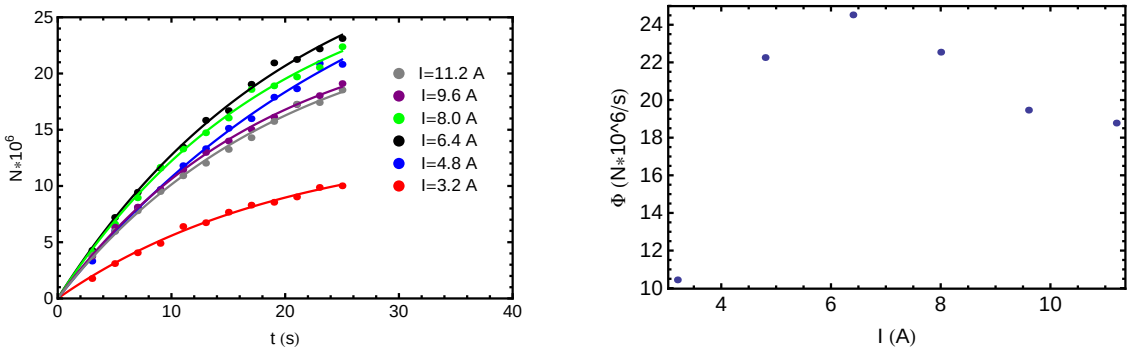

(a) Number of atoms in the MOT as a function of time.

(b) Loading rates of the MOT for different currents.

Figure 5.1: The dependence of the loading of the MOT for different currents and the loading rates at each current.

of 6.4 A which results in a weakly confined MOT. A higher current results in a lower loading rate but a tighter confinement which also enhances the density in our MOT.

5.1.2 Intensity of the MOT laser

We vary the power of the MOT beams at a constant current to investigate the influence on the loading of the MOT. In figure 5.2 we can clearly see that we trap more

[1]The number of atoms in the MOT as a function of time during the loading is given by $N(t) = N_{\max}(1 - e^{-t/\tau})$, where $N_{\max}$ is the maximum number of atoms in the saturated MOT and τ a time constant given by the losses of atoms from the MOT. The loading rate Φ is given by the ratio of maximum number of atoms in the MOT $N_{\max}$ and the time constant τ, $\Phi = N_{\max}/\tau$.

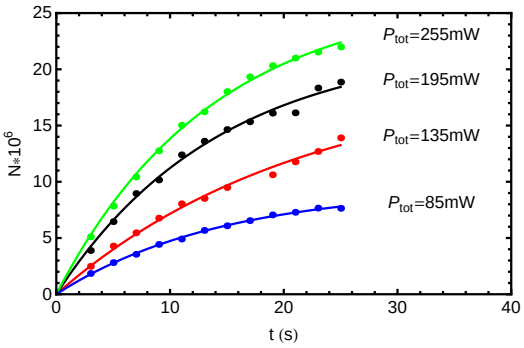

(a) Loading curves for different total powers of the MOT beams.

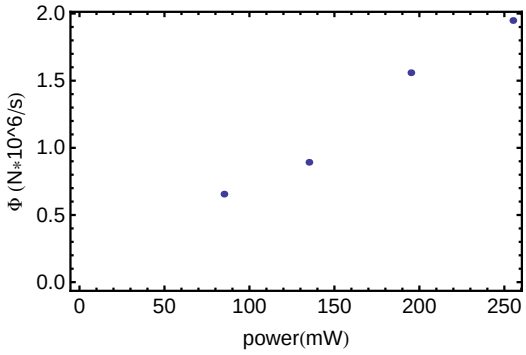

(b) Loading rates for different total powers of the MOT beams.

Figure 5.2: Number of trapped atoms as a function of the laser power of the MOT beams. We find for higher powers more trapped atoms and higher loading rates.

	Trapping laser	repumper	Quadrupole field	
Intensity	200mW	20mW	current	9-11 A
detuning	-2.6 Γ	0	gradient	8.1-9.9 G/cm
diameter	2.5cm	2.5cm		

Table 5.1: Typical operating parameters of the MOT.

atoms at a higher loading rate at a higher total power of the MOT beams.

5.2 Summary of all MOT parameters

Let us summarise the parameters of the MOT in tables showing operating parameters and measured quantities of the MOT. The gradients used are typical but the large diameters of the beams and the power of 200mW led to a saturation intensity of $\approx 1.6 I_0$ resulting in smaller number of atoms in the MOT. In the next we will show how the MOT was improved significantly by replacing the cooling laser with a more powerful one and replacing the free space MOT with a fibre coupled MOT.

Experimental MOT parameters	
N	$\sim 25\ 10^6$
n	$\sim 4.5\text{cm}^{-13}$
T	$\sim 200\mu$K (after molasses 50μK)
phase space density	$\sim 10^{-7}$
loading rate	$\sim 30\ 10^6$ atoms/s

Table 5.2: Measured properties of the MOT.

5.3 Fibre coupled MOT

A major problem that occurred with the MOT, when the beams were propagating in free space, e.g. the distribution of the light and the transfer of the six beams by using mirrors, was the instability of the alignment and overlap of the MOT beams with the repump beam and the drift of the MOT beam alignment with respect to the magnetic field. We improved the set up by replacing the free space propagating beams by fibre coupled beams. In figure 5.3(a) we see in the right hand corner the fibre couplers of the repumper and cooling laser. Both beams overlap behind a polarising beam splitter and pass through a telescope. They are distributed onto three separate arms, split into two and each single beam passing through another telescope before entering the science chamber. As the position of the MOT shifted, the loading was not optimal or alternatively the power balance of the beams changed noticeably from day to day. It proved a time consuming procedure to optimise our MOT, and the wish to simplify the optical system made us to decide to replace the free space MOT optics with a fibre coupled system. Distributing the light for the MOT beams with half wave plates and polarising beams splitters did not change but instead of delivering the light into the chamber with free space mirrors we coupled each beam into an individual polarisation maintaining fibre (Thorlabs PM-780). At the bare end of the fibre we mounted a quarter wave plate and a $f = 100$mm lens assembled in a $1''$ tube

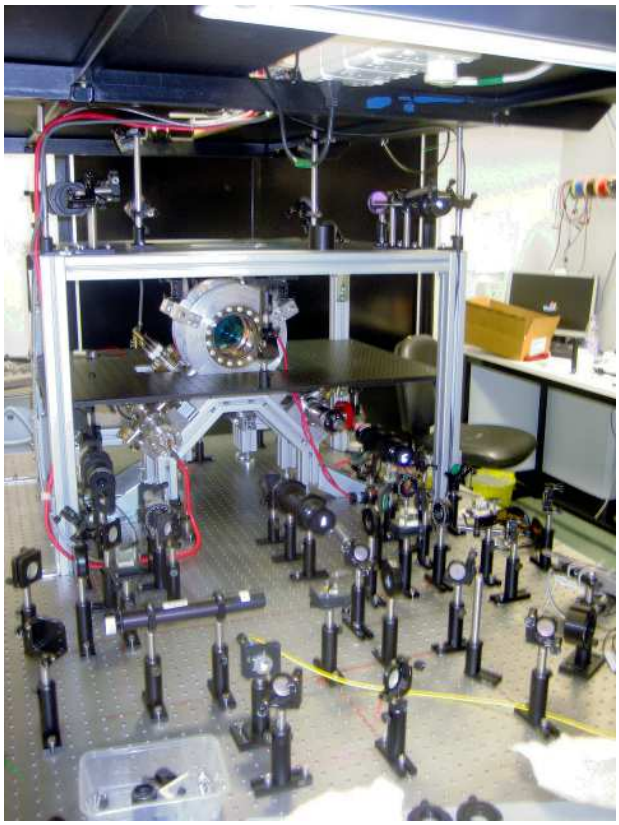

(a) Photograph of the set up. In the foreground are the optics distributing the light onto the six arms of the MOT.

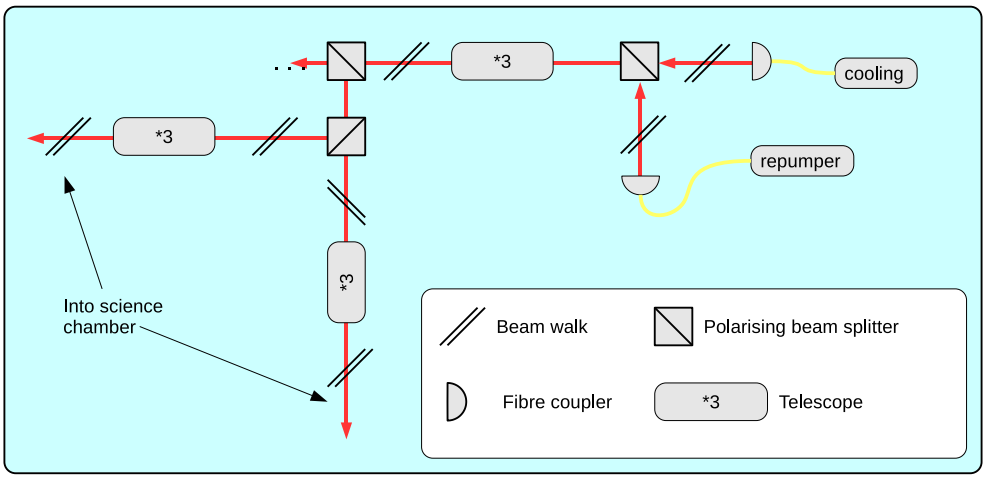

(b) A schematic of the optics of the free space MOT.

Figure 5.3: A schematic of the free space MOT and a schematic showing the distribution of the light. Further description see text.

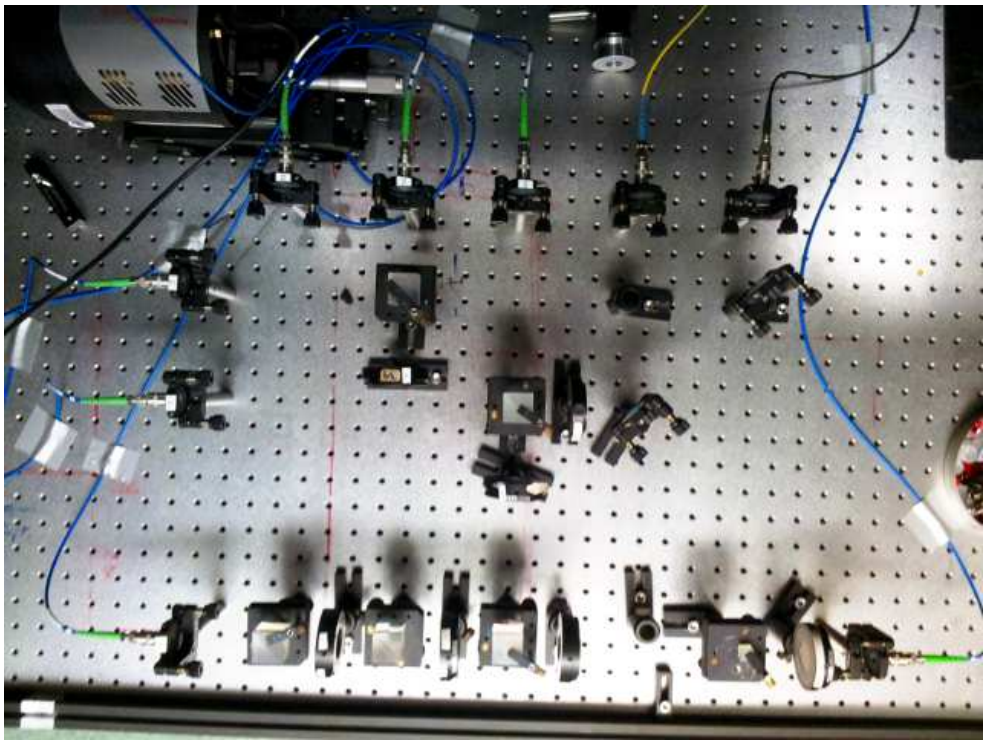

(a) The simple and easily maintained set up according to the scheme in figure 5.4(b).

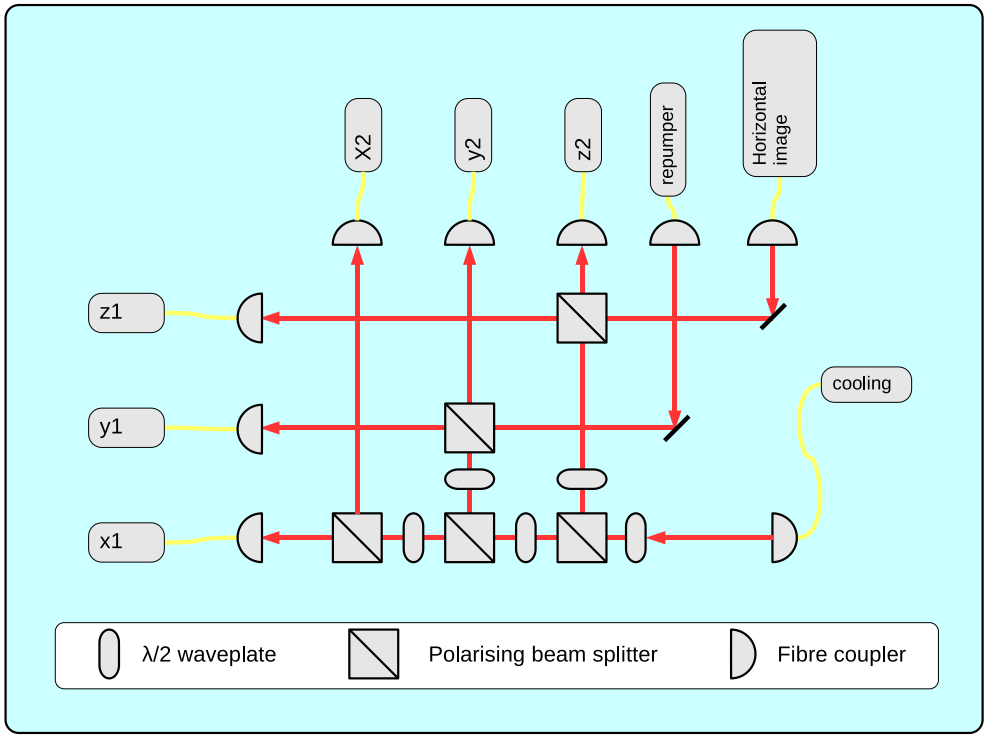

(b) Schematic overview of the fibre coupled MOT.

Figure 5.4: A schematic of the fibre coupled MOT and a schematic showing the distribution of the light. For description see text.

Experimental fibre MOT parameters	
N	up to $95 \cdot 10^6$
n	up to 10^{14}cm^{-3}
T	$\sim 200\mu$K (after molasses 50μK)
phase space density	$\sim 10^{-6}$

Table 5.3: Typical operating parameters of the fibre MOT.

system (see figure 5.4(b)and 5.5). By adjusting the wave plate we can choose the polarisation and collimate the beam with the position of the lens. These tubes were mounted in front of the chamber. Although the beams were smaller in their diameter than the free space MOT ($\varnothing 2''$) the saturation level increased to $I/I_0 \sim 5.5$. With the fibre coupled MOT we trap up to $100 \cdot 10^6$ atoms (see figure 5.7) and achieve a temperature of $T = 50\mu$K after the compression in the MOT which we will describe in the next section.

5.3.1 Compression and temporal dark MOT

The density and temperature of the atoms trapped by the MOT can be significantly improved by compressing the sample and applying a temporal dark MOT. The first technique simply means that the gradient is increased such that the trapped atoms

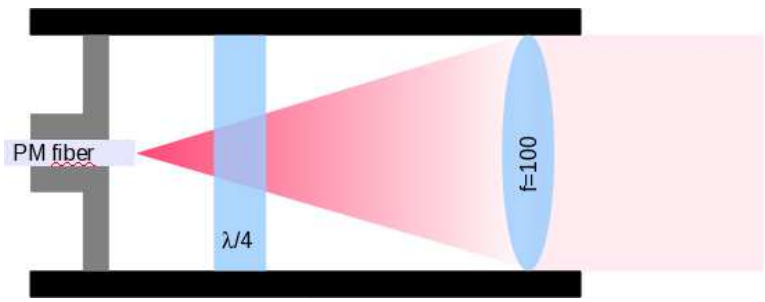

Figure 5.5: To collimate and adjust the polarisation of the trapping beams of the MOT a quarter wave plate and a $f = 100$mm are mounted into a $1''$ tube with the fibre mount.

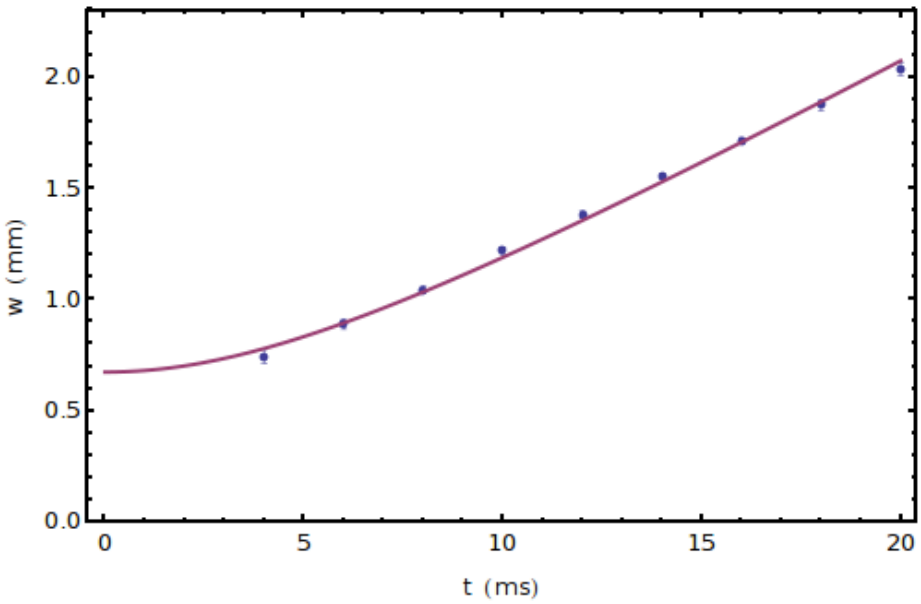

Figure 5.6: Expansion of the MOT after compression and a temporal dark phase. Analysis indicates a temperature of 50μK using (4.15).

are trapped in a smaller volume hence the density is higher. During the dark temporal MOT the intensity of the repumper is lowered to just a fraction of its initial intensity and the detuning of the trapping beams is increased further. With applying these two techniques to the sample after loading the MOT we trap nearly $50 \cdot 10^6$ atoms at a temperature of T=50μK (see figure 5.6) and a density of $\sim 10^{14}\text{cm}^{-3}$. At this stage the phase space density is a about $\sim 10^{-6}$ and further evaporation is required to reach quantum degeneracy. How we achieve this in an optical dipole trap we will discuss in the following chapter.

5.3.2 Initial number of atoms in the MOT

While attempting to maintain constant conditions for the loading of the dipole trap and evaporation one has to keep in mind that with every run of the sequence the background pressure of ^{87}Rb increases slightly. In figure 5.7 we see the long term

behaviour of the number of atoms in the MOT over time for varying the current through the dispenser. This data was taken such the sequence was running back to back over at least 18 repeats. Without the dispenser we load from the remaining background into to the MOT and about $17.5 \cdot 10^6$ are left after the compression. Loading the MOT at current of 5A increases the number of atoms almost linearly but does not plateau fast. Loading the MOT at 5.4 A through the dispenser the number of atoms after the compression of the MOT plateaus after nearly ten repeats and remains almost constant at $38 \cdot 10^6$ atoms. We observe a slow increase in the number of atoms after the compression of the MOT at current of 5.8A. Here it takes about 20 repeats to settle the number of atoms at nearly $100 \cdot 10^6$ atoms. Loading at a higher current will increase the initial number of atoms in the optical dipole trap but will also increase collisions with the hot background gas.

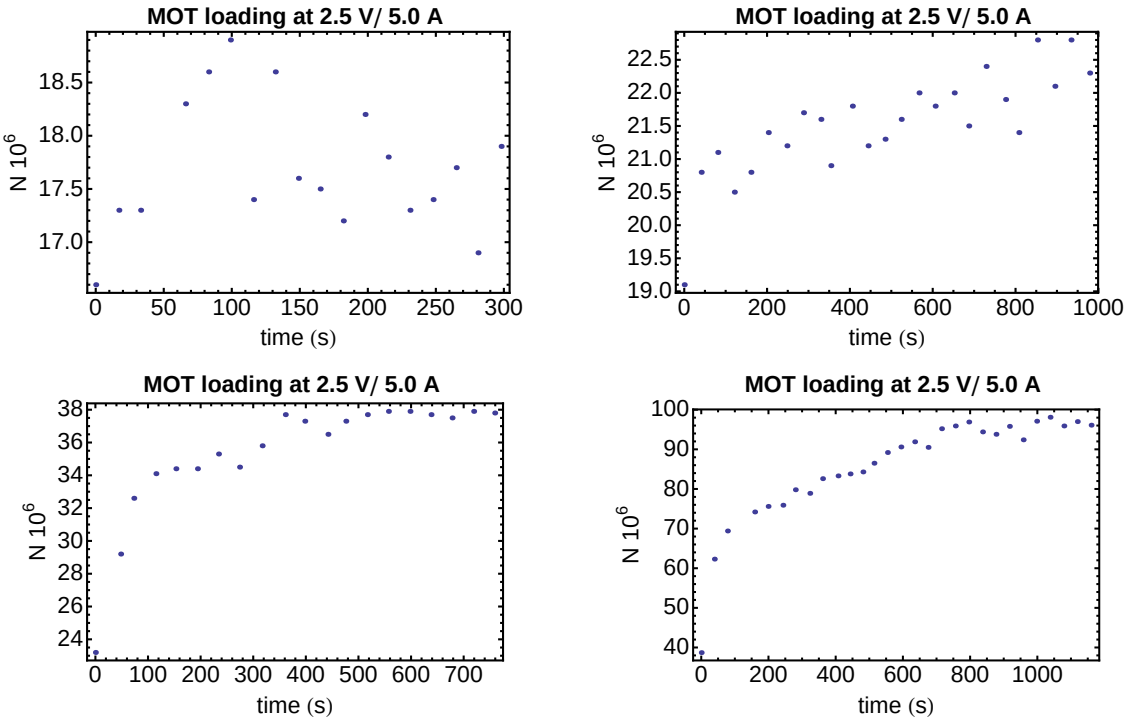

Figure 5.7: Loading of the MOT for different currents of the dispenser. Loading the MOT just by increasing the background pressure with the UV light loads about $20 \cdot 10^6$ atoms into the MOT (upper left figure). At a current of 5A in the dispenser the number of atoms in the MOT builds up very slowly over time (upper right figure). For a current of 5.4 A the number of atoms in the MOT settles after 10 successive runs of the sequence at about $30 \cdot 10^6$ atoms and at a current of 5.8 A at $95 \cdot 10^6$atoms.

6 Evaporation to BEC in an ODT

In the previous chapter we discussed the physics of a MOT. We saw that the key of trapping and cooling of atoms in a MOT is near resonant scattering of photons with a spatial dependency of the absorption probability. We also saw that in a MOT we can not reach a temperature and phase space density sufficient to undergo the phase transition to Bose-Einstein condensation.

In section 3.3 we discussed the physics of trapping neutral atoms in a far detuned focused laser beam. We also introduced the technical realisation and control of the optical dipole traps in section 4.5. In this chapter we will discuss the dynamics of the loading and evaporation in our traps.

6.1 Concepts and general ideas

The previous comprehensive discussion about the optical dipole force (see section 3.3) will now allow us to discuss the general concept of trapping and cooling atoms in a optical dipole trap and compare it qualitatively to the more common approach in a magnetic trap [75, 76, 77]. A typical initial condition for evaporative cooling in an optical dipole trap is that the depth of the trap is 10 times deeper than the temperature of the atomic ensemble i.e. $\eta = U_0/k_{\mathrm{B}}T \sim 10$. However, by simply lowering the power of the laser of a single beam trap the depth of the trap becomes shallower and it becomes more likely for the hottest atoms to escape the trap. By reducing the power one also weakens the confinement. Along the radial direction the trapping frequencies are usually still on the order of $2\pi f = \omega \sim$1kHz at lower powers

but the confinement along the axial direction decreases to a few Hz. The atoms spread out along the axial direction diluting the density at the centre of the trap but where a high density is essential to provide a fast elastic collision rate and hence a higher thermalization rate. To confine the atoms along the weak direction of the dipole trap one can cross two beams to provide a stronger confinement and also to provide an isotropic geometry of the potential. In the combined trap the power is further decreased until the temperature of the remaining atoms in the trap falls below the critical temperature for Bose-Einstein condensation. In an optical dipole trap using a linearly polarised laser the trapping is independent of the spin state, in contrast to a magnetic trap (see figure 6.1). In a magnetic trap the harmonic potential is given by the geometry of wires conducting a current. Highly energetic atoms are rejected from the trap by driving RF-transitions in to a non-trappable state. This takes energy out of the remaining ensemble and the remaining atoms rethermalise by elastic collisions to a lower temperature. The geometry of the potential remains constant the during the evaporation. Typical dipole traps for evaporative cooling are formed with $C0_2$ [20, 67, 78, 79, 80] laser operating at $\lambda = 10.6\mu$m or at $\lambda = 1565$nm [81] and more recently fibre lasers with a wavelength of $\lambda = 1064$nm are used as well [20]. A larger detuning comes at the cost of higher power for a constant potential but a longer wavelength also means another trap geometry as shall be seen. Typical waists of optical dipole traps range from 20μm to 80μm. Let us assume a waist of 30μm for two beams at wavelengths of $\lambda_1 = 10.6\mu$m and $\lambda_2 = 1064$nm. The Rayleigh lengths for beams are $z_{\mathrm{R1}} \sim 0.26$mm and $z_{\mathrm{R2}} \sim 2.62$mm. A ten times larger wavelength results in a ten times smaller Rayleigh length, this is particularly important in a crossed optical dipole trap, see figure 6.2. The potential for λ_1 is isotropic whereas for $\lambda = \lambda_2$ the trap has a dimple at the intersection of the two beams. The effective depth of the dimple for the beam of $\lambda = \lambda_2$ is just $U_0/2$ and atoms which are hotter than that reside in the wings of the potential. A detailed model by [82] show the population of atoms in the wings as a function of the two wavelengths λ_1 and λ_2 as

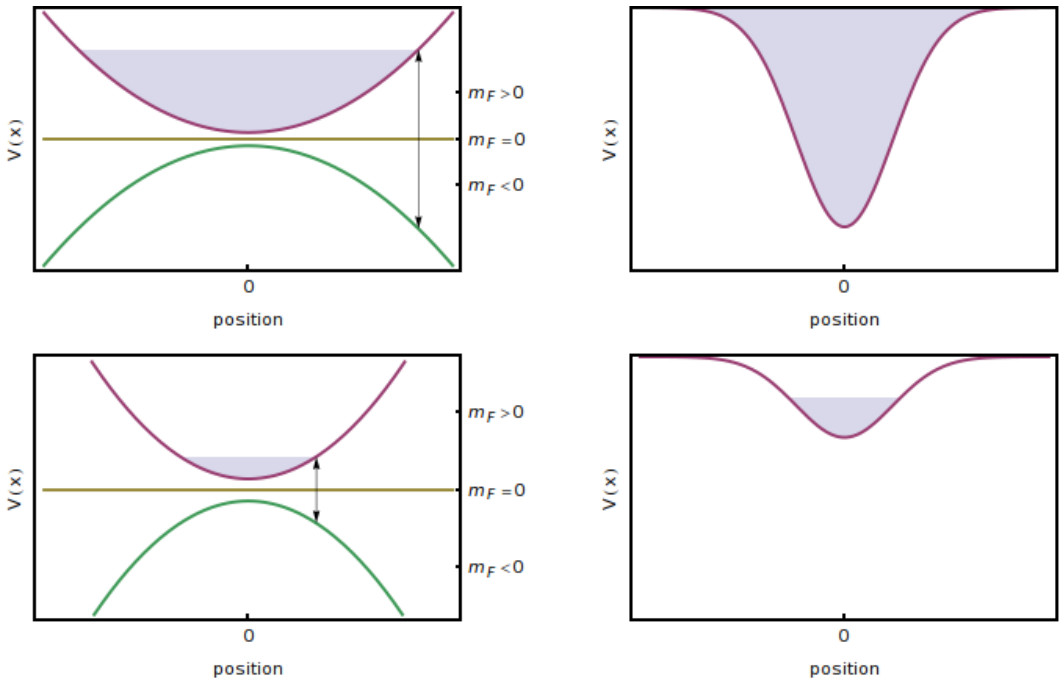

Figure 6.1: Principle of the evaporation in a magnetic trap (left hand side) and a optical dipole trap (right hand side); for a higher temperature (top row) and lower temperature (bottom row). In a magnetic trap the potential for a given spin state remains constant, whereas in an optical dipole trap the trapping is spin independent but the potential changes in time.

a function of the ratio of the kinetic energy and the 'true' depth of the potential. The general conclusion of this model shows that for a larger wavelength, hence a shorter Ryleigh length, fewer atoms populate the wings and for a shorter wavelength one needs a deeper trap to suppress the population of the wings. Furthermore the positioning of the optical trap with respect to the atomic cloud that it is loaded from depends on the temperature of the cloud, the power and the wavelength of the laser for the optical dipole trap. Again we want to simplify the discussion so we only vary the wavelength of the optical dipole trap and leave all other parameters constant. Usually optical dipole traps are loaded from a magneto-optical trap.

The larger the surface area of the optial dipole trap which atoms can enter the more atoms are trapped in the optical dipole trap. A simple model to maximise the number of atoms in the ODT was developed by [83] and experimentally verified by [84]. By approximating the volume of the trap with a cylinder of the length of the diameter D of the MOT and a radius r from the axis of propagation of the ODT to an equipotential line, if the Rayleigh length is larger than the diameter of the MOT ($z_{\mathrm{R}} \gg \varnothing_{\mathrm{MOT}}$). The volume given by this trap is $V = \pi D r^2$. At the focus of the trap the radius of this cylinder is the smallest and it becomes larger further away from the focus has a maximum and decreases again (see figure 6.3). With increasing radius the volume of the trap increases as well. In order to find the optimum position we basically use equation 3.25 for a constant potential (temperature) and vary the radius r. Setting $U(r,z) = U_c \sim k_{\mathrm{B}}T$ and solving for the radius we find

$$r(z) = \sqrt{\frac{w_0^2}{2}[1 + (z/z_{\mathrm{R}})^2]\ln\left(\frac{U_0}{U_c}\frac{1}{1 + (z/z_{\mathrm{R}})^2}\right)} \tag{6.1}$$

where w_0 is the waist of the trap at the focus, z_R is the Rayleigh length, U_0 the depth of the trap and U_c the cut off depth. This model is based on the idea of maximising the surface area A of the ODT through which the atoms are entering the ODT [80]. We call the distance from this position to the centre of the ODT $z_{\max}$. Figure 6.3 shows the radius as a function of the distance from the centre for two different wavelengths

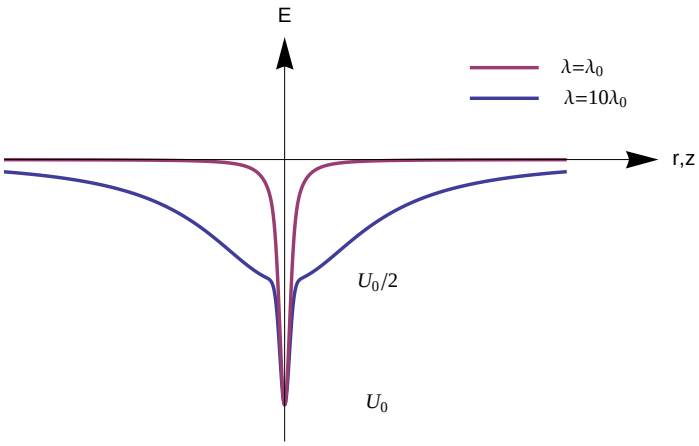

Figure 6.2: Two different potentials for wavelengths at $\lambda = 10\lambda_0$ (purple line) and $\lambda = \lambda_0$ (blue line), but same power and waist as a function of one direction through the centre of the trap.

where one is ten times larger than the other and $\eta = U_0/U_c = 10$. The y-axis is in units of the radius in the centre of the trap and r_0 denotes the radius to equipotential line at the focus of the trap. Therefore we see that for these conditions the optimum of the radius is just $\sim 1.26r_0$, whereas the axial positions of the optima differs by a factor ten. The dashed lines indicate the size of the MOT and the shaded area would be a partial volume of the MOT from where the atoms are loaded into the ODT. Therefore the axial overlap of the centre of the MOT and of an optical dipole trap at a wavelength of 1064nm is not as critical as for for a trap at a larger wavelength. An experimental verification of this model was done by [84] that shows a distinctive effect of the displacement of the ODT with respect to the MOT. In their experiment a Ti:saphire-laser was used at a wavlength of 837nm with a waist of 12μm and optimal diplacements of up to 15mm where found. Hence the expected effect for an ODT at a wavelength of 1064nm and a waist of approximately 30μ, hence a Ryleigh lenght of 2mm, as in our experiment, will not be crucial.

6.2 Optical dipole trap with a 1064nm fiber laser

In the following sections we will focus on the characterisation of the dipole traps, our loading scheme and will discuss the evaporation to reach quantum degeneracy.

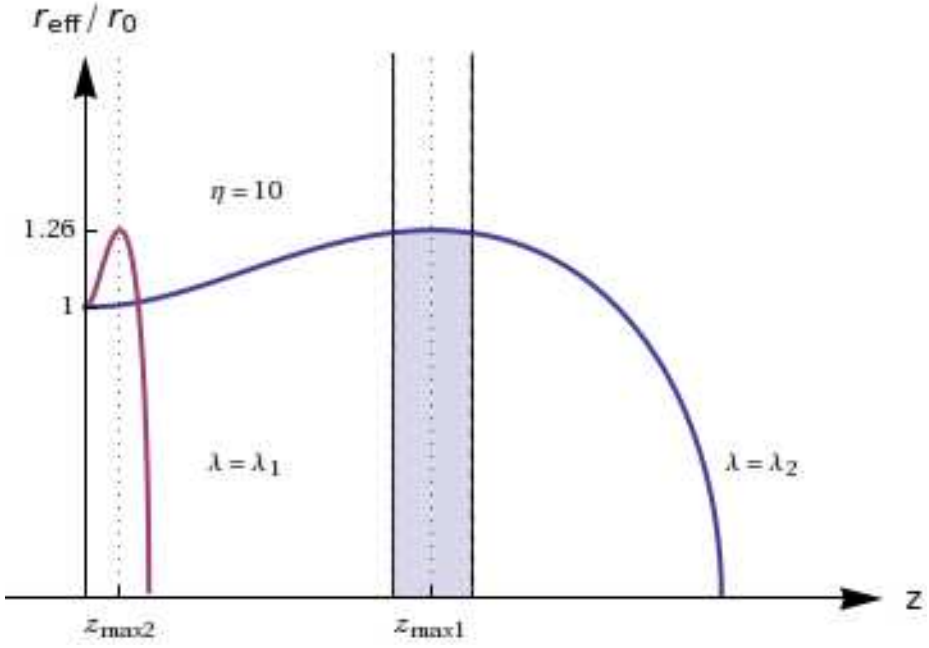

Figure 6.3: The solid lines show the equipotential lines of two dipole trap at a wavelength of $\lambda_1 = 10\mu$m (violet) and $\lambda_2 = 1.064\mu$m (blue), where the ratio of the kinetic energy of the atoms and the trap depth is $\eta = 10$. The size of the MOT (to scale) is shown by the shaded area. By approximating the overlapped volume of the MOT and an optical dipole trap by $V = \pi D r^2$, where D is the diameter of the MOT and r the radius from the axis of propagation to an equipotential line, the volume can be increased by displacing the focus of the optical dipole trap with respect to the centre of the MOT.

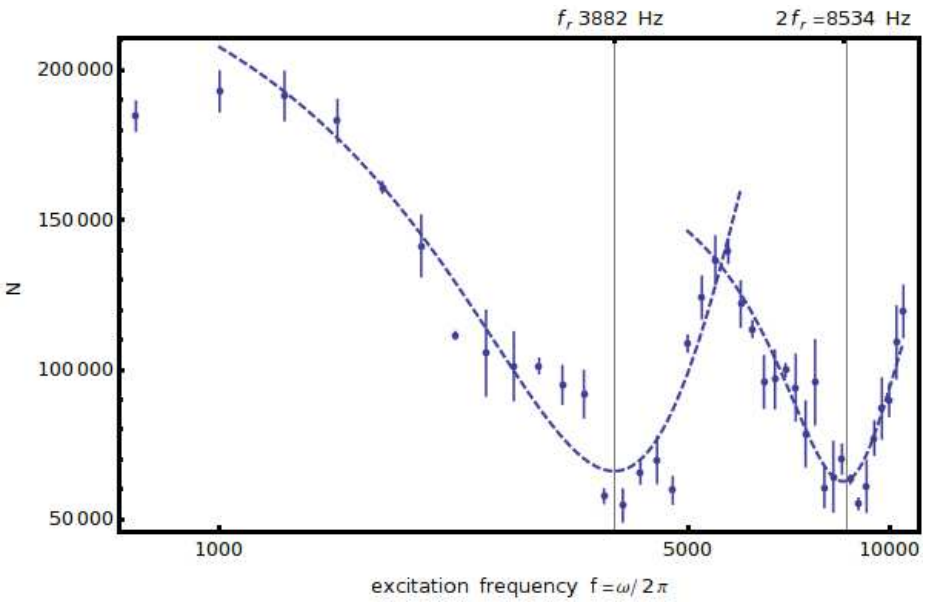

Figure 6.4: Excitation spectrum of ODT1 at 12.6W and Lorentzian fits. The resonance positions are at $\omega_r/2\pi = f = 3882 \pm 79$Hz and $2\omega_r/2\pi = 2f = 8534 \pm 89$Hz. Again we find from this a waist of 28μm.

6.2.1 Parametric heating of the optical dipole trap

We discussed in an earlier section (section 3.3.6) the dynamics of the parametric excitation. The two beams in our setup have a diameter of 5mm and are focused by a f=200mm lens. The expected waist at the focus therefore is $\sim 30\mu$m. The excitation spectrum of trap ODT1 at a power of 12.6W over a range from 750 Hz to 10.5 KhZ shows two significant resonances at $\omega_r \sim 3.9$kHz and $2\omega_r \sim 8.2$kHz (see figure 6.4). Substituting these positions into equation (3.26) we calculate a waist of $w_1 \sim 28\mu m$ for ODT1 and of $36.0 \pm 0.6\mu m$ for ODT2 within reasonable agreement of the design (see 4.5). We also repeated this measurement at a different power of 7.31W (see figure 6.5) to confirm our previous result of the waist. Again by substituting the power and resonance positions into (3.26) we determine a waist of 28μm.

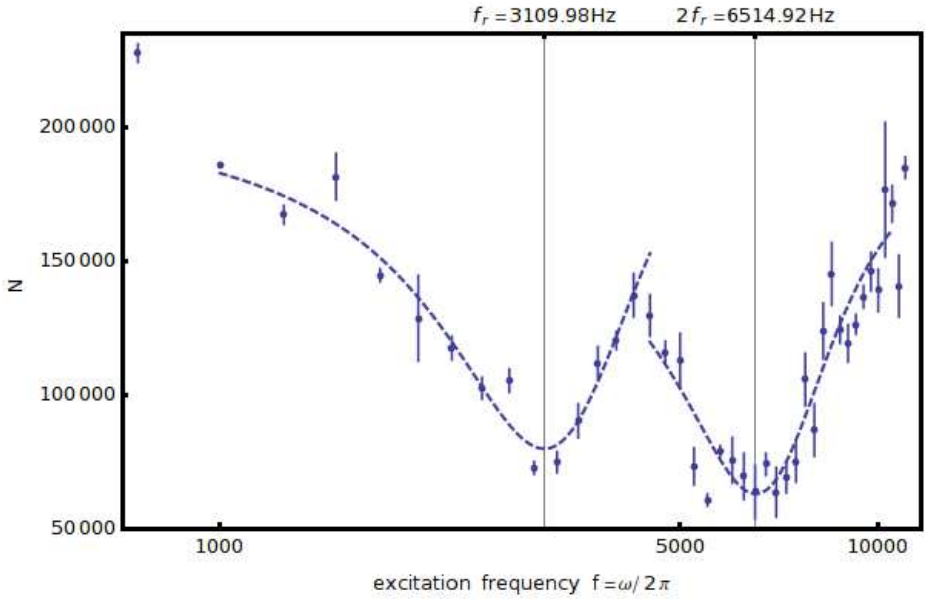

Figure 6.5: Excitation spectrum of ODT1 at 7.31W and Lorentzian fits. The resonance positions are at $\omega_r/2\pi = f = 3109 \pm 55$Hz and $2\omega_r/2\pi = 2f = 6514 \pm 10$Hz. This corresponds to a waist of 28μm.

6.2.2 Collision rates and loss mechanisms

The life time of a trap is determined by the number of atoms remaining in the trap after different holding times in a constant trap. In a simple model [62]

$$\frac{dN}{dt} = -\alpha N - \beta N^2 - \gamma N^3 \tag{6.2}$$

where α is an exponential loss rate caused by collisions with the hotter background gas and heating mechanisms, β a loss coefficient among inelastic collisions of two atoms and the γ the inelastic collision of three atoms.

Elastic two-body collisions The rate of the evaporation depends on the number of atoms N in the trap, the ratio $\eta = U_0/k_\mathrm{B}\ T$ of thermal energy of the atoms $k_\mathrm{B}\ T$ and the depth of the trap U_0 the trap an the elastic collision rate $\gamma_e l$ and the rate of evaporation is given by

$$\dot{N} = -N\beta_{el}\eta e^{-\eta} \tag{6.3}$$

where the elastic collision rate β_{el} is given by

$$\beta_{el} = N \left(8\sqrt{2} \frac{a^2 \, m}{\pi k_{\mathrm{B}}} \right) \frac{\bar{\omega}^3}{T} \tag{6.4}$$

where

- a is the s-wave scattering length
- m is the mass of the atomic
- $\bar{\omega} = (\omega_x \omega_y \omega_z)^{1/3}$ is the mean trapping frequency

three-body collisions The three body collision rate is proportional to the three body loss coefficient Γ_3 [85], the effective volume $V_{\mathrm{eff}} = (2\pi k_{\mathrm{B}} T/m)^{3/2} (1/\bar{\omega})^3$ of the trap and density n_0 of the atoms in the trap and is given by

$$\gamma = \Gamma_3 \, V_{eff} \, n_0 \tag{6.5}$$

6.3 Evaporating

A simplified schematic overview of the entire procedure from loading thermal atoms into a MOT and the evaporation to a BEC in our ODT showing the intensity detunings and the strength of the magnetic field is given in figure 6.6. The three stages of the procedure are

1. loading the MOT and transfer into initial single beam trap
    - loading the MOT compression in a CMOT
    - transfer into initial single beam trap
2. evaporation
    - initial evaporation in a single beam trap
    - compression into a crossed trap
    - final evaporation in the crossed trap
3. imaging after time of flight

which will be described in more detail in the following paragraphs.

Loading the MOT and transfer into initial single beam trap

We load our MOT for 13 seconds while one of our dipole trpas is at maximum power. After loading the MOT we slightly increase over a few tens of milliseconds the magnetic gradient to compress the atomic sample in order to increase the density. Further cooling and increase of the density is achieved by the technique of a short temporal dark MOT where the detuning of the trapping beams of the MOT is increased to $\Delta = -143\text{MHz}$ with respect to the $|F = 2\rangle \rightarrow |F = 3\rangle$ transition and the intensity of the rempumper is lowered to $\sim 40\mu W/cm^2$. Upon extinguishing the repumper and turning off the magnetic field we apply molasses cooling for a duration of 1 ms. The

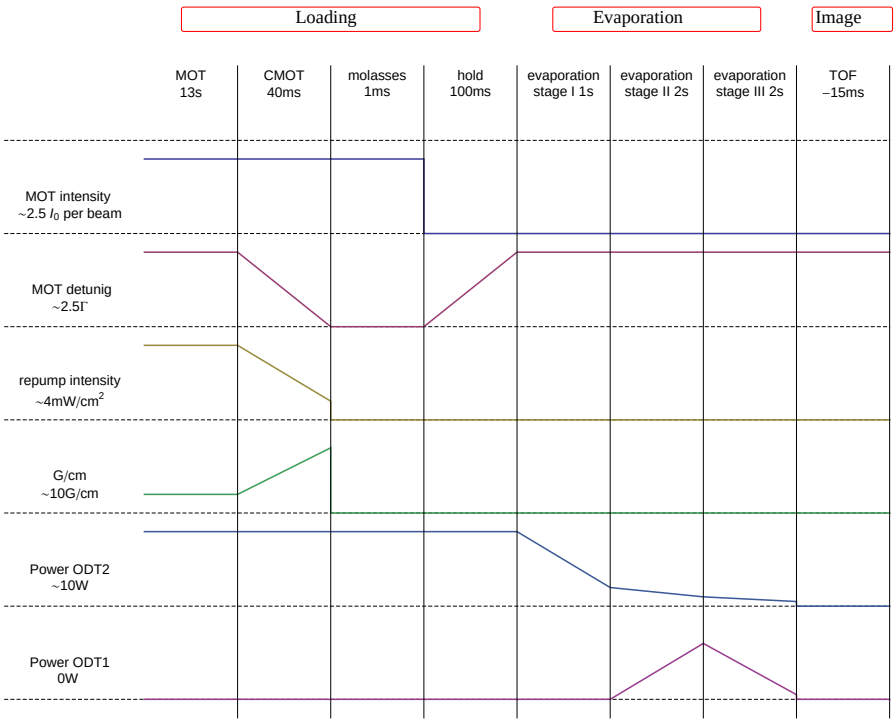

Figure 6.6: Schematic of the loading and evaporation sequence .

initial number of atoms in the optical dipole will improve with higher densities and higher number of atoms after the compression of the MOT and the temporal dark MOT. The initial number of atoms in our dipole trap as we vary the detuning of the MOT beams and the power of the repumper is shown in figure 6.7. We detect up to (5.0 ± 0.5) million ^{87}Rb atoms after holding the atoms for 100ms in the dipole trap and after turning off all MOT beams (see figure 6.6).

Evaporation

In order characterise the evaporation we measured the lifetime of the atoms in trap at the end of each step of the evaporation. In figure 6.8 is the decay of the number of for these different steps shown. The initial evaporation in broken up into three sections before the compression in the crossed trap and final evaporation towards quantum degeneracy. At each of these steps we hold the atoms in the trap over a increasing

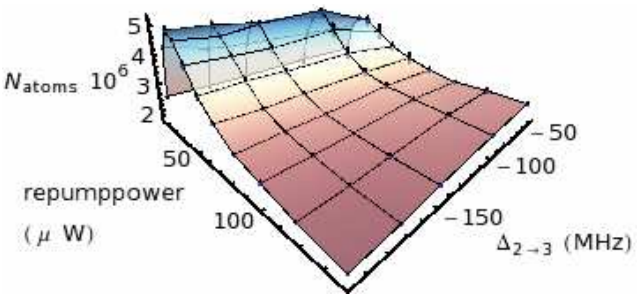

Figure 6.7: The number of atoms in the initial trap as a function of the power of the repumper and the detuning during the temporal dark MOT. The number of atoms maximises at a power of 40μW in the repump beam for all detunings the MOT trapping beam.

time at final power of each step. The life time of the of trap is determined by a rapid loss of atoms followed by a slower decay determined by collisions with the hot background gas. Fitting our data to this model given in (3.37) works poorly and we assume that other loss mechanisms have to be taken into account such as the light scattering taking other energy levels into account other than those from the D1 and D2 line. The line width of the used laser is 2 nm and possibly there is a coupling between states via a virtual states [86]. Estimating the $1/e$ life time of each step (see figure (see 6.10(a)) we see that first the life time increasing from 6s up to 11s. During the compression of the atoms in the crossed trap the three body loss rate increases significantly (see figure 6.10(b)) and hence the life time decreases. During the final evaporation the three body loss rate decreases and the life time is recovering to 6s. Throughout the evaporation the elastic collision rate remains high such the remaining atoms rethermalise fast (see figure 6.11).

The evaporation is described in section 6.3. With the decay of the number of atoms in the trap energy is removed from the system and lowers the temperature (see figure 6.8) of the remaining atoms and increasing the phase space density until the too few atoms remain in the trap to maintain a high collision rate. Therefore the decay of the temperature stagnates and the phase space density decreases (see figure 6.8) as atoms are lost but no longer remove energy from the system.

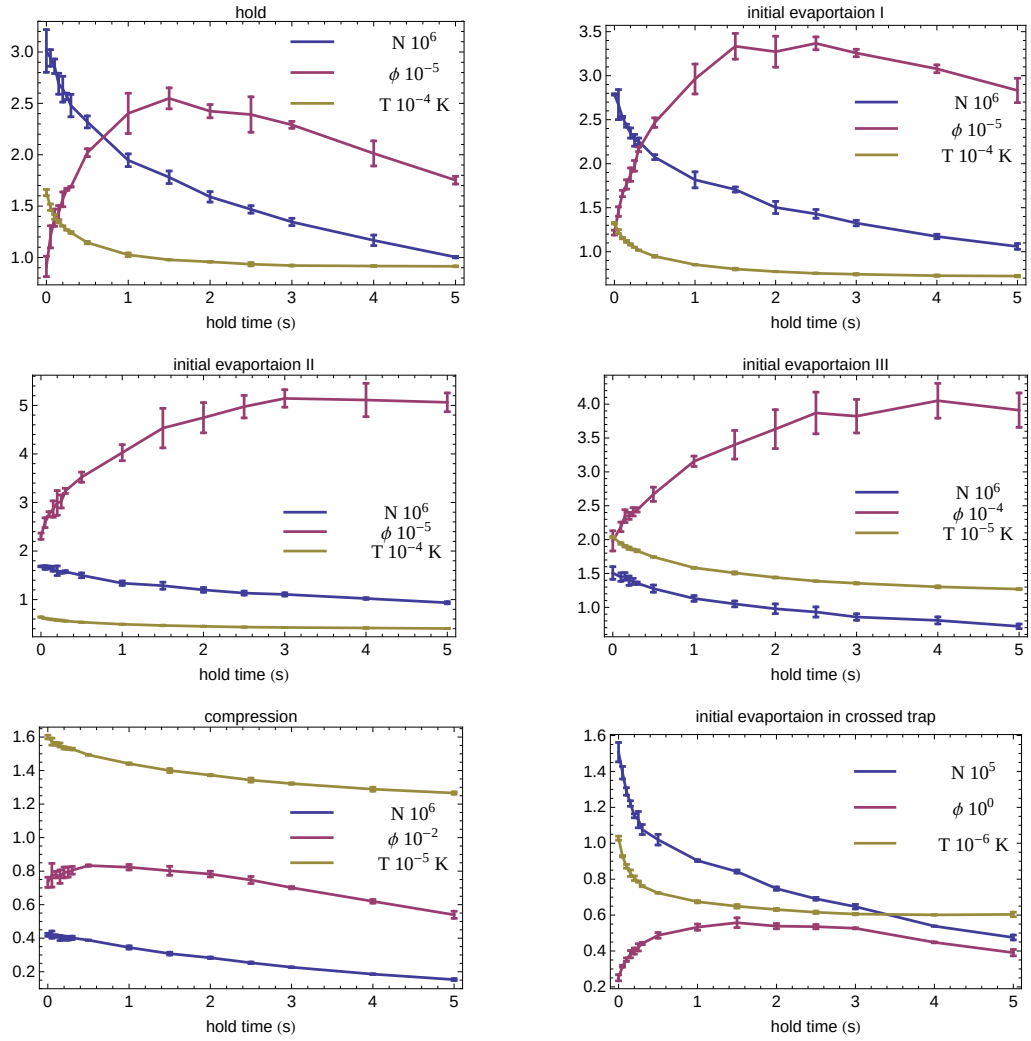

Figure 6.8: Characterisation of the evaporation. In each plot is shown the number of atoms N, the phase space density ϕ and the temperature T of the atoms in the trap as a function of the hold time along the stages of the evaporation.

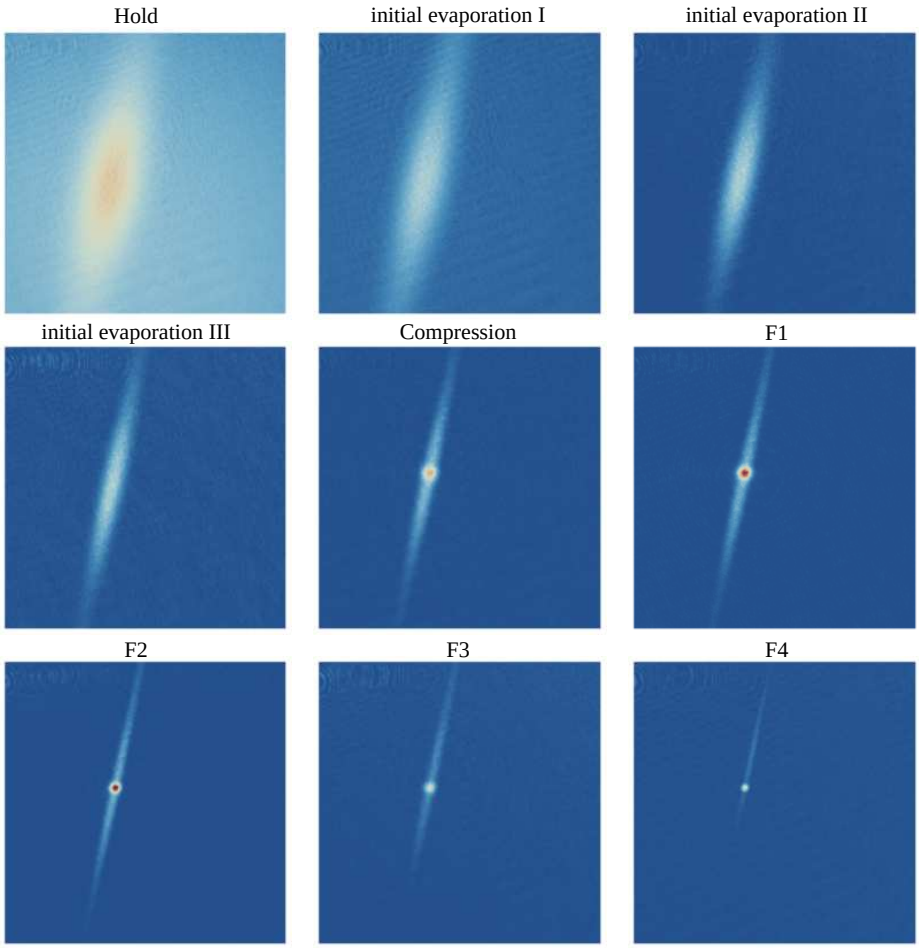

Figure 6.9: Absorption images at the end of each section of the evaporation scheme see text and figure 6.6.

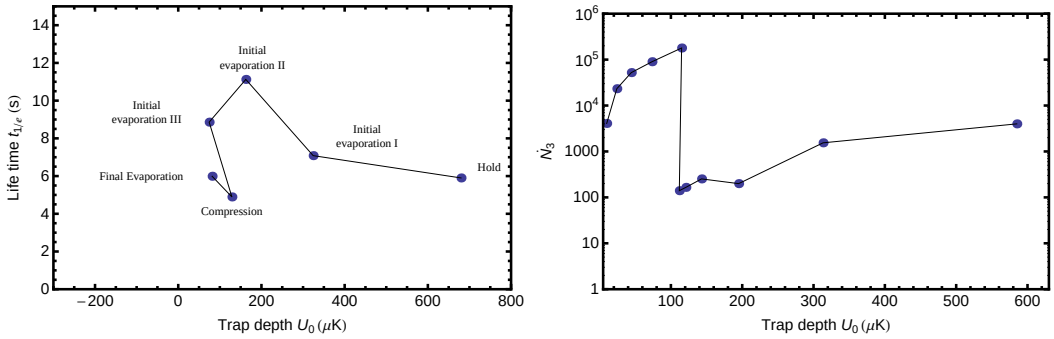

(a) $1/e$ lifetime. (b) Three body loss rate.

Figure 6.10: $1/e$ life time 6.10(a) and three body loss 6.10(b) rate of the trap during the evaporation: The sudden rise of the three-body loss rate is caused by the compression of the atoms in the crossed trap. The lines are a guide to the eye not data.

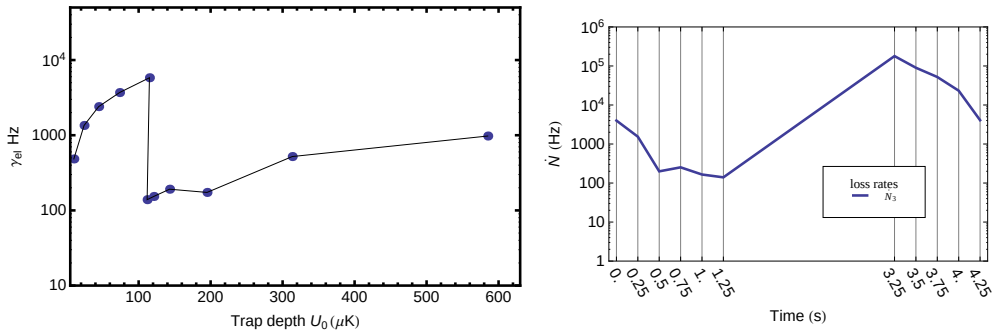

(a) Elastic two-body collision rate. (b) Three-body loss rate.

Figure 6.11: Elastic two-body collision rate 6.11(a) and three-body loss rate 6.11(b) during the evaporation: The sudden rise of the three-body loss rate is caused by the compression of the atoms in the crossed trap. The lines are a guide to the eye not data.

Overall we decrease the temperature from 160μK to 1μK and increase the phase space density by a factor $3{\cdot}10^4$ from 10^{-5} in the initial trap to 0.3 until we start to evaporate into the quantum degenerate regime.

6.3.1 Linear ramps at the final evaporation

After the compression into the crossed we kept evaporating with linear ramps halving the power from step to step varying the time of each section. These are the sections *F1, F2, F3, F4*. In figure 6.9 are the absorption images shown at the end of each section scaled to the same colour scale. The temporal change of the trap depth U_0 and mean frequency $\bar{f} = \bar{\omega}/2\pi$ of this sequence is shown in figure 6.12(a) and 6.12(b) respectively. For this sequential approach the number of atoms, the mean temperature and phase space density of the atomic sample are shown in the graphs of figure 6.13, where the data was taken at the end of each step and uncertainties are given in one standard deviation of the measured quantity. Using these ramps the phase space density increases constantly but towards the end of the last ramps very few atoms are left. Nonetheless the first onset of Bose Einstein condensation was observed with this approach (see figure 6.14) as the measured temperature was below the theoretical critical temperature. At this stage we were able to trap up to 40.000 atoms at a calculated $T/T_c \sim 0.5 - 0.6$ yet the observed condensate fraction was less than 5%. Although we saw a bimodal distributions (white circles in figure 6.14) we were not able to fit a bimodal distribution to extract further quantities. We believe the fragmentation of the BEC to arise from magnetic stray fields separating the hyperfine states or to be caused by impurities of the polarisation of the trapping beams causing a lattice like trap. Purification of the BEC could not be achieved as further reduction of the trapping potential resulted in the loss of the whole cloud. To make sure that the polarisation of the two traps are linear and orthogonal we put polarising beam splitters into the beam line of each trap before the beams are focused into the chamber. By comparison of our data to the data of a similar apparatus in

M.D. Barretts group in Singapore [87] we came to the conclusion that our evaporation scheme after the compression in the crossed dipole trap is not efficient. One reason could be a high three-body loss rate which becomes significant at densities higher than 10^{14}cm^{-3}. We therefore tried another scheme to evaporate faster and more efficiently which we will discuss in the next section.

6.3.2 Exponential ramps at the final evaporation

Another and faster approach was to replace the linear ramps after the compression with exponential ramps given by $f(t) = A\ e^{-t/\tau} + B$, where the constants A and B are to be determined by the initial and final power of the ramp. Figure 6.15(a) and 6.15(b) show again the evolution of the trap depth and mean frequency of the trap. The first steps until the compression in the crossed trap remain the same but the two final steps evolve exponentially in time. Comparing figure (6.13) and figure (6.16) we see that after the compression the phase space density grows faster and higher than before using the linear ramps. After the first step of the final evaporation we now achieve a higher phase space density in a shorter time and have sufficient number of atoms left. During the final evaporation the cloud undergoes the phase transition and condenses partially into a BEC (see figure 6.17) containing different spin states as we will see later. In figure 6.17(a) is shown the averaged optical density of 15 sequential shots to reduce noise caused by fringes. The bimodal distribution becomes more obvious to see if we integrate the two dimensional absorption profile along one direction and fit the one dimensional density distribution

$$n(x) = n_{th}\ \exp\left[-\frac{-x^2}{\sigma^2}\right] + n_c\ \max\left[0, 1 - \frac{x^2}{r_c^2}\right]^2 \tag{6.6}$$

From those fits we determine approximately 16500 atoms in the condensed fraction and nearly 5500 atoms in the thermal fraction resulting in a approximately 26% condensate fraction.

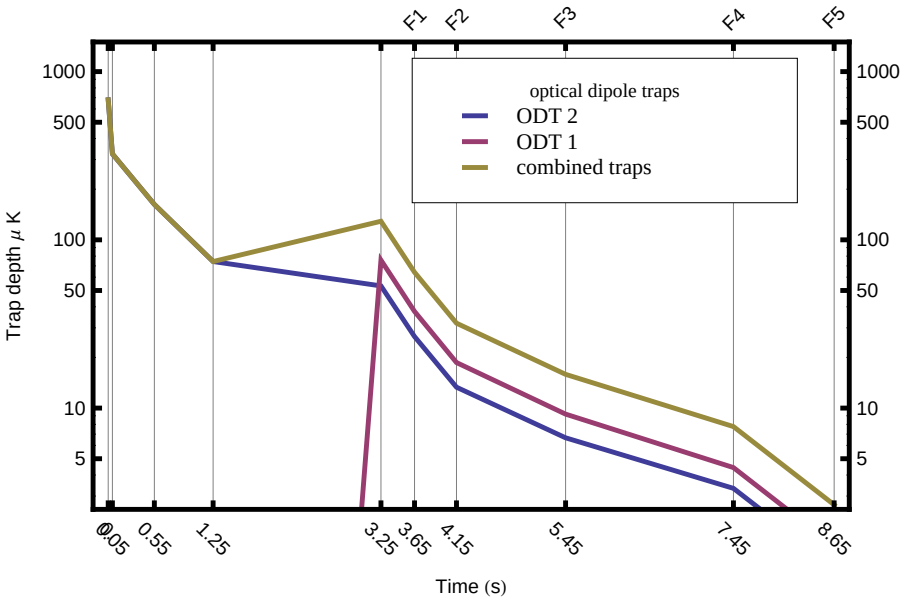

(a) Trap depth U_0 during the evaporation. Please not the logarithmic scale of the trap depth. At 1.25 s we begin to increase the power of ODT1 over 2s to approximately the same trap depth of ODT2.

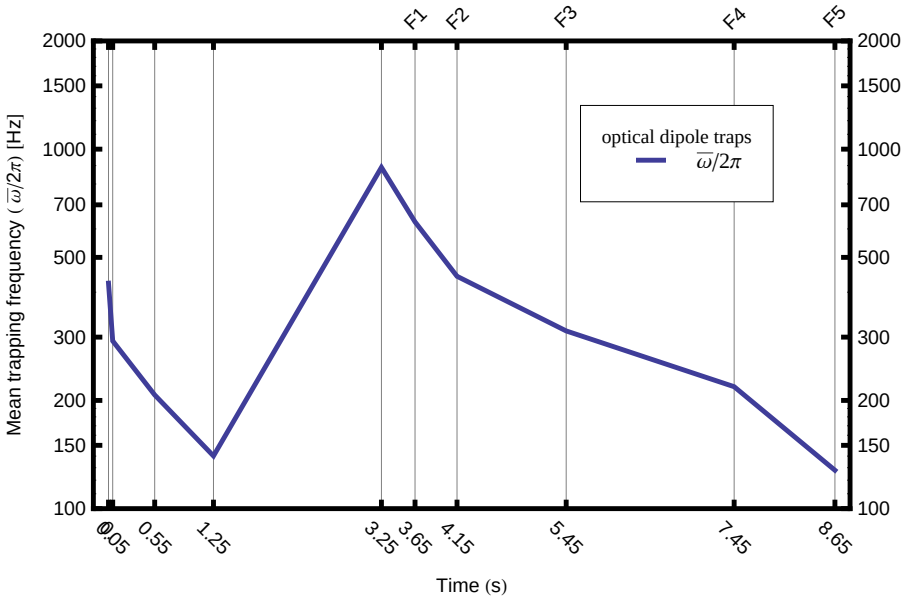

(b) Mean trapping frequency $\bar{f} = \bar{\omega}/2\pi$ during the evaporation.

Figure 6.12: Trap depth U_0 and mean frequency $\bar{f} = \bar{\omega}/2\pi$ during the evaporation

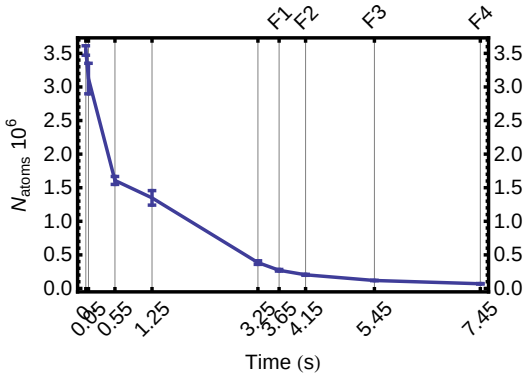

(a) Number of atoms N.

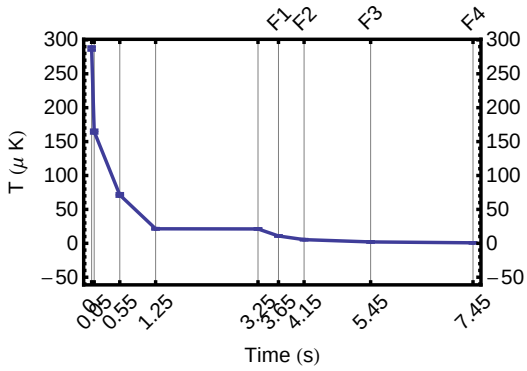

(b) Temperature T.

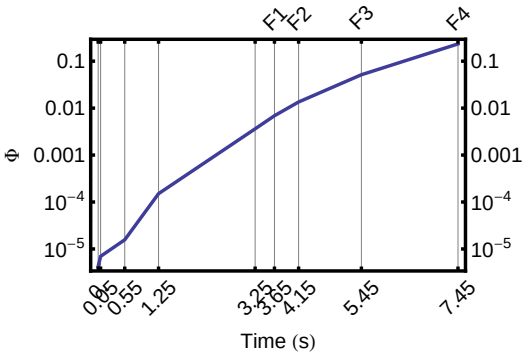

(c) Phase space density Φ.

Figure 6.13: The number of atoms N, the temperature T and phase space density Φ during the evaporation with linear ramps. We see an increase of the phase space density throughout the sequence but trap too few atoms at the very end of the sequence.

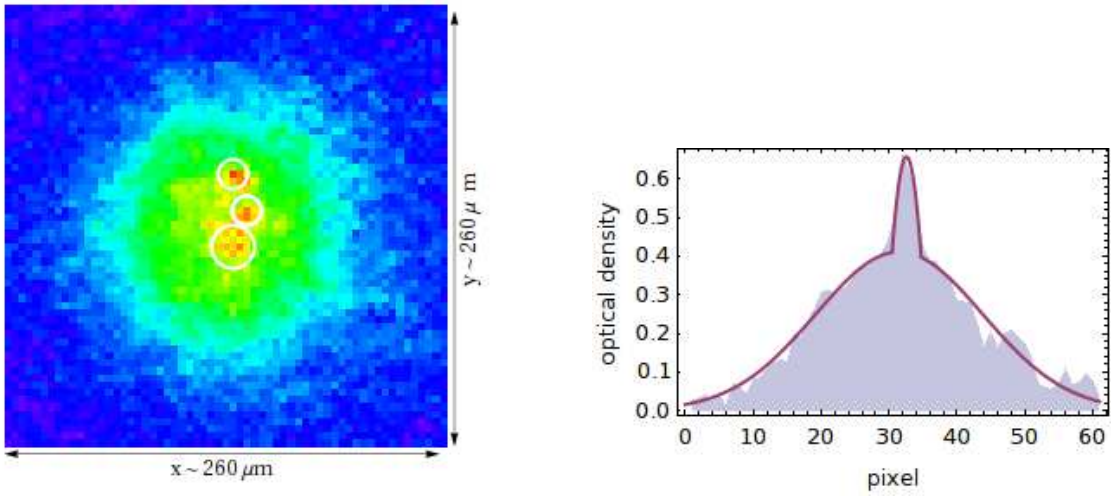

(a) An absorption image on the onset of Bose-Einstein condensation.

(b) Cross section through the strongest peak of the absorption image on the left.

Figure 6.14: On the onset of Bose-Einstein condensation we can identify a fragmented structure in the thermal cloud. A cross section through the highest optical density clearly shows a bimodal distribution as one would expect.

6.4 Distribution of the $m_F = 0, \pm 1$ states

In chapter 2 we described a model of a single component Bose-Einstein condensate. Since the optical dipole trap is not spin selective and the trapped atoms occupy the F=1 manifold with $m_F = 0, \pm 1$ and it is possible that they form in the condensed phase a so-called spinor condensates [88, 89, 90]. Spinor condensates are described by a vector order parameter $\Psi\chi$, where χ is a vector with $2F+1$ components describing the individual spins. The two-body interaction is then given by $U(r) = \delta(r)(c_0 + c_2\mathbf{F_1} \cdot \mathbf{F_2})$, where r is the interatomic distance and c_2 the spin dependent interaction parameter. The interaction is ferromagnetic for $c_2 < 0$ and antiferromagnetic for $c_2 > 0$. Calculations of the ground state of the F=1 spinor condensate have been done by [88, 91] in the absence of magnetic fields and by [92] in the presence of a magnetic field. For the thermodynamics of the Bose-Einstein condensation of a spin-1 system not only the total number of atoms $N = N_- + N_0 + N_+$ is conserved but the

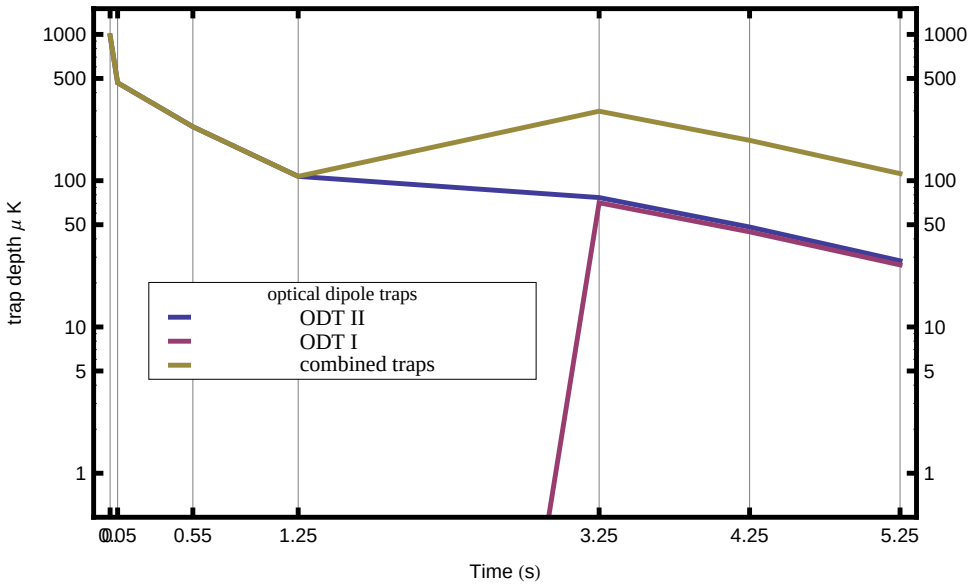

(a) Trap depth U_0 during the evaporation. Please not the logarithmic scale of the trap depth. At 1.25 s we begin to increase the power of ODT1 over 2s to approximately the same trap depth of ODT2.

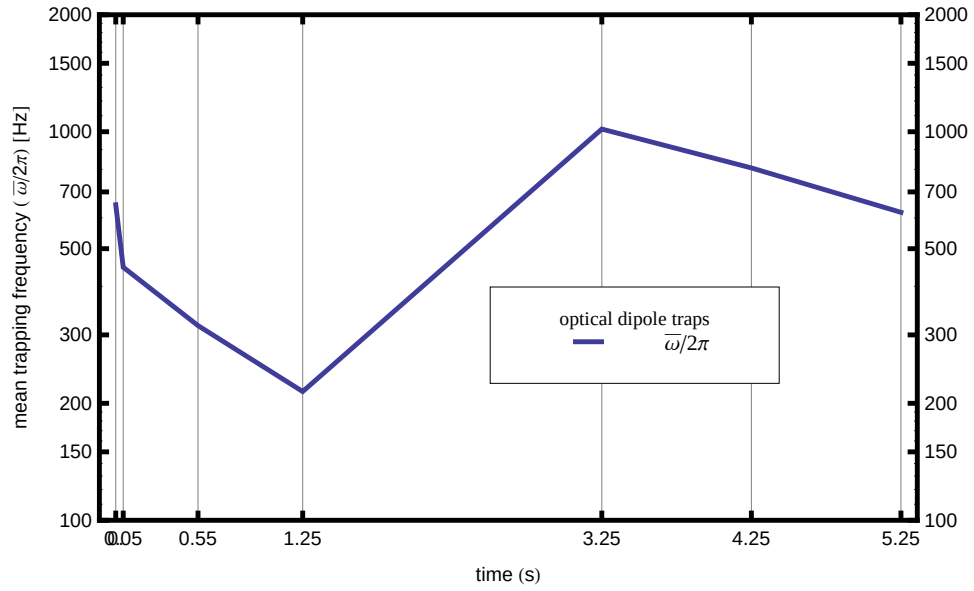

(b) Mean frequency $\bar{f} = \bar{\omega}/2\pi$.

Figure 6.15: Trap Depth U_0 and mean frequency $\bar{f} = \bar{\omega}/2\pi$ of a faster ramp with exponential ramps after the compression.

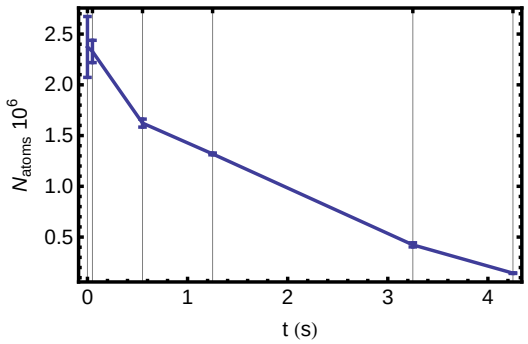

(a) Number of atoms N.

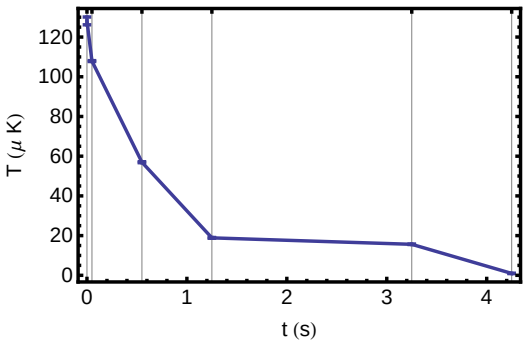

(b) Temperature T.

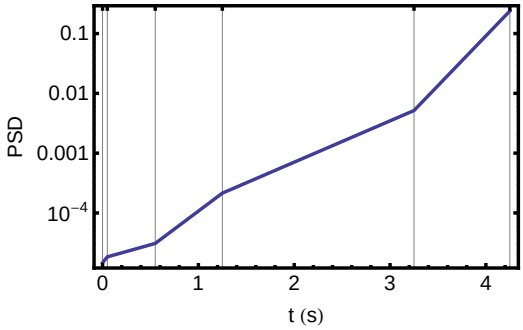

(c) Phase space density Φ.

Figure 6.16: The number of atoms N, the temperature T, and phase space density Φ during the evaporation using exponential ramps of the power after the compression.

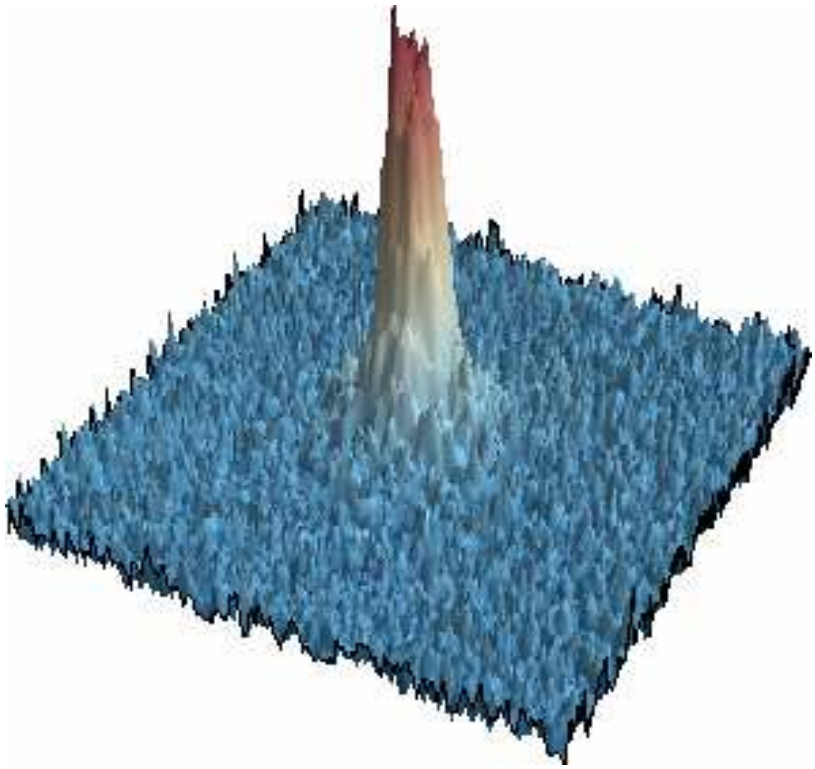

(a) Three dimensional representation of the optical density.

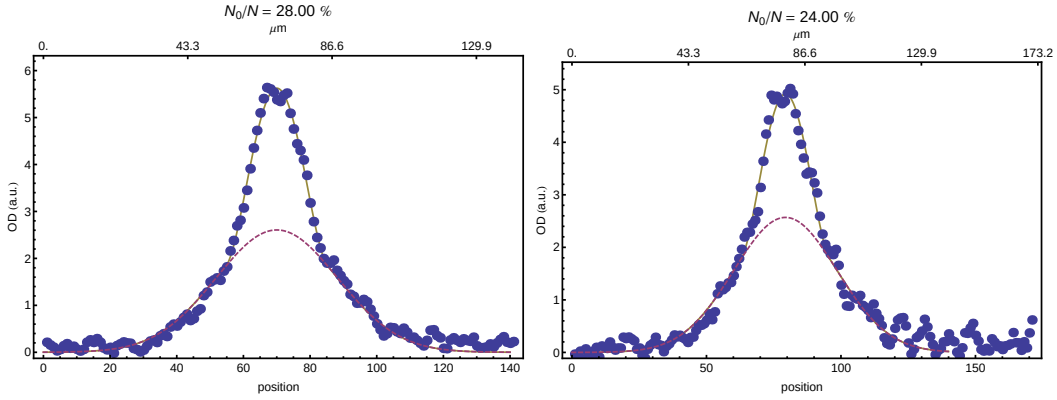

(b) Density profile of the integrated optical density along the x-direction

(c) Density profile of the integrated optical density along the y-direction

Figure 6.17: Two dimensional absorption image of an all-optical BEC and one-dimensional density profiles of the integrated two-dimensional image along either direction where the bimodal distribution can be seen.

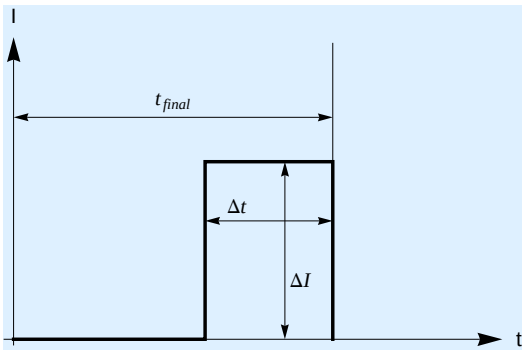

Figure 6.18: Variation of the applied magnetic field strength in time during the last step of the evaporation.

magnetisation $M = N_+ + N_-$ as well [93]. This leads to different chemical potentials as well and the condensation of the three m_F can occur at different temperatures. During evaporation we do not actively prepare a particular spin state. In a Stern Gerlach like experiment (see figure 6.19), where we apply a magnetic gradient field during the time of flight we can spatially separate the m_F substates as they are accelerated due to their magnetic moment. The magnetic force on atom is given by $F = \nabla(\mathbf{m} \cdot \mathbf{B})$. Therefore atoms in the state $m_F = 0$ are not accelerated whereas atoms occupying the states $m_F = -1$ and $m_F = +1$ are accelerated in opposite directions Following our standard procedure we find that most atoms are condensed into the $m_F = -1$ state. Applying a magnetic gradient field purifies the spin state into the $m_F = 0$ state [94]. Similar to the work by Chang we applied a magnetic gradient field of different strengths for different times (see figure 6.18) during the final evaporation. For different times and strengths of the field the condensation is occurs preferentially into one of the substates as shown in figure 6.20. Since no more atoms are added to the trap during the evaporation and the population remains constant (see figure 6.21(a)) as it is without applying a magnetic gradient of $\sim 10G/cm$, it means we can transfer almost all atoms into one particular spin state (see figure 6.21(b)). We discovered these dynamics shortly after the first successful formation of a BEC towards the end of the authors time in the laboratory. A similar observation was made by M.D. Barrett of this intriguing behaviour.

The origin of the magnetization produced in our all-optical condensates re-

> *mains to be determined; however we have developed empirical techniques to manipulate the magnetization of the cloud. By applying different magnetic field gradients during the evaporation process, we can significantly alter the spin population (see figure 5).* in [95]

Although this observation was reported in 2002, the author is as yet unaware of any further report in the literature of the underlying dynamics. The relative position of the magnetic and optical trap is unknown and may not overlap well, leading to difficulties in modelling the dynamics in the combined magnetic and optical potential. We here note, however, that it is a useful empirical technique to prepare initial desired spin states in our condensates, and that further study would be of interest.

6.5 Onset and growth of the condensate in the $m_F = 0$ state

In the previous two sections we saw that we can create a Bose Einstein condensate but know that it is a mixed spinor condensate. Also we saw that we are able to prepare a certain pure spin state. So far we have not thought about the condensate fraction of the BEC itself. One would expect that with further evaporation the temperature decreases and a fraction of the trapped atoms undergoes a phase transition and condense into a BEC, the absolute ground state of the trap. We stopped the last step of the evaporation at different points in time which means at different powers and therefore different trap depths and trapping frequencies. Figure 6.22 shows the onset and growth of the BEC at different points in time (labels on top on each smaller figure in units of seconds) of the last evaporation. Just below the critical temperature T_c a small condensate fraction can be seen on a thermal background. As the evaporation continues the condensate fraction becomes larger (see figure 6.23) and almost pure as there is no discernible thermal fraction to be seen. The condensate is elongated along the direction of ODT2 as it is the slightly weaker trap. The optical density

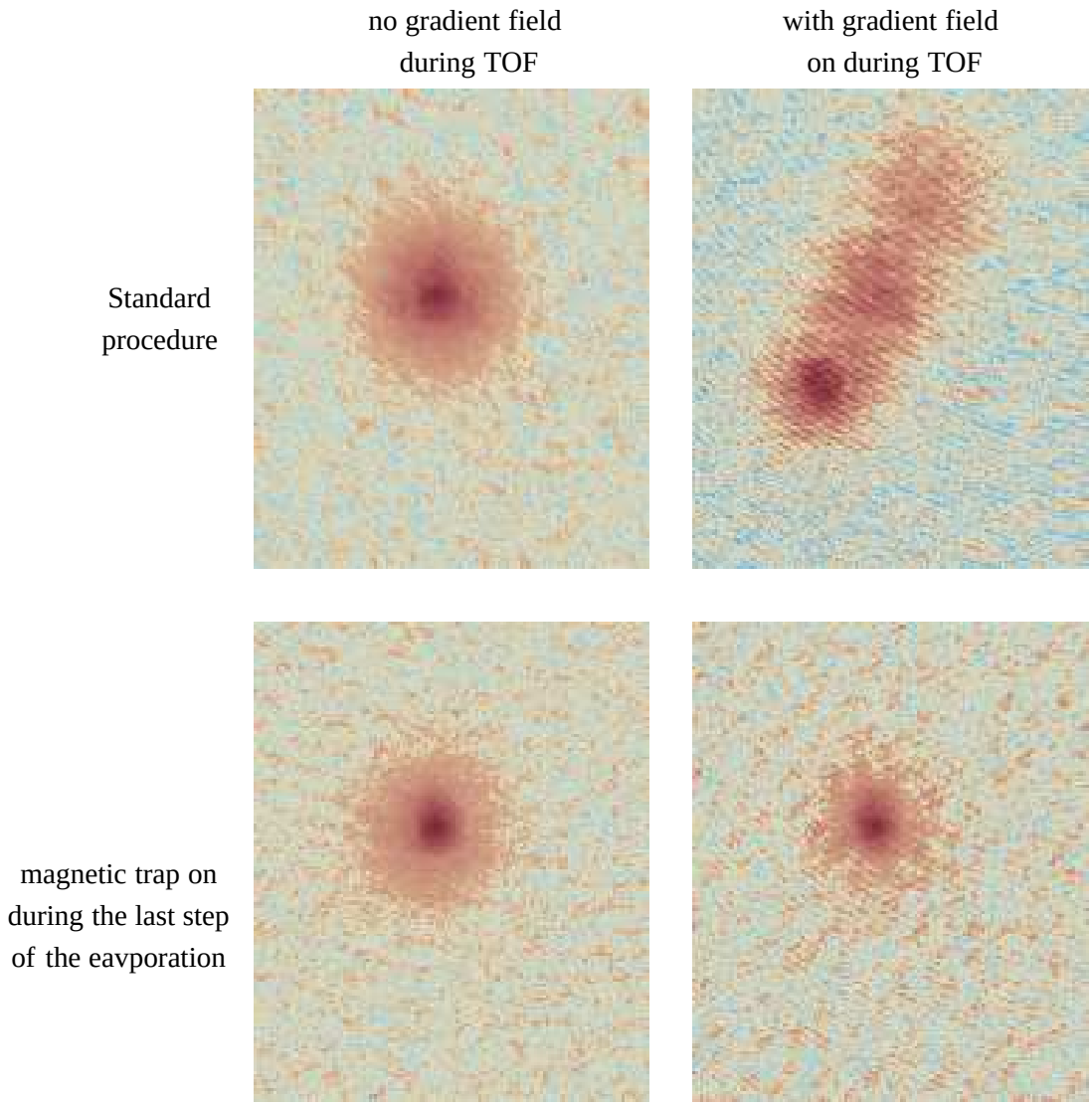

Figure 6.19: A mixed spinor condensate (top left) of the m_F states can be separated in a Stern Gerlach like experiment (top right).The mf =-1 state is condensed, and the onset of condensation can be seen in the mf=0 state. The mf=1 state is still thermal. All atoms condense into the $m_F = 0$ state (bottom left) if a magnetic gradient is applied during the last step of the evaporation as there are no other components left (bottom right)

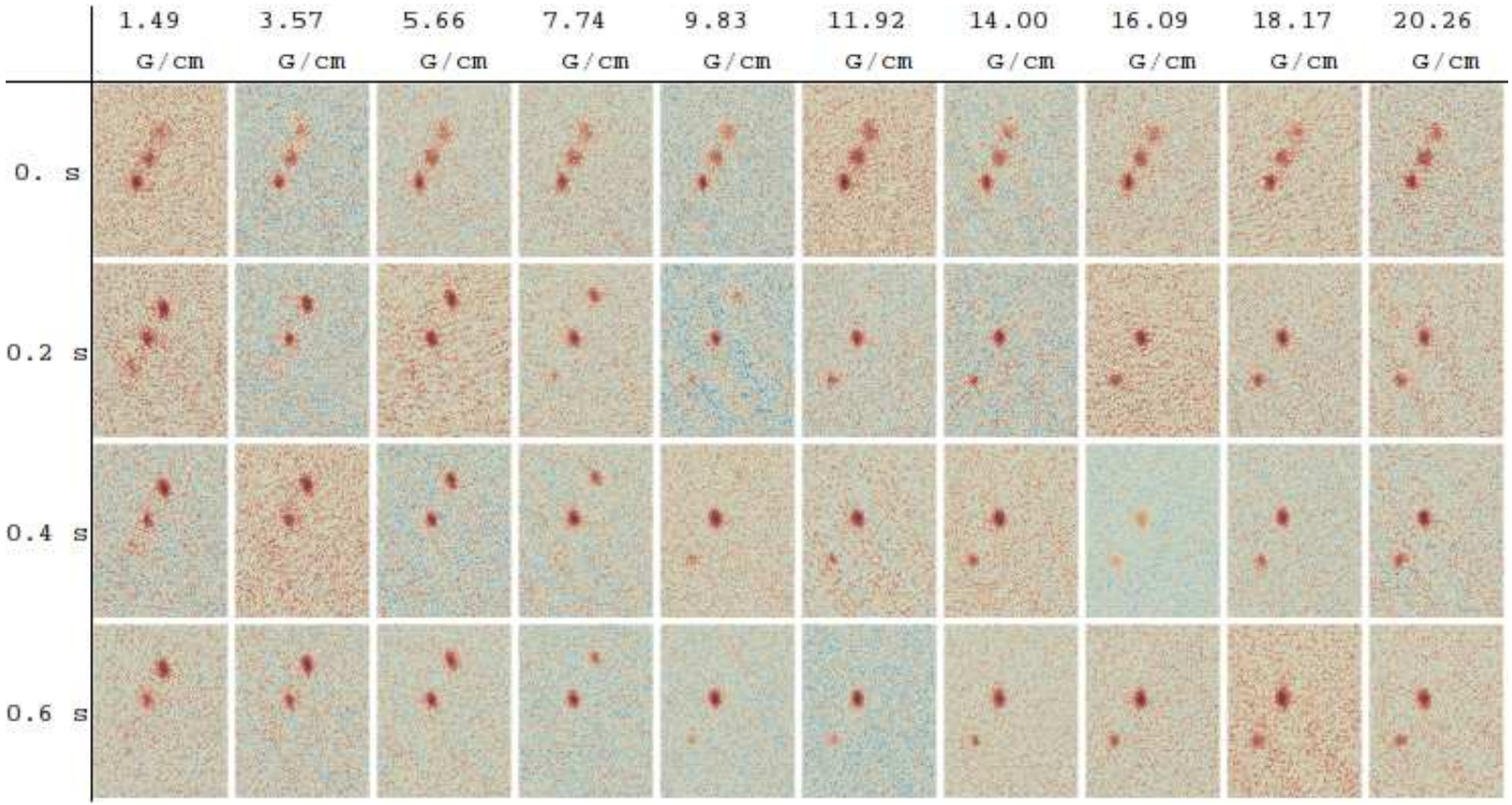

Figure 6.20: By applying a different magnetic gradient field (increasing from top to bottom from 1.49 G/cm to 20.26 G/cm) for different durations (increasing from left to right from 0.1 to 0.9s) during the last step of the evaporation one of three states is preferred for the condensation

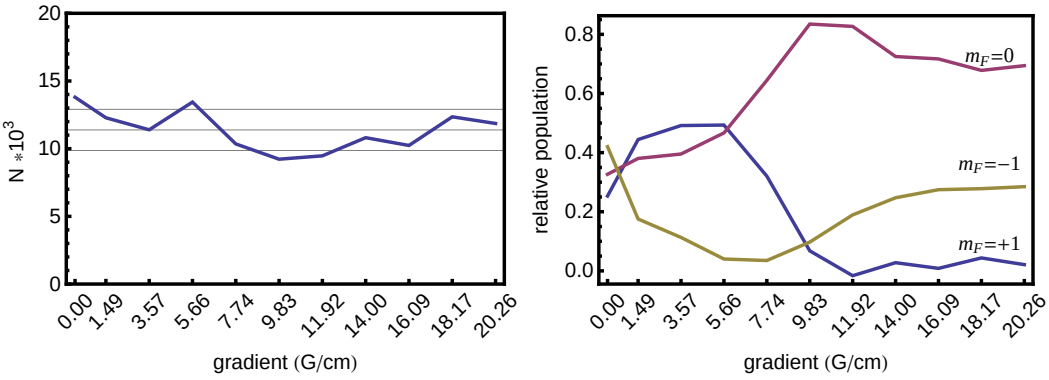

(a) Total number of atoms; grid lines are $\bar{N}$ and within one standard deviation.

(b) Relative population of the m_F states.

Figure 6.21: Total and relative population of the $m_F = \{-1, 0, +1\}$ states.

is integrated along one direction to fit a one dimensional bimodal distribution[1] from which we determine the number of atoms in the thermal and condensed phase. At these low powers the estimation of the temperature is highly sensitive to the actual trap geometry. In these shallow traps we can not neglect the effect of gravity any more 6.25. The effect of gravity alters the mean frequency, shifts the equilibrium position along gravity and the effective trapping potential along gravity is smaller as well. Further we have to consider finite size effects and the weak interaction of the particles. These two corrections are given by

$$\frac{\Delta T_f}{T_{c,0}} = -0.73 \frac{\omega_m}{\bar{\omega}} N^{-1/3} \tag{6.7}$$

for the finite size [96] where $\bar{\omega}$ and ω_m are the arithmetic and geometric means of the trapping frequencies. The correction for the weak interaction [97] is given by

$$\frac{\Delta T_{c,int}}{T_{c,0}} = -1.33 \frac{a_S}{a_{ho}} N^{-1/6} \tag{6.8}$$

where a_S is the s-wave scattering length and a_{ho} the characteristic length $a_{ho} = \sqrt{\hbar/m\omega}$ of the trap is. Thus the critical temperature T_c is lower than $T_{c,0}$ and we

[1] Taking out the integration along two directions of (4.13)

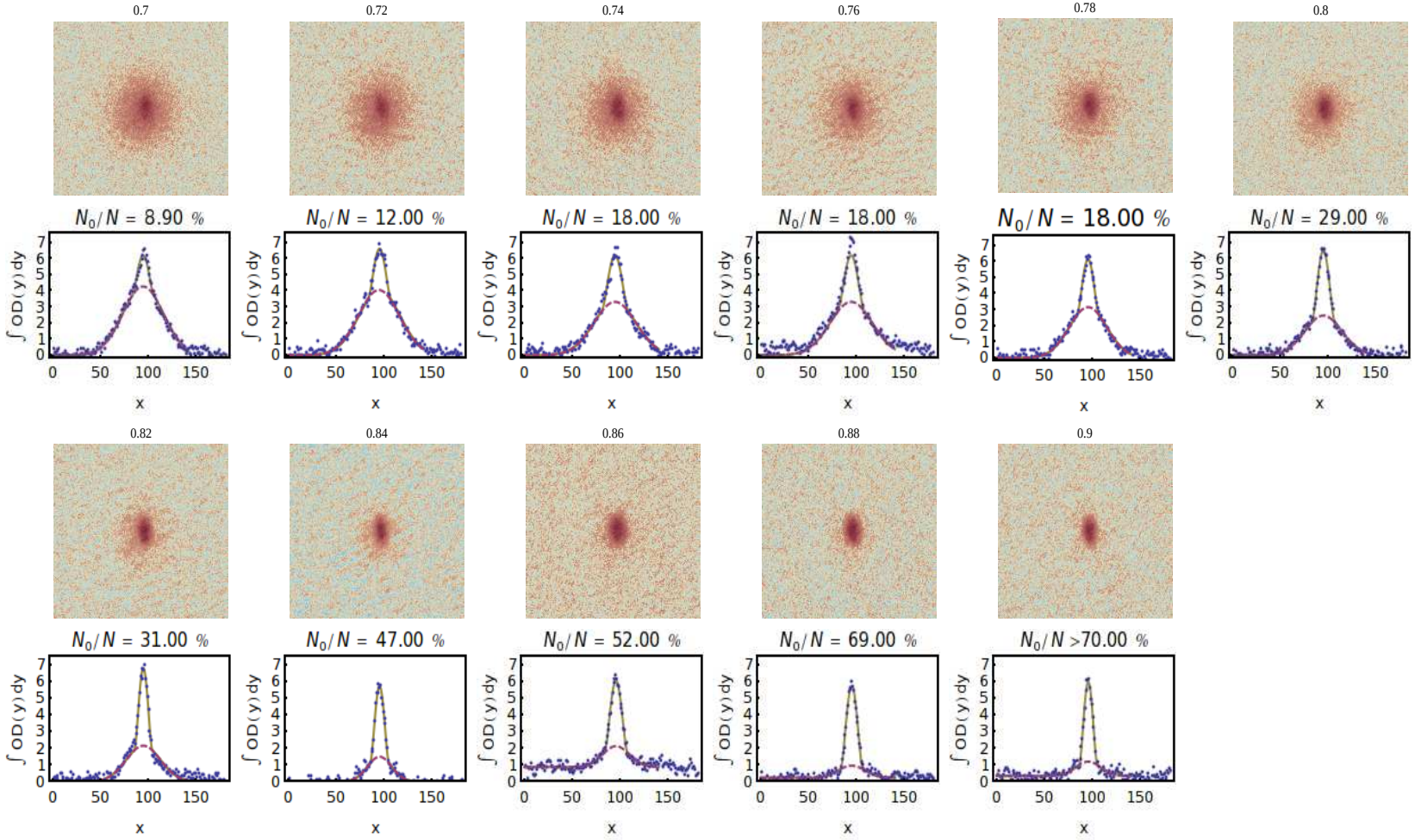

Figure 6.22: Onset and growth of the condensate of the $m_F = 0$ state: On top of each figure is the time in s where the last ramp of the evaporation was truncated. Below the absorption image that shows a spherical thermal cloud an a growing condensate fraction. The condensate is slightly elongated as the one trap is slightly tighter than the other. Below the absorption image are plots containing the data of the integrated optical density in one direction (dots), the bimodal fit (yellow line) and the fitted thermal fraction (red line).

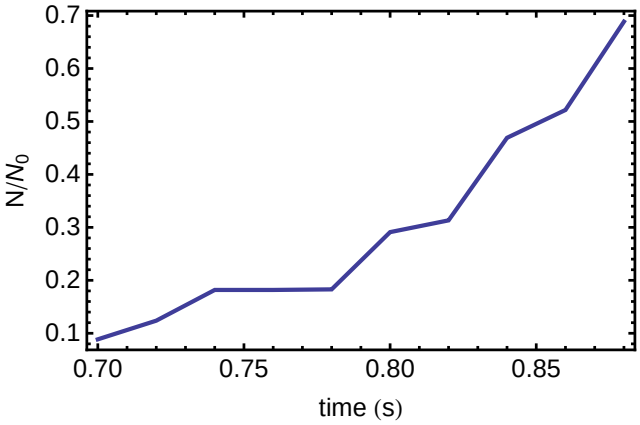

Figure 6.23: The condensate fraction as a function of the time when the last evaporation step was truncated.

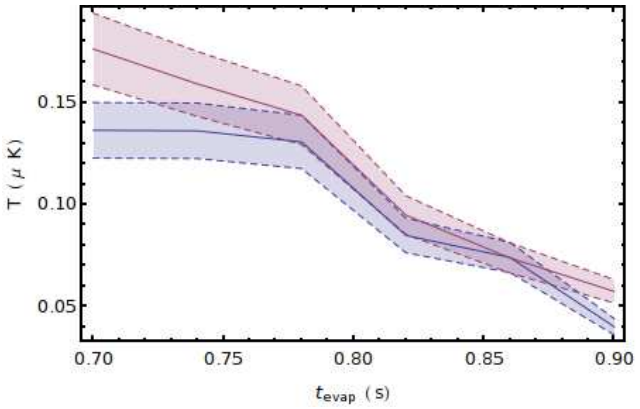

Figure 6.24: Comparison of the calculated temperature based on (4.16) (red)and based on time of flight measurements (4.15) (blue). Shaded areas represent a 10% uncertainty on the temperature

find for the corrected temperatures

$$T_{c,corrected} = T_{c,0} + \Delta T_f + \Delta T_{int} \tag{6.9}$$

where $T_{c,0}$ the critical temperature of 3D harmonic trap is which derived earlier (2.9). The impact of gravity at the end of the evaporation becomes quite significant for the measurement of the trapping frequencies and determining temperatures from the profiles of the atomic cloud. To verify the correctness of the temperature determined by (4.16) we compared the calculate temperature based on the trapping frequencies with time of flight measurements. In figure 6.24 we see that the measured temperature from a time of flight measurement (4.15) agrees very well with the estimated temperature(4.16) from the trap geometry within an uncertainty of 10%. Apart from the uncertainty of the alignment of the trap we found a dependency of the position of the focal point of each traps on the RF-power the AOMs are driven. The shift of

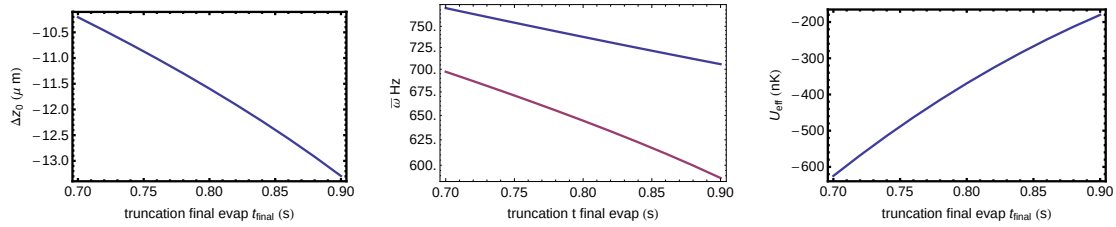

(a) Shift of the equilibrium position along the direction of gravity

(b) Mean trapping frequency with (red) and without (blue) corrections for gravity

(c) Trap depth

Figure 6.25: The effects of gravity on 6.25(a) the trap minima z_0, 6.25(b) trapping frequencies $\bar{\omega}$, and 6.25(c) trap depth U_0. Here the evaporation has been truncated in the final steps from 0.7s to 0.9 s in the final evaporation stage.

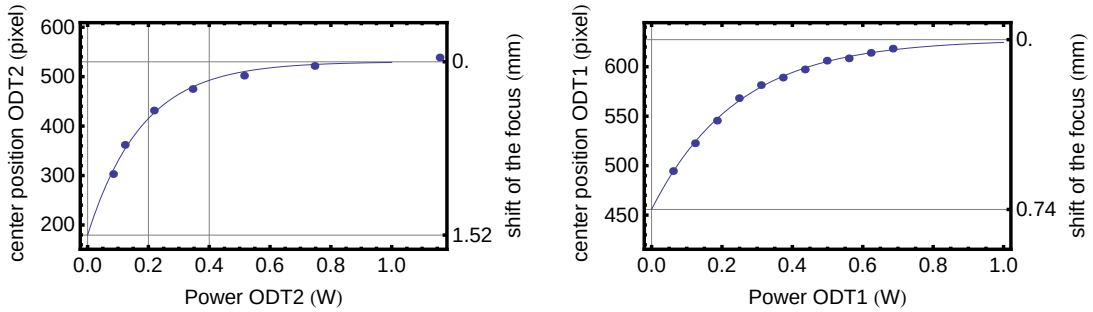

(a) lensing of ODT2

(b) lensing of ODT1

Figure 6.26: The position of the trap changes as power is lowered.

this "lensing effect" [98] for both traps 6.26 is quite significant and can be up to 1mm but is for both traps smaller than the Rayleigh length and hence the trap frequencies will not be effected by much. Although taking all these considerations into account which lowers $T_{c,0}$ by 7% the measured fraction of the condensate does not agree with the expected fraction of the condensate. This surprising result was also observed earlier by [87, 99, 100]. This discrepancy has been thought to be uncertainties in trap frequencies at the end of the evaporation [87], or in problems obtaining consistent condensate fractions from the image fits [100]. It is possible that some deeper devi-

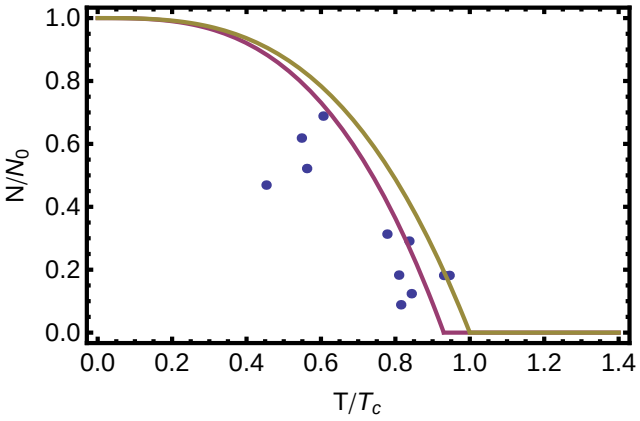

Figure 6.27: The condensate fraction: Ideal, yellow line calculated with (2.10), corrected condensate fraction (red) taking into account the corrections for finite size effects (6.7) and for interactions (6.8) of the critical temperature (2.9) into account and the measured condensate fraction (blue dots).

ation from the harmonic approximation, or underlying loss mechanism is apparent. This might not be surprising, given the relative weakness of the trap in the z direction due to gravity. We hope further work will explore this discrepancy in more detail. J.-P. Matikanien found that the harmonic approximation [101] of shallow traps for Bose-Einstein condensates formed using Gaussian potentials leads to a higher critical temperature [102]. Due to time constraints the verification of the model is beyond the scope of this thesis. In order to perform any experiment on cold atoms the life time needs to be sufficient long which means a life time on the order of a few seconds. In figure 6.28 is the $1/e$ life of our BEC and an exponential fit shown and the decay constant from the fit is (8.6 ± 0.7)s. Therefore we expect to be able to investigate the superfluid properties of a BEC in a toroidal trap [103].

6.6 Summary

Here in the chapter we described the loading of ^{87}Rb and evaporation in an precisely controlled (see section 4.5) optical dipole trap to quantum degeneracy in a dilute atomic gas. We achieved almost pure condensates with up to 20000 atoms in the condensed phase purely in the $m_F = 0$ state by applying a magnetic gradient during

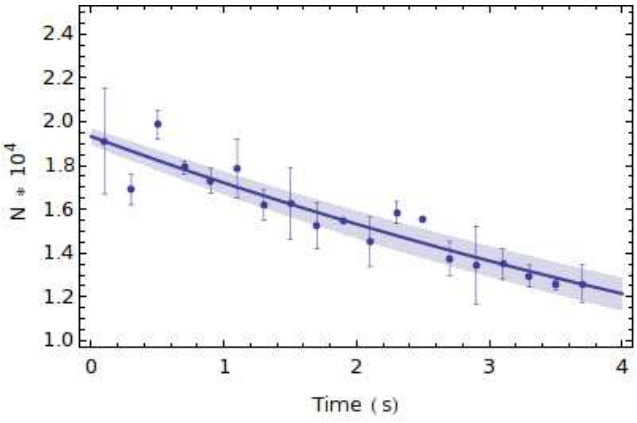

Figure 6.28: $1/e$ life time (dots data, error bars are one standard deviation) of the BEC: the decay constant is (8.6±0.7)s. The shaded area shows the uncertainty of the fit.

the final evaporation. A discrepancy between the expected condensate fraction and measured condensate fraction was observed. Future work will be to optimise the evaporation process further to produce larger condensates, and to explore the nature of the difference in the expected and observed condensate fraction.

7 Towards a scanning dipole trap

In this chapter we discuss the design of a fast scanning laser beam and its applications. The dimension of the confiment of BECs [104] and shape of potentials such as double wells [105] or optical lattices [106] for BECs in atom optics have exhibited interesting phenomena. Optical dipole traps can play a very important role in experiments to apply potentials of various shapes and dimensionality. Often these potentials are combined traps of magnetic fields and optical dipole traps or optical lattices. One problem arising in combined traps is the relative motion of the traps caused by mechanical vibrations. In our experiment we use a trap design that requires only one single beam to apply various potentials or even two-dimensional lattices of a finite number of lattice sites.

7.1 General considerations and design

In optical tweezers experiments commonly 2D AOMs are used to manipulate the position of macroscopic particles. Similar to this technique we use a tightly focused red detuned laser beam to manipulate the potential for neutral atoms in the horizontal plane.

Additional to the frequency shift of a laser beam passing through an AOM the laser beam is also deflected by a small angle which is proportional to the frequency applied to the AOM. Conservation of momentum gives us $k_\mathrm{d} = k_\mathrm{i} \pm k_\mathrm{a}$, where k_d is the wave vector of the deflected beam and k_i and k_a are the wave vectors of the incident beam and the acoustic wave. Within the bandwidth of the AOM the deflection angle

is given by $\Theta = \lambda\nu/v$, where λ is the wavelength of the laser beam and ν and v are the frequency and velocity of the sound wave. For two-dimensional scanning we use two AOMs mounted orthogonally to each other, such the first AOM deflects the beam in one direction and the second one perpendicular to the direction of the first deflection. Now we change the applied frequencies in time and we can write with the double deflected beam any arbitrary pattern [35]. For the dynamic control of a rapidly scanning beam trap, figure 7.1 shows the general concept of the scanning beam trap, a number of technical considerations need to be addressed. To control and stabilise the power of the laser beam we use a noise eater as we discussed in section 4.5. In our experiment we use digital frequency sources to avoid complications arising from the creation of side bands if analogue sources were used. The second channel is controlled with a fast forward loop. Some power of the scanned beam is detected on a photo detector and recorded. The recorded signal is then inverted and combined with the control signal to correct systematic imperfections. In the diffraction limit the smallest possible structure that could be resolved measures 2.2μm for a wavelength of 1064nm. In order to achieve this resolution we designed and optimised a set of lenses that are commercially available. Simulations in Oslo showed that this resolution can be achieved but one also has to be very careful in adjusting the lenses. According to the simulations we are able to scan an area of $200 * 200\mu\text{m}^2$ without any distortion of the focal plane. Even outside this area the distortion is smaller than 10^{-4}.

7.1.1 Properties of a toroidal potential

A toroidal potential well can be produced by scanning a focused laser beam in a circle. The toroidal potential confines the atoms well in the transversal direction but not along the beam direction. The strength of the confinement and also the depth are determined by the time averaged optical dipole force applied to the atoms. Let us assume we scan a ring of radius R with a focused laser beam of power P and a waist of w_0 in the focal plane. From a simple calculation we find the averaged intensity to

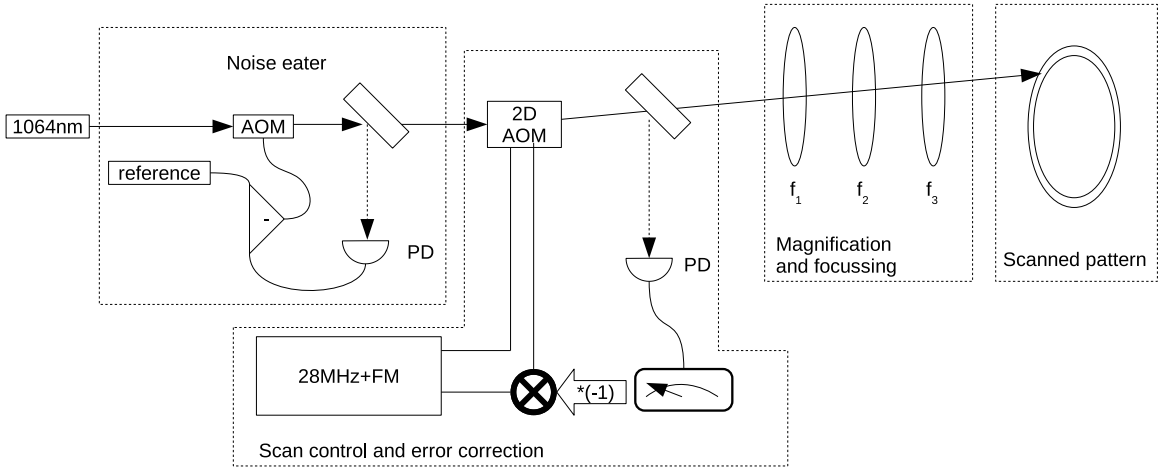

Figure 7.1: First the noise eater stabilises the power of the laser beam. The two-dimensional AOM deflects the stabilised laser beam. Finally the scanned beam is magnified and focused.

be [35]

$$I(r) = \frac{4P}{w_0^2} \exp\left(-\frac{2(r^2 - R^2)}{w_0^2}\right) \; J_0(\xi) \tag{7.1}$$

with the modified zeroth-order Bessel function $J_0(\xi)$ as a function of $\xi = 4Rr/w_0^2$, R is the radius of the ring, r the spatial position and w_0 the waist of the scanned beam at the focus. Substituting equation 7.1 into equation 3.18 we find the optical dipole potential of a toroidal trap. A plot of such a toroidal potential is given in figure 7.2. The depth in all plots of the ring is given in units of $T = E/k_{\mathrm{B}}$. In figure 7.2(a) is shown the toroidal potential in the horizontal plane at the focus. The potential through the centre of the ring along one direction is shown figure 7.2(b). The potential in the vertical plane through the centre of the trap is shown on figure 7.2(c). Again note the different scale on the r and z axes resulting in a stronger confinement in the horizontal plane than in the vertical plane along the z direction. The minimum of the trap is at $r = R$ and the atoms of mass m oscillate in the transverse direction with a frequency of

$$\omega_r = 4 \sqrt{-\frac{\kappa P e^{-\rho} \left[8a^2 \left(\mathcal{J}_1(\rho) - \mathcal{J}_0(\rho)\right) + w_0^2 \left(\mathcal{J}_0(\rho) + \mathcal{J}_1(\rho)\right)\right]}{m w_0^6}} \tag{7.2}$$

with $\rho = \frac{4a^2}{w_0^2}$, $U_0 = -\kappa P$ and $\mathcal{J}_n$ the n-th order modified Bessel function. In figure 7.3(a) is a plot showing the trapping frequency as a function of the scanned radius R. The trapping frequency decreases rapidly for radii smaller than the waist of the beam, reaches a local minimum and decreases slowly with larger radii. For radii smaller than $R \approx 0.6\ w_0$ the potential remains a single well potential that becomes wider. When scanning radii larger than $R \approx 0.6\ w_0$ a double well structure emerges with lower trapping frequencies.

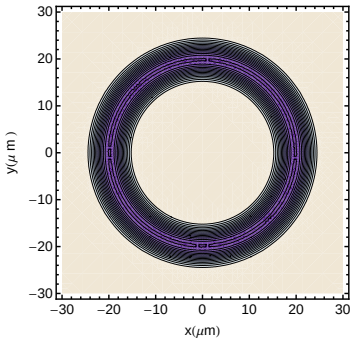

(a) The toroidal potential along the x and y axis at $z = 0$.

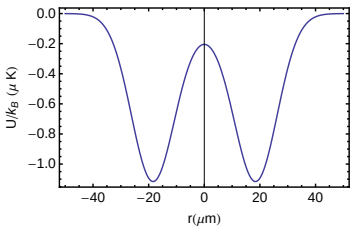

(b) The toroidal potential along the x-axis at $y = 0$ and $z = 0$.

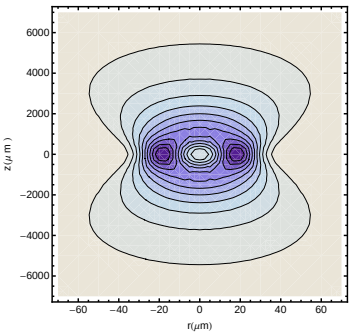

(c) The toroidal potential along the x and z-axis for $y = 0$.

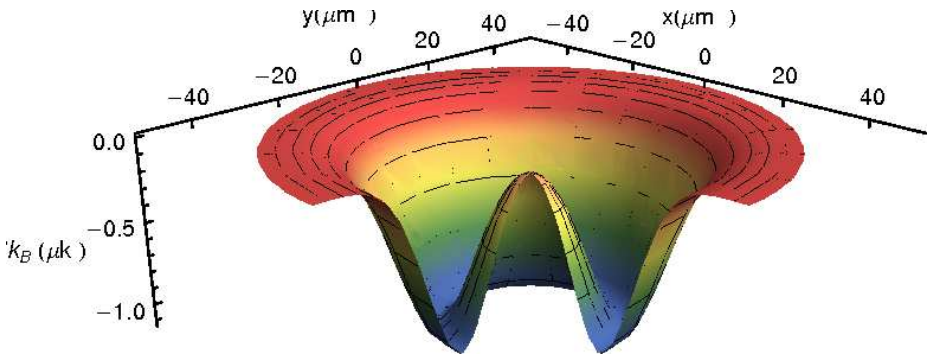

(d) The toroidal potential along the x and y-axis for $z = 0$.

Figure 7.2: Profiles of a toroidal potential for $R_0 = 20\mu$m, $w_0 = 15\mu$m, $P = 1$mW and $\lambda = 1064$nm.

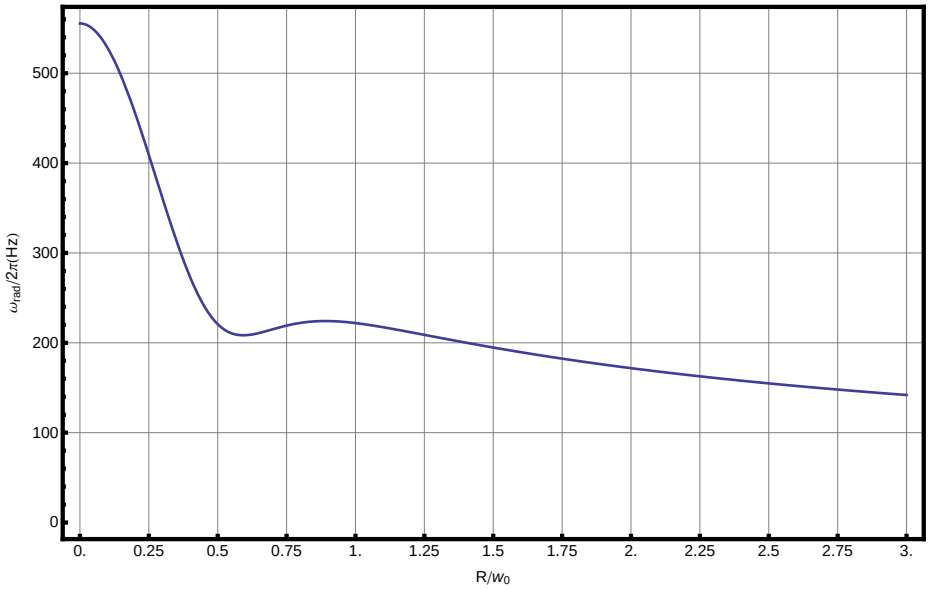

(a) The trapping frequency of a toroidal trap as a function of the scanned radius R with laser beam of a power of 1mW, a waist of $w_0 = 15\mu$m and a wavelength of $\lambda = 1064$nm.

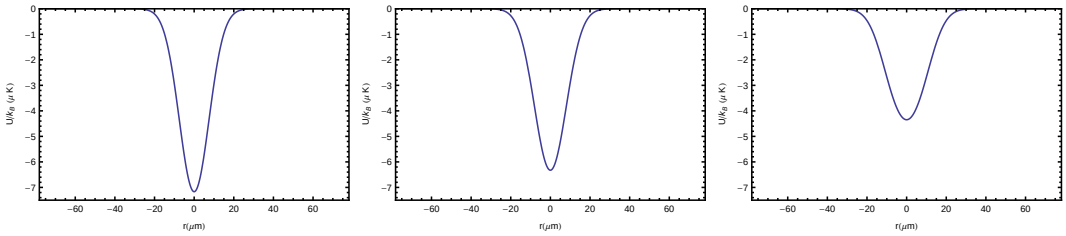

(b) $R = 0\ w_0$ (c) $R = 0.25\ w_0$ (d) $R = 0.5\ w_0$

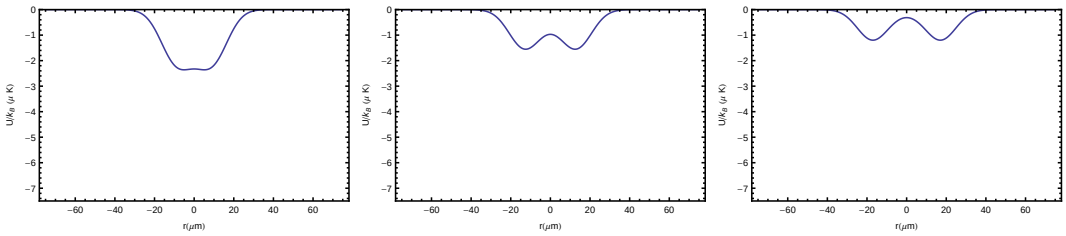

(e) $R = 0.75\ w_0$ (f) $R = 1.0\ w_0$ (g) $R = 1.25\ w_0$

Figure 7.3: The trapping frequency as a function of the radius is shown in 7.3(a) while b-g shows cross sections through the centre of the potential well for the same parameters.

7.2 Bosons in toroidal traps a summary of some theory and outlook

Toroidal traps are of particular interest on account of their periodic boundary conditions. Among the tremendous amount of theoretical work on BECs in toroidal traps we will look into some of the theory and how we could apply some experiments that could verify theoretical predictions. A very important parameter that determines the dynamics of a BEC is the ratio of the scattering length over the oscillator length (compare 2.17). By changing these parameters the interaction becomes either attractive or repulsive but also determines the dimensionality of the system. Also the number of particles and the temperature are important parameters that determine the dynamics. Let us assume a toroidal potential of radius R_0 is given by

$$V(r,z) = \frac{\lambda}{4}(r^2 - R_0^2)^2 + \frac{m\omega_z^2}{z^2} \tag{7.3}$$

s where λ is in units of $0.477\text{peV}/\mu\text{m}^4$. In order to determine the chemical potential and the wave function we would have to solve the GP equation. We will continue the discussion in the Thomas-Fermi limit in order to deduce an expression for the wave function and the chemical potential. The Thomas-Fermi approximation holds if $N \gg (\hbar^2/2m)(\lambda R_0^2 + m\omega_z^2/2)/\mu_0^2$ with the bare chemical potential $\mu_0 = (2/\pi^2)(\lambda/4)^{1/4}(m\omega_z^2/2)^{1/4}g^{1/2}$. The solution of the wave function in the Thomas-Fermi limit is given by

$$\Psi(\mathbf{r}) = \left(\frac{1}{gN}[\mu - V_0(\mathbf{r})]\right)^{1/2} \Theta[\mu - V_0(\mathbf{r})]. \tag{7.4}$$

The dimensionality is determined by comparison of the chemical potential with the oscillator energies, thus we summarise in table 7.1

dimensionality	condition	chemical potential
1D	$\mu < \hbar\omega_\rho$	$\mu_{1\mathrm{D}} = \hbar\overline{\omega}\frac{Na}{\pi R_0}$
2D	$\hbar\omega_\rho < \mu < \hbar\omega_z$	$\mu_{2\mathrm{D}} = \hbar\overline{\omega}\left(\frac{\omega_\rho}{\omega_z}\right)^{1/6}\left(\frac{3Na}{4\sqrt{\pi}R_0}\right)^{2/3}$
3D	$\mu > \hbar\omega_z$	$\mu_{3\mathrm{D}} = \hbar\overline{\omega}\sqrt{\frac{2Na}{\pi R_0}}$

Table 7.1: The dimensionality of the toroidal potential depends on the relation of the chemical potential and the oscillator energy. Where $\overline{\omega}$ is the geometric mean of the transverse and axial trapping frequencies ω_z and ω_ρ.

7.3 Experiments with atoms in a scanning dipole trap

A major advantage of the fast scanning dipole trap is the dynamic control over the trapping potential, and versatile applications which we briefly discuss here.

Atom interferometry

Interferometry is an important technique in physics to detect the phase shift between two paths of an interferometer. With a Sagnac interferometer one can measure the rate of rotation by the induced phase shift, which is proportional to the enclosed area of the paths and inversely proportional to wavelength of photons and massive particles given by

$$\Delta\Phi = \frac{4\pi\Omega \cdot A}{\lambda v}. \tag{7.5}$$

Here lambda is the wavelength of the particle, which is the de Broglie wavelength $\lambda_{db} = h/mv$ for a massive particle, and v the velocity of the particle. Assuming an atom- and light-based interferometer of the same enclosed area we find the intrinsic sensitivity is larger by a factor 10^{11} for rubidium atoms compared to visible

light. Better beamsplitters for light than for atoms and highly reflective mirrors lets one easier increase the enclosed area for a light-based interferometer than for an atom-interferometer and the intrinsic sensitivity advantage of an atom-interferometer becomes smaller. However, we are able to scan toroidal time averaged potentials of radii up to 150μm. In such a trap the sensitivity would be greater by a factor $24 \cdot 10^3$ compared to a light-based interferometer of an area of 1m^2.

Finite lattices

Optical lattices created by tightly focused and retro-reflected laser beams form a lattice (along the direction of the propagation) with a spacing between lattice sites of half the wave length of the focusing laser. In such an optical lattice one can neither change the spacing between individual lattice sites nor the on-site lattice depth. Here again the dynamic control over the on-site power and position at the same time allows us to scan finite lattices with individual control of the on-site lattice depth. An interesting experiment would be to begin with spinpolarised BECs on each lattice and to observe the spontaneous magnetisation as the system evolves in time.

Controlled vortex creation

In contrast to the spontaneous formation of vortices [107] the simulations performed by J.Butcher [108] show that it is possible to create vortex states in a controlled way in a scanning beam trap. In these simulations we initially trap a BEC in a single beam trap and start scanning a finite lattice of four sites. Although the number on each site is statistically determined they all have the same phase. By increasing the depth on individual lattice sites we can imprint a known phase onto the wave function on each lattice sites. If imprinting the phase difference such it is a multiple of 2π between the first and the last lattice site, we would expect from the free expanding BECs to form a vortex state when they interfere.

8 Conclusions and outlook

The author's work reported in this thesis was aimed to build an apparatus to create an all optical BEC. The creation of an all-optical ^{87}Rb BEC was realised in a crossed optical dipole trap at a wavelength of $\lambda = 1064$nm. The trapping of neutral atoms in an optical dipole trap is spin independent and a mixed spinor condensate among the $F = 1$ manifold with $m_F = \{-1, 0, +1\}$ is formed. The work confirmed an earlier report that a particular spin state can be prepared by applying a magnetic gradient field during the evaporation. Yet the experiments on Bose-Einstein condensation remain challenging as many different components of such experiments have to work precisely together.

This thesis is mainly concerned with experimental details on the trapping of ^{87}Rb atoms from a hot vapour and cooling in a magneto optical trap and further evaporation to quantum degeneracy in a crossed optical dipole trap with accurate control of the power in both beams via a feedback loop. A major improvement made during the development of the system was replacing the free space coupled MOT with optical fibres. From then on we were able to quickly diagnose and if necessary to optimise the MOT. Currently we load from approximately 95 million atoms after the temporal dark MOT up to 5 million atoms into the optical dipole trap to start the evaporation with. The loading of the MOT could be further improved by building a 2D MOT system to load a 3D MOT separated by an aperture. The loading will then be on the order of a few seconds, decreasing the duty cycle of the experiment further with longer life times of the trapped atoms. With our current procedure we can now routinely

create almost pure Bose-Einstein condensates purely in the $m_F = 0$ state with nearly 7000 atoms in the condensed fraction. This was successfully demonstrated just a few weeks before submission of the thesis was due.

The number of all optical BEC experiments has grown over the years, yet there are not as many as their magnetic counterparts. Also the modelling of the dynamics of the evaporation is well established for magnetic traps but not so well for optical traps. We found that although the standard theory agreed very well with our measurements of the MOT, it did not account well for the dynamics of the evaporation process which led to condensation. Another interesting and useful phenomenon was the formalism of condensed pure spin states when the evaporation was carried out in a magnetic field gradient. Such behaviours have been reported previously and it is hoped that this confirmation will spark interest in explaining and modelling the effect. This already leaves plenty of research for the future. Since the formation of an all optical BEC works reliably we have opened the door to investigate Bose-Einstein condensates in arbitrary potentials using a time averaged scanning dipole trap.

Bibliography

[1] M. H. Anderson, J. R. Ensher, M. R. Matthews, C. E. Wieman, and E. A. Cornell. Observation of bose-einstein condensation in a dilute atomic vapor. *Science*, 269(5221):198–201, 1995.

[2] K. B. Davis, M. O. Mewes, M. R. Andrews, N. J. van Druten, D. S. Durfee, D. M. Kurn, and W. Ketterle. Bose-einstein condensation in a gas of sodium atoms. *Phys. Rev. Lett.*, 75(22):3969–3973, Nov 1995.

[3] Franco Dalfovo, Stefano Giorgini, Lev P. Pitaevskii, and Sandro Stringari. Theory of bose-einstein condensation in trapped gases. *Rev. Mod. Phys.*, 71(3):463–512, Apr 1999.

[4] Anthony J. Leggett. Bose-einstein condensation in the alkali gases: Some fundamental concepts. *Rev. Mod. Phys.*, 73(2):307–356, Apr 2001.

[5] D. S. Durfee W. Ketterle and D. M. Stamper-Kurn. Making, probing and understanding bose-einstein condensates. *Proceedings of the International School of Physics Enrico Fermi*, pages pp. 67–176, 1999.

[6] Bose. Plancks gesetz und lichtquantenhypothese. *Zeitschrift fuer Physik A Hadrons and Nuclei*, 26(1):178–181, 1924.

[7] Zur quantentheorie des idealen gases. *Sitzungsber. Preuss. Akad. Wiss.*, Bericht 3:18, 1925.

[8] M. R. Andrews, C. G. Townsend, H. J. Miesner, D. S. Durfee, D. M. Kurn,

and W. Ketterle. Observation of interference between two bose condensates. *Science*, 275(5300):637–641, 1997.

[9] P. Kapitza. Viscosity of liquid helium below the λ-point. *Nature*, 141:74–74, 1938.

[10] John D. Reppy and David Depatie. Persistent currents in superfluid helium. *Phys. Rev. Lett.*, 12(8):187–189, Feb 1964.

[11] F. London. On the bose-einstein condensation. *Phys. Rev.*, 54(11):947–954, Dec 1938.

[12] On the theory of superfluidity. *J. Phys. (USSR)*, 11:23, 1947.

[13] J. R. Abo-Shaeer, C. Raman, J. M. Vogels, and W. Ketterle. Observation of vortex lattices in bose-einstein condensates. *Science*, 292(5516):476–479, 2001.

[14] B. P. Anderson, P. C. Haljan, C. E. Wieman, and E. A. Cornell. Vortex precession in bose-einstein condensates: Observations with filled and empty cores. *Phys. Rev. Lett.*, 85(14):2857–2860, Oct 2000.

[15] E. Hodby, G. Hechenblaikner, S. A. Hopkins, O. M. Maragò, and C. J. Foot. Vortex nucleation in bose-einstein condensates in an oblate, purely magnetic potential. *Phys. Rev. Lett.*, 88(1):010405, Dec 2001.

[16] K. W. Madison, F. Chevy, W. Wohlleben, and J. Dalibard. Vortex formation in a stirred bose-einstein condensate. *Phys. Rev. Lett.*, 84(5):806–809, Jan 2000.

[17] M. R. Matthews, B. P. Anderson, P. C. Haljan, D. S. Hall, C. E. Wieman, and E. A. Cornell. Vortices in a bose-einstein condensate. *Phys. Rev. Lett.*, 83(13):2498–2501, Sep 1999.

[18] R. Onofrio, C. Raman, J. M. Vogels, J. R. Abo-Shaeer, A. P. Chikkatur, and W. Ketterle. Observation of superfluid flow in a bose-einstein condensed gas. *Phys. Rev. Lett.*, 85(11):2228–2231, Sep 2000.

[19] C. Raman, M. Köhl, R. Onofrio, D. S. Durfee, C. E. Kuklewicz, Z. Hadzibabic, and W. Ketterle. Evidence for a critical velocity in a bose-einstein condensed gas. *Phys. Rev. Lett.*, 83(13):2502–2505, Sep 1999.

[20] M. D. Barrett, J. A. Sauer, and M. S. Chapman. All-optical formation of an atomic bose-einstein condensate. *Phys. Rev. Lett.*, 87(1):010404, Jun 2001.

[21] M. S. Chang, C. D. Hamley, M. D. Barrett, J. A. Sauer, K. M. Fortier, W. Zhang, L. You, and M. S. Chapman. Observation of spinor dynamics in optically trapped ^{87}Rb Bose-Einstein Condensates. *Phys. Rev. Lett.*, 92(14):140403, Apr 2004.

[22] W. Ketterle and D. E. Pritchard. Earlyring1. *Applied Physics B:L asers and Optics*, 54(4):403–406, 1992.

[23] A. S. Arnold, C. S. Garvie, and E. Riis. Large magnetic storage ring for bose-einstein condensates. *Phys. Rev. A*, 73(4):041606, Apr 2006.

[24] S. Gupta, K. W. Murch, K. L. Moore, T. P. Purdy, and D. M. Stamper-Kurn. Bose-einstein condensation in a circular waveguide. *Phys. Rev. Lett.*, 95(14):143201, Sep 2005.

[25] J. A. Sauer, M. D. Barrett, and M. S. Chapman. Storage ring for neutral atoms. *Phys. Rev. Lett.*, 87(27):270401, Dec 2001.

[26] Olivier Morizot, Yves Colombe, Vincent Lorent, Hélène Perrin, and Barry M. Garraway. Ring trap for ultracold atoms. *Phys. Rev. A*, 74(2):023617, Aug 2006.

[27] Spencer E. Olson, Matthew L. Terraciano, Mark Bashkansky, and Fredrik K. Fatemi. Cold-atom confinement in an all-optical dark ring trap. *Phys. Rev. A*, 76(6):061404, Dec 2007.

[28] A. D. Jackson and G. M. Kavoulakis. Bose-einstein-condensed atoms in toroidal traps. *Phys. Rev. A*, 74(6):065601, Dec 2006.

[29] M. Modugno, C. Tozzo, and F. Dalfovo. Detecting phonons and persistent currents in toroidal bose-einstein condensates by means of pattern formation. *Phys. Rev. A*, 74(6):061601, Dec 2006.

[30] L. Salasnich, A. Parola, and L. Reatto. Transition from three dimensions to one dimension in bose gases at zero temperature. *Phys. Rev. A*, 70(1):013606, Jul 2004.

[31] L. Salasnich, A. Parola, and L. Reatto. Thermodynamics of solitonic matter waves in a toroidal trap. *Phys. Rev. A*, 74(3):031603, Sep 2006.

[32] Frank Moscatelli, Charles Sackett, Shengwang Du, and Eun Oh. Far-off-resonant ring trap near the ends of optical fibers. *Phys. Rev. A*, 76(4):043404, Oct 2007.

[33] E. M. Wright, J. Arlt, and K. Dholakia. Toroidal optical dipole traps for atomic bose-einstein condensates using laguerre-gaussian beams. *Phys. Rev. A*, 63(1):013608, Dec 2000.

[34] K. Helmerson, M. F. Andersen, C. Ryu, P. Cladé, V. Natarajan, A. Vaziri, and W. D. Phillips. Generating persistent currents states of atoms using orbital angular momentum of photons. *Nuclear Physics A*, 790(1–4):705–712, 2007. ¡ce:title¿Few-Body Problems in Physics¡/ce:title¿ ¡ce:subtitle¿FB 18¡/ce:subtitle¿ ¡xocs:full-name¿18th International IUPAP Conference on Few-Body Problems in Physics¡/xocs:full-name¿.

[35] S. K. Schnelle, E. D. van Ooijen, M. J. Davis, N. R. Heckenberg, and H. Rubinsztein-Dunlop. Versatile two-dimensional potentials for ultra-cold atoms. *Opt. Express*, 16(3):1405–1412, Feb 2008.

[36] F. Dalfovo, L. Pitaevskii, and S. Stringari. Order parameter at the boundary of a trapped bose gas. *Phys. Rev. A*, 54(5):4213–4217, Nov 1996.

[37] Franco Dalfovo, Stefano Giorgini, Lev P. Pitaevskii, and Sandro Stringari. Theory of bose-einstein condensation in trapped gases. *Rev. Mod. Phys.*, 71(3):463–512, Apr 1999.

[38] J. R. Ensher, D. S. Jin, M. R. Matthews, C. E. Wieman, and E. A. Cornell. Bose-einstein condensation in a dilute gas: Measurement of energy and ground-state occupation. *Phys. Rev. Lett.*, 77(25):4984–4987, Dec 1996.

[39] M. O. Mewes, M. R. Andrews, N. J. van Druten, D. M. Kurn, D. S. Durfee, and W. Ketterle. Bose-einstein condensation in a tightly confining dc magnetic trap. *Phys. Rev. Lett.*, 77(3):416–419, Jul 1996.

[40] M. O. Mewes, M. R. Andrews, N. J. van Druten, D. M. Kurn, D. S. Durfee, C. G. Townsend, and W. Ketterle. Collective excitations of a bose-einstein condensate in a magnetic trap. *Phys. Rev. Lett.*, 77(6):988–991, Aug 1996.

[41] William D. Phillips. Nobel lecture: Laser cooling and trapping of neutral atoms. *Rev. Mod. Phys.*, 70(3):721–741, Jul 1998.

[42] Claude N. Cohen-Tannoudji. Nobel lecture: Manipulating atoms with photons. *Rev. Mod. Phys.*, 70(3):707–719, Jul 1998.

[43] Steven Chu. Nobel lecture: The manipulation of neutral particles. *Rev. Mod. Phys.*, 70(3):685–706, Jul 1998.

[44] A. Ashkin. Trapping of atoms by resonance radiation pressure. *Phys. Rev. Lett.*, 40(12):729–732, Mar 1978.

[45] E. L. Raab, M. Prentiss, Alex Cable, Steven Chu, and D. E. Pritchard. Trapping of neutral sodium atoms with radiation pressure. *Phys. Rev. Lett.*, 59(23):2631–2634, Dec 1987.

[46] T. W. Hänsch and A. L. Schawlow. Cooling of gases by laser radiation. *Optics Communications*, 13(1):68–69, 1975.

[47] D.Wineland and H. Dehmelt. Proposed $10^14\delta\nu/\nu$ laser fluorescence spectroscopy on tl^+ mono-ion oscillator. *Bull. Am. Phys. Soc.*, 20:637, 1975.

[48] P. D. Lett, W. D. Phillips, S. L. Rolston, C. E. Tanner, R. N. Watts, and C. I. Westbrook. Optical molasses. *J. Opt. Soc. Am. B*, 6(11):2084–2107, 1989.

[49] J. Dalibard and C. Cohen-Tannoudji. Laser cooling below the doppler limit by polarization gradients: simple theoretical models. *J. Opt. Soc. Am. B*, 6(11):2023–2045, Nov 1989.

[50] D. Hoffmann, P. Feng, R. S. Williamson, and T. Walker. Excited-state collisions of trapped ^{85}Rb atoms. *Phys. Rev. Lett.*, 69(5):753–756, Aug 1992.

[51] D. Sesko, T. Walker, C. Monroe, A. Gallagher, and C. Wieman. Collisional losses from a light-force atom trap. *Phys. Rev. Lett.*, 63(9):961–964, Aug 1989.

[52] M. Prentiss, A. Cable, J. E. Bjorkholm, Steven Chu, E. L. Raab, and D. E. Pritchard. Atomic-density-dependent losses in an optical trap. *Opt. Lett.*, 13(6):452–454, Jun 1988.

[53] John Weiner, Vanderlei S. Bagnato, Sergio Zilio, and Paul S. Julienne. Experiments and theory in cold and ultracold collisions. *Rev. Mod. Phys.*, 71(1):1–85, Jan 1999.

[54] L. Marcassa, V. Bagnato, Y. Wang, C. Tsao, J. Weiner, O. Dulieu, Y. B. Band, and P. S. Julienne. Collisional loss rate in a magneto-optical trap for sodium atoms: Light-intensity dependence. *Phys. Rev. A*, 47(6):–4563, Jun 1993.

[55] Thad Walker, David Sesko, and Carl Wieman. Collective behavior of optically trapped neutral atoms. *Phys. Rev. Lett.*, 64(4):408–411, Jan 1990.

[56] C. Monroe, W. Swann, H. Robinson, and C. Wieman. Very cold trapped atoms in a vapor cell. *Phys. Rev. Lett.*, 65(13):1571–1574, Sep 1990.

[57] A. Ashkin. Acceleration and trapping of particles by radiation pressure. *Phys. Rev. Lett.*, 24(4):156–159, Jan 1970.

[58] V. S. Letokhov, V. G. Minogin, and B. D. Pavlik. Cooling and trapping of atoms and molecules by a resonant laser field. *Optics Communications*, 19(1):72–75, 1976.

[59] A. Ashkin. Trapping of atoms by resonance radiation pressure. *Phys. Rev. Lett.*, 40(12):729–732, Mar 1978.

[60] Steven Chu, J. E. Bjorkholm, A. Ashkin, and A. Cable. Experimental observation of optically trapped atoms. *Phys. Rev. Lett.*, 57(3):314–317, Jul 1986.

[61] J. D. Miller, R. A. Cline, and D. J. Heinzen. Far-off-resonance optical trapping of atoms. *Phys. Rev. A*, 47(6):–4567, Jun 1993.

[62] K. L. Corwin, S. J. M. Kuppens, D. Cho, and C. E. Wieman. Spin-polarized atoms in a circularly polarized optical dipole trap. *Phys. Rev. Lett.*, 83(7):1311–1314, Aug 1999.

[63] S. J. M. Kuppens, K. L. Corwin, K. W. Miller, T. E. Chupp, and C. E. Wieman. Loading an optical dipole trap. *Phys. Rev. A*, 62(1):013406, Jun 2000.

[64] B. M. Garraway and V. G. Minogin. Theory of an optical dipole trap for cold atoms. *Phys. Rev. A*, 62(4):043406, Sep 2000.

[65] Rudolf Grimm, Matthias Weidemüller, and Yurii B. Ovchinnikov. Optical dipole traps for neutral atoms. *Adv. At. Mol. Opt. Phys.*, 42:95–170, Feb 2000.

[66] J. Dalibard and C. Cohen-Tannoudji. Dressed-atom approach to atomic motion in laser light: the dipole force revisited. *J. Opt. Soc. Am. B*, 2(11):1707–1720, 1985.

[67] S. Friebel, C. D'Andrea, J. Walz, M. Weitz, and T. W. Hänsch. CO_2-laser optical lattice with cold rubidium atoms. *Phys. Rev. A*, 57(1):–20, Jan 1998.

[68] T. A. Savard, K. M. O'Hara, and J. E. Thomas. Laser-noise-induced heating in far-off resonance optical traps. *Phys. Rev. A*, 56(2):–1095, Aug 1997.

[69] Milton Abramowitz and Irene A. Stegun. *Handbook of Mathematical Functions with Formulas, Graphs, and Mathematical Tables*. Dover, New York, ninth dover printing, tenth gpo printing edition, 1964.

[70] Jochen Kronenjaeger. *Coherent Dynamics of Spinor Bose-Einstein Condensates*. PhD thesis.

[71] Martin Brinkmann. Optimierung der detektion und auswertung von ^{87}Rb-Spinor-Kondensaten. Master's thesis, ILP Hamburg, 2005.

[72] Michael Erhardt. *Experimente mit mehrkomponentigen Bose-Einstein-Kondensaten*. PhD thesis, ILP Hamburg, 2004.

[73] E. L. Raab, M. Prentiss, Alex Cable, Steven Chu, and D. E. Pritchard. Trapping of neutral sodium atoms with radiation pressure. *Phys. Rev. Lett.*, 59(23):2631–2634, Dec 1987.

[74] C. Klempt, T. van Zoest, T. Henninger, O. Topic, E. Rasel, W. Ertmer, and J. Arlt. Ultraviolet light-induced atom desorption for large rubidium and potassium magneto-optical traps. *Phys. Rev. A*, 73(1):013410, Jan 2006.

[75] Kendall B. Davis, Marc-Oliver Mewes, Michael A. Joffe, Michael R. Andrews, and Wolfgang Ketterle. Evaporative cooling of sodium atoms. *Phys. Rev. Lett.*, 74(26):5202–5205, Jun 1995.

[76] D. J. Wineland, C. E. Wieman, S. J. Smith, and American Institute of Physics. Atomic physics 14: Fourteenth international conference on atomic physics, boul-

der, co, 1994. In *1M-3*, AIP conference proceedings. American Institute of Physics, 1995.

[77] D. J. Wineland, C. E. Wieman, S. J. Smith, and American Institute of Physics. Atomic physics 14: Fourteenth international conference on atomic physics, boulder, co, 1994. In *1M-7*, AIP conference proceedings. American Institute of Physics, 1995.

[78] Toshiya Kinoshita, Trevor Wenger, and David S. Weiss. All-optical bose-einstein condensation using a compressible crossed dipole trap. *Phys. Rev. A*, 71(1):011602, Jan 2005.

[79] Nathan E. Lundblad, Robert J. Thompson, David C. Aveline, and Lute Maleki. Initial experiments with an all-optical spinor bec. In *Conference on Lasers and Electro-Optics/Quantum Electronics and Laser Science Conference and Photonic Applications Systems Technologies*, pages –6. Optical Society of America, 2006.

[80] P. Ahmadi, B. P. Timmons, and G. S. Summy. Geometrical effects in the loading of an optical atom trap. *Phys. Rev. A*, 72(2):023411, Aug 2005.

[81] J. F. Clément, J. P. Brantut, M. Robert-de Saint-Vincent, R. A. Nyman, A. Aspect, T. Bourdel, and P. Bouyer. All-optical runaway evaporation to bose-einstein condensation. *Phys. Rev. A*, 79(6):061406, Jun 2009.

[82] M.D. Barrett K.J. Arnold. All-optical bose–einstein condensation in a 1.06 μm dipole trap. *Optics Communications*, 284(13):3288–3291, 2011.

[83] S. J. M. Kuppens, K. L. Corwin, K. W. Miller, T. E. Chupp, and C. E. Wieman. Loading an optical dipole trap. *Phys. Rev. A*, 62(1):013406, Jun 2000.

[84] Andrzej Szczepkowicz, Leszek Krzemie´n, Adam Wojciechowski, Krzysztof Brzozowski, Michael Krüger, MichałZawada, Marcin Witkowski, Jerzy Za-

chorowski, and Wojciech Gawlik. Optimal geometry for efficient loading of an optical dipole trap. *Phys. Rev. A*, 79(1):013408, Jan 2009.

[85] E. A. Burt, R. W. Ghrist, C. J. Myatt, M. J. Holland, E. A. Cornell, and C. E. Wieman. Coherence, correlations, and collisions: What one learns about bose-einstein condensates from their decay. *Phys. Rev. Lett.*, 79(3):337–340, Jul 1997.

[86] T. Lauber, J. Küber, O. Wille, and G. Birkl. Optimized bose-einstein-condensate production in a dipole trap based on a 1070-nm multifrequency laser: Influence of enhanced two-body loss on the evaporation process. *Phys. Rev. A*, 84(4):043641, Oct 2011.

[87] K. Arnold. private communication. Natioanl University of Singapore.

[88] Tin-Lun Ho. Spinor bose condensates in optical traps. *Phys. Rev. Lett.*, 81(4):742–745, Jul 1998.

[89] Tetsuo Ohmi and Kazushige Machida. Bose-einstein condensation with internal degrees
of freedom in alkali atom gases. *Journal of the Physical Society of Japan*, 67(6):1822–1825, 1998.

[90] Inouye S. Stamper-Kurn D. M. Miesner H.-J Chikkatur A. P. Ketterle W Stenger, J. Spin domains in ground-state Bose-Einstein condensates. *Nature*, 396(6709):345, 1998.

[91] C. K. Law, H. Pu, and N. P. Bigelow. Quantum spins mixing in spinor bose-einstein condensates. *Phys. Rev. Lett.*, 81(24):5257–5261, Dec 1998.

[92] Wenxian Zhang, Su Yi, and Li You. Mean field ground state of a spin-1 condensate in a magnetic field. *New Journal of Physics*, 5(1):77, 2003.

[93] Wenxian Zhang, Su Yi, and L. You. Bose-einstein condensation of trapped interacting spin-1 atoms. *Phys. Rev. A*, 70(4):043611, Oct 2004.

[94] M. S. Chang, C. D. Hamley, M. D. Barrett, J. A. Sauer, K. M. Fortier, W. Zhang, L. You, and M. S. Chapman. Observation of Spinor Dynamics in Optically Trapped ^{87}Rb Bose-Einstein Condensates. *Phys. Rev. Lett.*, 92(14):140403, Apr 2004.

[95] C. Hamley K. Fortier J.A. Sauer M.D. Barrett, M.-S. Chang and M.S. Chapman. All-optical atomic bose-einstein condensates. In E.J. Heller H. R. Saeghpour and D.E. Pritchard, editors, *Prceedings of the XVII International Conference on Atomic Physics*, page 31. World Sientific, 2003.

[96] H. Smith C. J. Pethick. *Bose-Einstein condensation in dilute gases*. Cambridge ; New York : Cambridge University Press,, 2008.

[97] S. Giorgini, L. P. Pitaevskii, and S. Stringari. Condensate fraction and critical temperature of a trapped interacting bose gas. *Phys. Rev. A*, 54(6):4633, Dec 1996.

[98] Johanna Nes M.Sc. *Cold Atoms and Bose-Einstein Condensates in Optical Dipole Potentials*. PhD thesis, Institu für Angewandte Physik, Technische Universität darmstadt.

[99] Dipl.-Phys. Oliver Wille. *Manipulation von Bose-Einstein Kondensaten in ptischen Dipolpotentialen*. PhD thesis, Institu für Angewandte Physik, Technische Universität darmstadt, August 2010.

[100] Sylvi Händel. *Experiments on ultracold quantum gases of ^{85}Rb and ^{87}Rb*. PhD thesis, Department of Physics, Durham University, October 2011.

[101] Wolfgang Ketterle and N. J. van Druten. Bose-einstein condensation of a fi-

nite number of particles trapped in one or three dimensions. *Phys. Rev. A*, 54(1):656–660, Jul 1996.

[102] J. P. Martikainen. Bose-einstein condensation in shallow traps. *Phys. Rev. A*, 63(4):043602, Mar 2001.

[103] C. Ryu, M. F. Andersen, P. Clade, Vasant Natarajan, K. Helmerson, and W. D. Phillips. Observation of persistent flow of a bose-einstein condensate in a toroidal trap, 2007.

[104] A. Görlitz, J. M. Vogels, A. E. Leanhardt, C. Raman, T. L. Gustavson, J. R. Abo-Shaeer, A. P. Chikkatur, S. Gupta, S. Inouye, T. Rosenband, and W. Ketterle. Realization of bose-einstein condensates in lower dimensions. *Phys. Rev. Lett.*, 87(13):130402, Sep 2001.

[105] G. J. Milburn, J. Corney, E. M. Wright, and D. F. Walls. Quantum dynamics of an atomic bose-einstein condensate in a double-well potential. *Phys. Rev. A*, 55(6):4318–4324, Jun 1997.

[106] J. Hecker Denschlag, J. E. Simsarian, H. Häffner, C. McKenzie, A. Browaeys, D. Cho, K. Helmerson, S. L. Rolston, and W. D. Phillips. A bose-einstein condensate in an optical lattice. *Journal of Physics B: Atomic, Molecular and Optical Physics*, 35(14):3095, 2002.

[107] C. C. Bradley, C. A. Sackett, J. J. Tollett, and R. G. Hulet. Evidence of bose-einstein condensation in an atomic gas with attractive interactions. *Phys. Rev. Lett.*, 75(9):1687–1690, Aug 1995.

[108] Jessica Butcher. Scanning potentials for an all-optical bose-einstein condensate. Master's thesis, Department of Mathematics and Physcics, July 2011.

[109] Daniel Adam Steck. Rubidium 87 line data.

A Cameras

For different purposes we have a camera from Prosillica (EC1380) and another one from Prinecton Instruments (Pixis). We use the camera from Prosillica to continuously monitor the MOT and to take absorption images in the horizontal plane. The camera from Princeton is used to take absorption images along gravity. To take pictures with the camera from Princeton the readily available software WinView was used. To operate the camera from Prosillica a graphical user interface was written in LabView which we will briefly introduce in the following sections.

A.1 Prosillica camera

A.1.1 Continuous operation

In figure A.1(a) and A.1(b) are screenshots shown of a program written by the author in LabView to monitor the fluorescent light of the MOT continuously with the camera from Prosillica camera. On the front panel the user will see in the upper left corner the image of the MOT and in the two columns on the right Gaussian fits and the widths through the maximum of the MOT along the transverse directions. The transverse lines through maximum can be highlighted by the user turning on or off the button 'Show Max'. The user can choose a region of interest of the chip with the sliders on the lower left on the camera, input the properties of the lenses of the imaging system and the pixel size of the camera. The exposure time and also the time steps from frame to frame can be chosen by the user. The lower right corner shows the

amplitude of the total intensity on the chip which can be saved into a file by starting the program. On the block diagram A.1(b) the flow and processing of the image is shown. Before the program enters the while loop the camera is initialised and a file dialogue box opens to save the total intensity into a *.txt-file. The program reads out continuously the image of the camera and sends it to another self written sub program where the actual fitting of the Gaussian profiles is calculated.

A.1.2 Taking absorption images

This self written program by the author in LabView triggers the camera to take three images, to display a preview of the absorption image and the line profiles through the maximum of intensity along the transverse direction. On the front panel the three images of the series are displayed on the left side. In the upper box the user can choose an area of interest of the chip and also the the exposure time of the chip. The graph in the center shows the calculated preview of the absorption image and on the top and left are graphs that show the line profiles along the transverse directions through the maximum of intensity. On the far right is a graph that shows the absorption image of the previous run. The user can save the images into a folder by switching the button 'Save Images' on or off. The three images are saved into a chosen folder with a format that includes the date, the number of the run and the extension atom, noatoms and background, e.g. 01_01_1900_000001_atoms.tif, 01_01_1900_000001_noatoms.tif and 01_01_1900_000001_background.tif. The program evaluates two parallel while loops as can be seen on the block diagram A.2(b). The first while loop constantly reads the level of a digital input. For a low level the variable 'Taking Images' is set to 'false' and is forwarded into the second while loop. The false case means that the camera will not take images. For a high level on the digital input the variable 'Taking Images' is set to true and forwarded to the second while loop. In the true case, in the second while loop as shown in A.2(b) the first sub.vi initialises the camera and takes three images when the camera is triggered. The following sub.vi calculates the

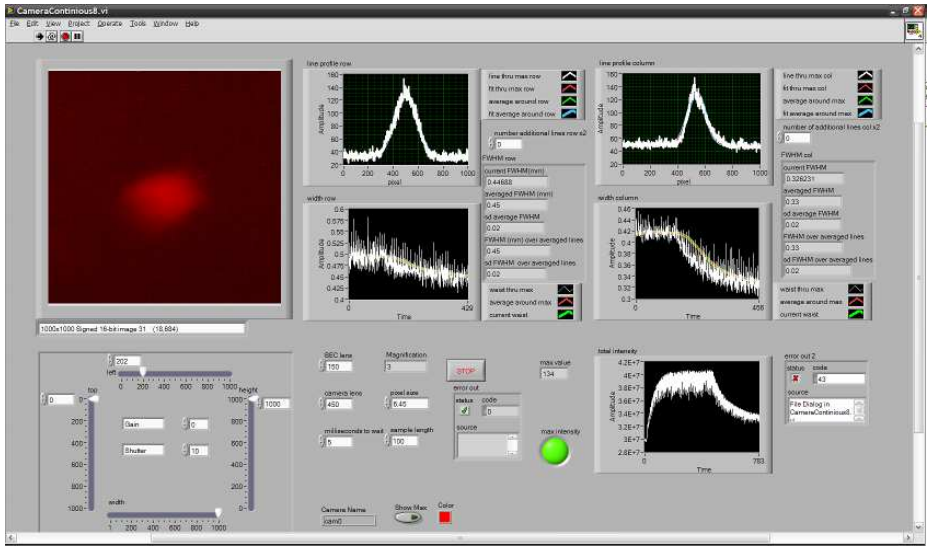

(a) On the front panel the continuous image of the fluorescent light of the MOT, upper left, the Gaussian fits right hand, the region of interest, lower left, properties of the imaging system and the total intensity lower right.

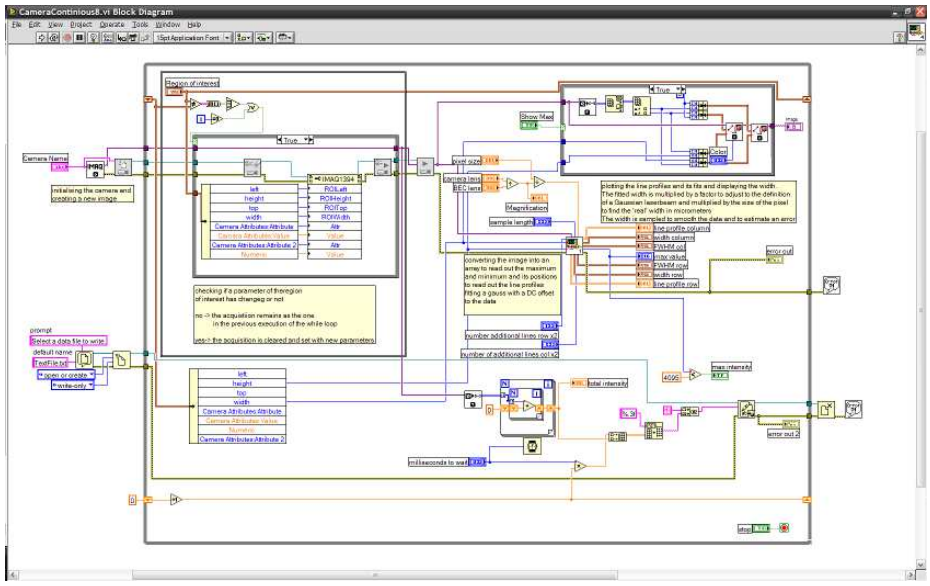

(b) The source code of the program. For a closer description please refer to the text.

Figure A.1: Front panel, upper figure, and block diagram, lower figure, of the program to monitor the MOT continuously.

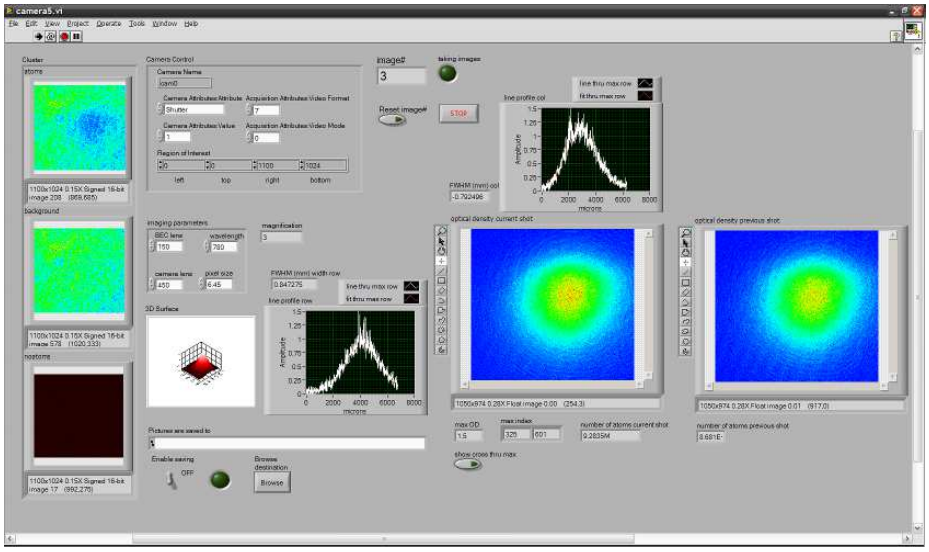

(a)

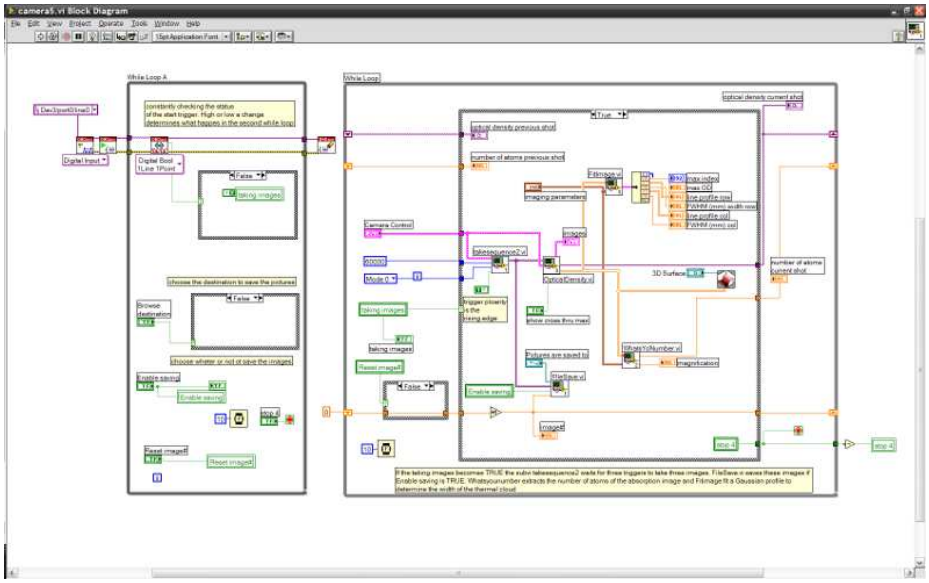

(b)

Figure A.2: Front panel, upper figure, and block diagram, lower figure, of the program to take absorption images with the Prosillica camera.

optical density with the three pictures as described in section 4.6.1. The following two sub.vis fit a Gaussian profile through the maximum of the optical density along the transverse directions and calculate the number of atoms according to equation 4.6.

A.2 Princeton Instruments camera

In our experiment we use a CCD camera from Princeton Instruments (Pixis). The properties of the camera like exposure time, triggering and the destination where to save the images are set with the manufacture's software WinView.

B Analysis

Quite a significant amount of time was spent on developing scripts in Mathematica to display and analyse the absorption images. We briefly explain the following script that was used to analyse the thermal fraction in the absorption images that were taken in the crossed dipole trap at the end of the evaporation cycle. On the front panel in Mathematica the user executes the function

CrossedTrapRegulated[image#,top,bottom,left,right,p1,p2,TOF]

was written to calculate the optical density (see section: 4.6.1) and to calculate quantities. The first variable is the number of the image to be analysed. The following four determine the region of interest of the image. The variables p1 and p2 are the powers of the beams of the optical dipole traps ODT1 and ODT2 in units of a voltage according to a calibration. The last variable TOF is the time of flight which is necessary to calculate the temperature of the atoms. The script starts testing the existence of the file and the length of the multipage .TIF to be read. If both tests are true the three images $\mathcal{A}$, $\mathcal{R}$ and $\mathcal{D}$ are read into the variables $atom, noatom$ and $back$. Each of these variables is a matrix with the dimension of the area of the CCD chip (or set region of interest set in WinView). A subarray given by choosing the boundaries (top, bottom,left, right) is selected and used to calculate the optical density of the region of interest (lines 37-67). To allow for noise in the image we determine the average profile in two directions (lines 87-88) and determine the position of the maximum along those directions (line 90-91). A two-dimensional Gaussian function (line 97) is then fitted (line99-102) to the two-dimensional data set

(line 93). The fitted parameters (line 106-111) are then used for various calculations. For visualisation a plot of the optical density, fitted cross sections and all quantities are summarised in the variable "plotsnnumbers" which is displayed on the front panel in Mathematica and also saved into the working directory as a .gif-file (see figure) along with text files .dat and .txt that contain all calculated quantities of each single image.

```
1  CrossedTrapRegulated[pic0_, top_, bottom_, left_, right_, p1_, p2_,
2     TOF_] :=
3    Module[{picnum = pic0, b = bottom, t = top, l = left, r = right,
4      pfirst = p1, psecond = p2, time = TOF},
5     Clear[data];
6     (*reading the rawdata images*)
7
8     picco = picnum;
9     imgfile = "image" <> ToString[picnum] <> ".TIF";
10    (* testing the existance of the selected image file*)
11
12    If[FileType[imgfile] == File,
13     (* importing the selected image file *)
14
15     img = Import["image" <> ToString[picnum] <> ".TIF", {"Data"}];
16     (* testing the dimension of the selceted imagefile.
17     1. flourescence, 2. atoms, 3. without atoms, 4. background => 4*)
18
19          If[Dimensions[img][[1]] == 4,
20
21       atom = img[[2]];
22       noatom = img[[3]];
23       back = img[[4]];
24       (*
25       Setting a region of interest and testing the boundaries,
26       if they are exceeded they are set to its max/min default value
27       *)
```

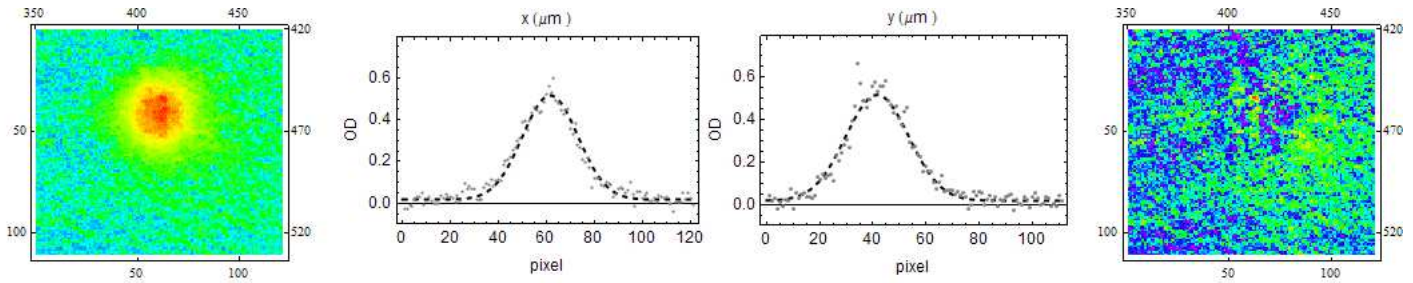

picnumber	213	TOF μs	10 100	norm	1.01323				
Max OD	0.663			@ x,y	62	34			
Max OD start fit	0.55			@ x,y	64	41			
Max OD fit	0.499			@ x,y	61.5574	41.6041			
N	92500.	N_{fit}	59700.						
Power first	0.0361	Power second	0.0235						
trap depth μK	−5.8169	ω_x	966.726	ω_y	1282.23	ω_z	1605.77	$\overline{\omega}$	1257.91
		f_x	153.859	f_y	204.074	f_z	255.567	$\overline{f}$	200.203
$1/\omega$ μs	622.753	TOF×ω	16.2						
width x 1/e μm	71.0863								
width y 1/e μm	72.6983								
T_x TOF μK	0.256479			η_x	22.7				
ϕ_x	3.14								
T_y TOF μK	0.269451			η_y	21.6				
ϕ_y	2.71								
T_{mean} TOF μK	0.265055			η	21.9				
ϕ_{mean}	2.85								
T_c μK	0.353	$\overline{T}/T_c$	0.750351	ΔT	-88.2×10^{-9}				
ROI μm×μm	476.667	x	520.						
n TOF	28.6×10^{9}	cm^{-3}	n mean in trap	276000.					
n_0	$155.\times10^{12}$	cm^{-3}							

Fri 9 Sep 2011 16:05:52

Figure B.1: Example of the display on the the front panel in Mathematica of an analysed image.

```
28      t = If[t < b && t > 0, t, 1];
29      b = If[b > t && b <= Dimensions[img][[2]], b,
30        Dimensions[img][[2]]];
31      l = If[l < r && l > 0, l, 1];
32      r = If[r > l && r <= Dimensions[img][[3]], r,
33        Dimensions[img][[3]]];
34
35      (*Extracting the region of interest*)
36
37      newatom = atom[[t ;; b, l ;; r]];
38      newnoatom = noatom[[t ;; b, l ;; r]];
39      newback = back[[t ;; b, l ;; r]];
40
41      (*width and height of the picture in pixel*)
42
43      width = r - l;
44      height = b - t;
45      xrange = width;
46      yrange = height;
47      (* estimate of the for power fluctuation*)
48
49      norm =
50       Total[(atom[[800 ;; 850, 1 ;; 50]] -
51             back[[800 ;; 850, 1 ;; 50]])/(noatom[[800 ;; 850,
52              1 ;; 50]] - back[[800 ;; 850, 1 ;; 50]]), 2]/2500 // N;
53      (* calculating the optical density*)
54      (*
55      testing the nominator and denominator for pixel values equal or \
56  smaller than zero*)
57
58      nom = (newatom - newback) /. x_ /; x <= 0 -> 0.;
59      denom = (newnoatom - newback) /. x_ /; x <= 0 -> 1.;
60      frac = nom/denom;
61      (* calculating the optical density,
```

```
62      the MedianFilter smoothes the images if wanted.
63      A greater smoothing value increases the computational time. *)
64    \
65     (*OD=-Log[frac/norm];*)
66
67      OD = Image[MedianFilter[-Log[frac/1.], 0]][[1]];
68      dims = Dimensions[OD];
69
70      (*searching for the maximum of the optical density,
71      1 automatically, 2 averaging over all lines in x and y direction*)
72
73            ODMax = Max[OD];
74      ODMin = Min[OD];
75      posmax = Position[OD, ODMax];
76      xmax = posmax[[1, 2]];
77      ymax = posmax[[1, 1]];
78
79      xmean = Mean[Table[OD[[i, All]], {i, dims[[1]]}]];
80      ymean = Mean[Table[OD[[All, i]], {i, dims[[2]]}]];
81
82      MaxX = Position[xmean, Max[xmean]][[1, 1]];
83      MaxY = Position[ymean, Max[ymean]][[1, 1]];
84
85      dims = Dimensions[OD];
86
87      xmean = Mean[Table[OD[[i, All]], {i, dims[[1]]}]];
88      ymean = Mean[Table[OD[[All, i]], {i, dims[[2]]}]];
89
90      MaxX = Position[xmean, Max[xmean]][[1, 1]];
91      MaxY = Position[ymean, Max[ymean]][[1, 1]];
92
93      NewODdata =
94       Flatten[Table[{j, i, OD[[i, j]]}, {i, dims[[1]]}, {j,
95          dims[[2]]}], {2, 1}];
```

```
96
97      Gauss2D = A*Exp[-(((x - x0))^2/wx^2 + (((y - y0))^2/wy^2))] + off;
98
99      Gauss2Dfit =
100      NonlinearModelFit[
101       NewODdata, {Gauss2D}, {A, {x0, MaxX}, {y0, MaxY}, wx, wy,
102        off}, {x, y}, MaxIterations -> 1000];
103
104     GaussPara = Gauss2Dfit["BestFitParameters"];
105
106     peak = GaussPara[[1, 2]];
107     xOFF = GaussPara[[2, 2]];
108     yOFF = GaussPara[[3, 2]];
109     xwidth = GaussPara[[4, 2]];
110     ywidth = GaussPara[[5, 2]];
111     OFF = GaussPara[[6, 2]];
112
113     FitPlotX = Plot[Gauss2Dfit[x, Round[yOFF]], {x, 0, dims[[2]]},
114       PlotRange -> {All, {1.2 Min[OD], 1.2 Max[OD]}},
115       PlotStyle -> {Dashed, Thick, Black},
116       Frame -> True,
117       FrameStyle ->
118        Directive[{{FontSize -> 12, FontFamily -> "Helvetica",
119            Thickness[0.005]}, {FontSize -> 12,
120            FontFamily -> "Helvetica", Thickness[0.005]}}],
121       FrameLabel -> {{"OD", None}, {"pixel", "x (\[Mu]m )"}},
122       Epilog -> {PointSize[0.01], Gray,
123         Point[Table[{i, OD[[Round[yOFF], i]]}, {i, dims[[2]]}]]}];
124
125     FitPlotY = Plot[Gauss2Dfit[Round[xOFF], y], {y, 0, dims[[1]]},
126       PlotRange -> {All, {1.2 Min[OD], 1.2 Max[OD]}},
127       PlotStyle -> {Dashed, Thick, Black},
128       Frame -> True,
129       FrameStyle ->
```

```
130          Directive[{{FontSize -> 12, FontFamily -> "Helvetica",
131              Thickness[0.005]}, {FontSize -> 12,
132              FontFamily -> "Helvetica", Thickness[0.005]}}],
133          FrameLabel -> {{"OD", None}, {"pixel", "y (\[Mu]m )"}},
134          Epilog -> {Gray,
135            Point[Table[{i, OD[[i, Round[xOFF]]]}, {i, dims[[1]]}]]}];
136
137
138       (* absorption picture of the reagion of interest*)
139
140       roi = MatrixPlot[OD, ColorFunction -> (Hue[1 - #] &),
141         (*AspectRatio->Dimensions[OD][[1]]/Dimensions[OD][[2]],
142         ImageSize->{{100,Dimensions[OD][[2]]},{2yrange,Dimensions[OD][[
143         1]]}},*)
144
145         FrameTicks -> {{Automatic,
146             Table[{i, i + t}, {i, 0, Dimensions[OD][[1]],
147               50}]}, {Automatic,
148             Table[{i, i + 1}, {i, 0, Dimensions[OD][[2]], 50}]}}];
149
150
151       (*Calculating the number of atoms from the absorption picture by \
152 summing up all pixels multiplied by the area of a pixel over the \
153 resonant cross section*)
154
155       atoms = Total[OD, 2]*(pixellength)^2/sigma0 // N;
156       fitatoms = Pi*peak/sigma0  xwidth ywidth *pixellength^2;
157
158       wXlength = xwidth*pixellength;
159       wYlength = ywidth*pixellength;
160       atomdensity = fitatoms/(Pi)^(3/2)/wYlength/wXlength/wYlength ;
161
162       newdens =
163        fitatoms*(Pi*w0*Sqrt[2]/lambdaL)^2/(wXlength)^3/(2 Pi)^(3/2);
```

```
164
165       (* calculating the number of atoms by integrating  a 2D Gauss \
166  with peak amplitude of the fitted optical density and width over 4 \
167  times the width of the cloud in each direction*)
168
169       thermalcloud =
170        Table[Gauss2D /. {A -> peak, x0 -> xOFF, y0 -> yOFF,
171           wx -> xwidth, wy -> ywidth, off -> OFF, x -> j, y -> i}, {i,
172          1, dims[[1]]}, {j, 1, dims[[2]]}];
173
174       residualcloud = MatrixPlot[OD - thermalcloud,
175         ColorFunction -> (Hue[1 - #] &),
176         (*AspectRatio->Dimensions[OD][[1]]/Dimensions[OD][[2]],
177         ImageSize->{{100,Dimensions[OD][[2]]},{2 yrange,Dimensions[OD][[
178         1]]}},*)
179
180         FrameTicks -> {{Automatic,
181            Table[{i, i + t}, {i, 0, Dimensions[OD][[1]],
182              50}]}, {Automatic,
183            Table[{i, i + l}, {i, 0, Dimensions[OD][[2]], 50}]}}];
184       (*N2DFit=Integrate[test[x,y]/.{A->ODFIT,x0->0,y0->0,sx->wXpixel,
185       sy->wYpixel},{x,-4* wXpixel,4*wXpixel},{y,-4*wYpixel,4*wYpixel}]*
186       pixellength^2/sigma0;*)
187
188       O1 = ODT1 /. x -> pfirst;
189       O2 = ODT2 /. x -> psecond;
190
191
192       (* caculating the trap parameters*)
193
194       U = Pi*lightspeed^2*
195         GammaD2/omegaD2^3*((2./(omegaL - omegaD2)) + (1./(omegaL -
196                omegaD1)))/2;
197       I01 = 2*O1/Pi/w1^2;
```

```
198     I02 = 2*O2/Pi/w2^2;
199
200     TrapDepth = U (2 O1 /Pi/wmain^2 + 2 O2/Pi/waux^2)/kb;
201
202     (* trapping frequencies*)
203
204     omx = Sqrt[-8*U/Pi/mRb (O2/w2^4 + O1/2/w1^2/zR1^2)];
205     omy = Sqrt[-8*U/Pi/mRb (O1/w1^4 + O2/2/w2^2/zR2^2)];
206     omz = Sqrt[-8 U/Pi/mRb (O1/w1^4 + O2/w2^4)];
207
208     meanomega = (omx*omy*omz)^(1/3);
209
210
211     Tx = mRb*omx^2*wXlength^2/kb/(1 + omx^2*time^2)/2;
212     Ty = mRb*omy^2*wYlength^2/kb/(1 + omy^2*time^2)/2;
213
214     Tc = hbar*meanomega/kb (fitatoms/Zeta[3])^(1/3);
215
216     Tmean = (Ty^2*Tx)^(1/3);
217
218     psdx = fitatoms (hbar*meanomega/kb/Tx)^3;
219     psdy = fitatoms (hbar*meanomega/kb/Ty)^3;
220
221     psdmean = fitatoms (hbar*meanomega/kb/(Ty^2*Tx)^(1/3))^3;
222
223
224     peakdens = fitatoms (mRb/2/Pi/kb/Tmean)^(3/2) meanomega^3;
225     gammael = fitatoms*8*Sqrt[2]*asRb^2*mRb*meanomega^3/Pi/kb/Tmean;
226     twobodycollision = -fitatoms*gammael*Abs[TrapDepth/Tmean]*
227       Exp[-Abs[TrapDepth/Tmean]];
228     Veff = (2 Pi kb Tmean/mRb)^(3/2)/meanomega^3;
229     threebodyloss = Gamma3BncRb Veff peakdens^3 /100^6;
230     (*summary of the data*)
231
```

```
232     data = {picco, atoms, fitatoms, norm, atomdensity, peakdens,
233       twobodycollision, threebodyloss, O1, O2, Tx, Ty, Tc, Tmean,
234       psdx, psdy, psdmean, ODMax, peak, wXlength, wYlength, MaxX,
235       MaxY, MaxX + l, MaxY + b, xOFF, yOFF, OFF, b, t, l, r, Veff,
236       TrapDepth, gammael};
237
238     numF[x_] := NumberForm[x, 3, ExponentStep -> 3];
239     (*the plots*)
240     info = Graphics[
241       Text[
242        Style[
243         Grid[
244          {{, "Image", picco, , , , , ,},
245           {, , "Max OD", "Max OD start fit", "Max OD fit", , , , ,},
246           {, "\!\(\*SubscriptBox[\"OD\", \"0\"]\)", numF[ODMax],
247            numF[OD[[MaxY, MaxX]]], numF[peak], , , , ,},
248           {, "x", xmax, MaxX, xOFF, , , , ,},
249           {, "y", ymax, MaxY, yOFF, , , , ,},
250           {, , , , , , , , ,},
251           {, , "\[Sigma] \[Mu]m", "T \[Mu]K", "\[Phi]",
252            "\[Omega] kHz", "f Hz", "\[Eta]", ,},
253           {, "x", numF[wXlength/mum], numF[Tx/muK], numF[psdx],
254            numF[omx/1000], numF[omx/2/Pi], numF[-TrapDepth/Tx]},
255           {, "y", numF[wYlength/mum], numF[Ty/muK], numF[psdy],
256            numF[omy/1000], numF[omy/2/Pi], numF[-TrapDepth/Ty]},
257           {, "z", , , , numF[omz/1000], numF[omz/2/Pi],},
258           {},
259           {, "mean", , numF[Tmean/muK], numF[psdmean],
260            numF[meanomega/1000], numF[meanomega/2/Pi],
261            numF[-TrapDepth/Tmean]},
262           {},
263           {, "P1 W", "P2 W",
264            "\!\(\*SubscriptBox[\"U\", \"0\"]\) \[Mu]K", "N",
265            "\!\(\*SubscriptBox[\"N\", \"fit\"]\)", "TOF (ms)",
```

```
266                "\!\(\*SubscriptBox[\"T\", \"c\"]\) \[Mu]K",
267                "\!\(\*OverscriptBox[\"T\", \
268 \"_\"]\)/\!\(\*SubscriptBox[\"T\", \"c\"]\)", "\[CapitalDelta]T"},
269               {, numF[O1], numF[O2], numF[TrapDepth/muK], numF[atoms],
270                numF[fitatoms], numF[time/ms], numF[Tc/muK],
271                numF[Tmean/Tc], numF[Tmean - Tc/muK], "   "},
272               {,
273                "\!\(\*SubscriptBox[\"n\", \"TOF\"]\) \
274 \!\(\*SuperscriptBox[\"cm\",
275 RowBox[{\"-\", \"3\"}]]\)",
276                "\!\(\*SubscriptBox[\"n\", \"0\"]\) \!\(\*SuperscriptBox[\
277 \"cm\",
278 RowBox[{\"-\", \"3\"}]]\)",
279                "\!\(\*SubscriptBox[\"V\", \"eff\"]\) \
280 \!\(\*SuperscriptBox[\"cm\", \"3\"]\)",
281                "\!\(\*SubscriptBox[\"\[Gamma]\", \"el\"]\) kHz",
282                "\!\(\*SubscriptBox[\"dN\", \"3\"]\)/dt kHz",
283                "\!\(\*SubscriptBox[\"dN\", \"2\"]\)/dt"},
284               {, numF[atomdensity/10^6], numF[peakdens/10^6],
285                numF[Veff*10^6], numF[gammael/1000],
286                numF[-threebodyloss/1000], numF[twobodycollision]},
287               {},
288               {, DateString[FileDate[imgfile]], SpanFromLeft,
289                SpanFromLeft, , ,}
290               }
291              , Spacings -> 2], 16
292             ]
293           ], ImageSize -> Automatic
294          ];
295       plotsnnumbers = GraphicsGrid[
296         {
297          {roi, FitPlotX, FitPlotY, residualcloud},
298          {info, SpanFromLeft, SpanFromLeft}
299          },
```

```
300         Spacings -> {0, 0}, ImageSize -> {{800, 2500}, {100, 1000}},
301         AspectRatio -> 1/GoldenRatio];
302       Export[
303        ResultDirectory <> "\\CrossedTrapRegulated" <>
304         StringReplace[imgfile, ".TIF" -> ".gif"], plotsnnumbers];
305       Export[
306        DataDirectory <> "\\CrossedTrapRegulated" <>
307         StringReplace[imgfile, ".TIF" -> ".dat"], data];
308       Export[
309        DataDirectory <> "\\CrossedTrapRegulated" <>
310         StringReplace[imgfile, ".TIF" -> ".txt"], data];
311
312       plotsnnumbers
313       ,
314       Print["pics not having the right dimensions "]
315       ],
316      Print["pics not there"]
317      ](*End If*)
318     ](*End Module*);
```

C Physical properties of Rubidium

Selected porperties of ^{87}Rb taken from [109]

Table C.1: Atomic properties of ^{87}Rb

atomic mass	m	86.909180520(15)	u
realtive natural abundance	η	27.83%	
nuclear lifetime	τ	4.8810^{10}	yr
density at 25 °C	ρ	1.53	g/cm^3
melting point	T_M	39.31	°C
boiling point	T_B	688	°C
vapor pressure at 200 °C	P_V	$3.0 * 10^{-7}$	Torr
nuclear spin	I	3/2	

Table C.2: Properties of the D2-line

frequency	ω_0	$2\pi 384.2304844685(62)$	THz
transition energy	$\hbar\omega_0$	1.589049439(58)	eV
wavelength (vacuum)	λ	780.241209686(13)	nm
wavlength (air)	λ_{air}	780.032	nm
lifetime	τ	26.24(4)	ns
natural line width (FWHM)	Γ	$2\pi 6.065(9)$	Mhz